# WATER STRUCTURES AND THE SEPARATION EFFECT ON WATER–ALCOHOL SOLUTIONS IN CARBON NANOTUBES UNDER THE INFLUENCE OF ELECTRIC FIELDS

March 2016

WINARTO

A Thesis for the Degree of Ph.D in Engineering

# WATER STRUCTURES AND THE SEPARATION EFFECT ON WATER–ALCOHOL SOLUTIONS IN CARBON NANOTUBES UNDER THE INFLUENCE OF ELECTRIC FIELDS

March 2016

Graduate School of Science and Technology
Keio University

WINARTO

*To my family*

# ACKNOWLEDGMENT

I would like to specially address this acknowledgment letter to all great people involved in this dissertation. Though my name is the only one appears on the cover of this dissertation, I owe a sincere gratitude to these people, which without their supports and guidance, I would never be able to complete my study.

Foremost, I would like to express my great appreciation to my supervisor Prof. Dr. Kenji Yasuoka for his continuous support to my study. His patience, enthusiasm, support, knowledge, and commitment to the highest level, has inspired and motivated me. I am also deeply grateful to Dr. Daisuke Takaiwa who has patiently taught me how to perform molecular dynamics simulation and to analyze data. He has always been ready for a discussion or suggesting an advice. I am also thankful to Dr. Eiji Yamamoto for his help and encouragement to support me to arrange a scientific manuscript. Not to forget, a deeply thanks for Dr. Donguk Suh and Dr. Masaki Hiratsuka who introduced and guided my first experience in leaning statistical mechanics. A great thanks also to all former and current members of Yasuoka Laboratory, Keio University for their support to my research. Their friendship is exceptionally meaningful to me to go through all the obstacles during my study and research. Hopefully, we can continue to collaborate in the scientific activities in the future. I also gratefully acknowledge the members of my thesis committee: Prof. Dr. Hiroshi Takano, Prof. Dr. Koji Fukagata, and Prof. Dr. Keita Ando, for their insightful comments, assessments, and valuable feedback. Another important person I would like to express my gratitude to, is Prof. Dr. Yasuaki Einaga, who has been a good friend to our family for all these years and who also introduced me to Prof. Dr. Kenji Yasuoka in the first place. Last but not least, I would like to thank my parents, my wife, and all of my big family members for their never ending support, continuous encouragement, and their best wishes throughout my study. This accomplishment would not have been possible without them. Again, thank you for all of you.

# ABSTRACT

Carbon nanotubes (CNTs) are promising for nanofluidic-based applications such as separation membranes and nanopumps. However, a better understanding of the properties of water molecules in CNTs is required to develop such kinds of CNT-based nanofluidic devices, since they can be very different from those in the bulk. Using molecular dynamics simulations, we investigate the effects of axial electric fields on the water molecules in CNTs. Moreover, this work investigates the effect of electric fields for separation of water–methanol solutions and water–ethanol solutions by CNTs. An alternative method for alcohol separation from aqueous solution is urgently needed for production of biofuel because the separation with distillation consumes a large amount of energy.

An electric field aligns the dipole moment of water molecules parallel to the direction of the electric field. Water molecules thus have the same orientation in the CNTs. The uniformity of the orientation then facilitates the water molecules to build hydrogen bond network for formation of ordered structures. The structures are solid-like structures or ice nanotubes structures. The electric field induces phase transition from liquid to solid in the CNTs. Although the water structures are like solid but they can flow through CNTs. Formation of the ordered structures strengthens the hydrogen bond (or electrostatic interaction) between the water molecules. This promotes the water structures in the CNTs to be more stable and water molecules prefer to fill CNTs. The preference of water to fill CNTs under the influence of an electric field is an important property to produce a separation effect.

Without an electric field, methanol molecules or ethanol molecules fill the CNTs in preference to water molecules. The preference of methanol or ethanol to occupy the CNTs over water results in a separation effect. The van der Waals interaction of CNT–methanol or CNT–ethanol is the main factor for inducing the separation effect without the electric field. However, the van der Waals interaction significantly decreases with the increase of CNT diameter. Consequently, the separation effect without an electric field is strong for small CNT diameters and significantly decreases with the increase of diameter. In contrast, under an electric field, water molecules strongly prefer to occupy

the CNTs over methanol molecules or ethanol molecules, resulting in a separation effect for water. The electrostatic interaction within the water molecules structures is the main factor for inducing the separation effect with an electric field. Thus, the formation of water structures in CNTs induced by an electric field has an important role in the separation of water from methanol or ethanol. The electrostatic interaction depends more on the molecules structures rather than the CNT diameter. As the result, the separation effect with an electric field is stronger and does not decrease with the increase of CNT diameter.

# CONTENTS

# Chapter 1

# INTRODUCTION

Since discovered in 1991 [1], carbon nanotubes (CNTs) with their extraordinary strength, unique electrical properties, and efficiency for heat conductor have attracted great attention from the scientists and engineers in numerous areas such as materials science, electronics, optics, chemical sensors, biosensors, medicine and many more fields [2,3]. More recent finding shows that CNTs have anomalous fluid property, that is the ability to transport water molecules rapidly [4]. This particular property offers a new potential application *i.e.* for nanofluidics devices.

## 1.1 Structures of Carbon Nanotubes

CNTs are tubular structures typically of nanometer diameter and many microns in length [5]. The aspect ratio (length/diameter) can be very large (greater than $10^4$), thus leads to a prototype one-dimension system. CNTs can be visualized as a rolled sheet of graphene with $sp^2$ hybridized carbon atoms. Structures of CNTs are specified by the chiral vector $C_h$,

$$C_h = n a_1 + m a_2 \equiv (n,m) \tag{1.1}$$

which is often notated by the pair of indices (*n, m*) [5-7]. The indices *n* and *m* denote the number of unit vector $a_1$ and $a_2$ (Fig. 1). A CNT is described by rolling a graphene sheet, in which the point (*n, m*) is superimposed with the origin point (0, 0). In other words, the length of the vector (*n, m*) denoted circumference of the CNT. Therefore, the diameter of a carbon tubule can be expressed as,

$$d = \frac{a\sqrt{m^2 + mn + n^2}}{\pi} \tag{1.2}$$

where $a = 1.42 \times \sqrt{3}$ Å corresponds to the lattice constant in graphene sheet [7]. Length of the C−C bond *b* is 1.42 Å for $sp^2$ hybridized carbon.

The indices (*m, n*) determine the structure of a CNT, namely armchair, zigzag, and chiral. If the index is *m = n*, the structure is armchair CNT. Zigzag CNT is for (*m*, 0) and all other indices form chiral CNTs (see Figs. 1 and 2). Theoretical studies on the

_____

electronic properties indicate that all armchair CNTs are metallic, as well as zigzag CNTs with the value of *m* multiples of three. In summary, the CNTs show metallic property when the structure can be expressed as

$$\frac{(2m+n)}{3} = integer \tag{1.3}$$
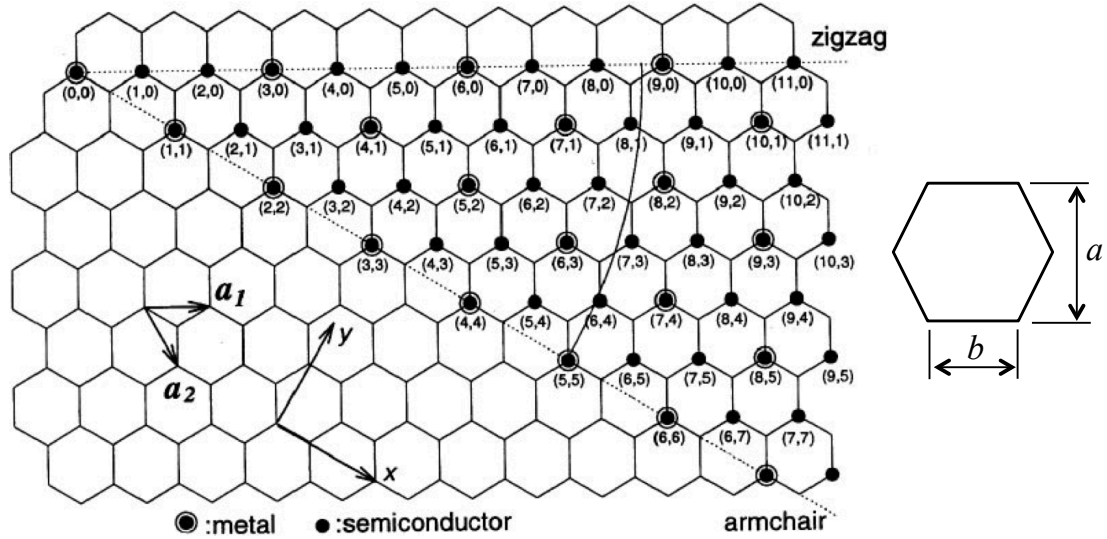


**Fig. 1** Two-dimensional structure of graphene sheet. The indices (*m, n*) indicate the number of unit vectors of $a_1$ and $a_2$. Reprinted from [6].
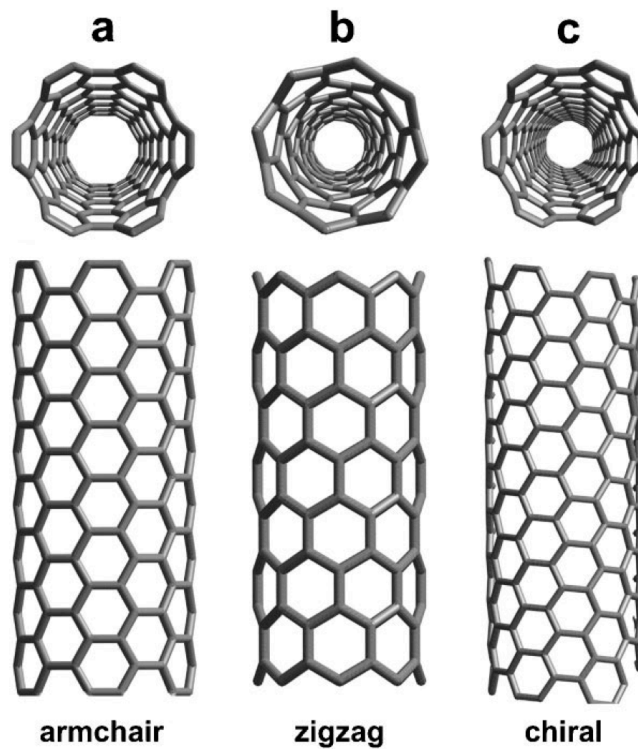


**Fig. 2** Structures of carbon nanotubes: (a) armchair, (b) zigzag, and (c) chiral. Reprinted from [7].

_____

## 1.2  Nanofluidics in Carbon Nanotubes

Nanofluidics is generally defined as the study and application of fluid flow in and around nanosize objects with at least one characteristic dimension in the range of 0-100 nm [8,9]. CNTs are hydrophobic channels with diameters in the range of nanometer and atomically smooth surfaces. It was surprising that water can enter and fill in the very narrow hydrophobic CNTs. Intuitively, one would not expect water to enter a narrow hydrophobic pore because of the tube's narrowness and water-repellent properties.

It is Hummer *et al*. who firstly reported three important results regarding water in CNTs from molecular dynamics (MD) simulations [4]. First, counter intuitively, they observed spontaneous and continuous filling of water in a (6,6) CNT (0.81 nm in diameter). The water molecules confined in such a small space form a hydrogen-bond chain (single-file configuration) that is not visible in the bulk water. Second, the simulations suggest rapid motion of water along the tube axis. Later on, other MD simulations confirm the result of fast water transport through CNTs [10-13]. Moreover, CNTs also exhibit to be very effective to deliver gas. The gas flux in CNTs reaches a three orders value of magnitude higher than in zeolites with similar pore sizes [14]. Several experimental studies provide the same evidence of fast transport of fluids through CNTs [15-18]. Permeability of gas and water through CNTs-based membranes can be higher by several orders of magnitude higher than those of commercial polycarbonate membranes, despite of having one order smaller pore size of magnitude [18]. The third interesting result is a minute reduction in the attraction between the tube wall and water dramatically affects the pore hydration, leads to sharp two-state transitions between empty and filled states on a nanosecond timescale. The result implies that transport properties of water through CNTs can be manipulated such as by small changes in the polarity, geometry of the pore, chemical modification of the tube, and so on.

Water transport in CNTs is also significant for biological science because of the similarity towards the cell channels such as aquaporins [19-21]. The major part of aquaporins is smooth hydrophobic wall that facilitates nearly frictionless transport of water, resulting in rapid transport. MD simulations show that the flow rates of water in CNTs are comparable to those through the aquaporins [10]. Actually, there is hydrophilic region in the aquaporins and so water might exhibits a more complex behavior than in a more simple CNT. However, it is believed that CNTs can be used in simulation to mimic and help understanding the behavior of aquaporins and ion channels [22].

CNTs with the smooth hydrophobic surfaces and high aspect ratio provide an ideal platform for fundamental studies of nanofluidics. Furthermore, the combination of the effective transport and feasible for manipulating the flow offers a prospective technology for the next generation of water desalination, water purification, nanofiltration, gas separation, and therapeutic applications [23-25]. Here, we briefly introduce some issues related to hydrodynamics in CNTs followed by nanofluidic-based applications of CNTs.

Continuum Navier–Stokes equations successfully describes the dynamic of fluid flow on the macroscopic scale by considering no-slip condition at a solid-liquid interface. The concept of a slip boundary condition was first proposed by Navier in 1823 as shown schematically in Fig. 3 [26]. In Navier's model, the magnitude of the slip velocity $\boldsymbol{u}_s$ is proportional to the magnitude of the shear rate experienced by the fluid at the wall,

$$\boldsymbol{u}_s = \boldsymbol{u}(R) = L_s \left\| \left( \frac{\partial \boldsymbol{u}(r)}{\partial r} \right)_{r=R} \right\| \tag{1.4}$$

where $L_s$ is slip length and $R$ denotes radius of tube. Flow enhancement $Q_E$ for Hagen-Poiseuille is described using a slip length $L_s$ as [17,27],

$$Q_E = \frac{Q_{slip}}{Q_{no-slip}} = \left( 1 + \frac{8L_s}{D} \right) \tag{1.5}$$

where $Q_{slip}$ is the observed flow rate and $Q_{no\text{-}slip}$ is the expected flow rate using the no-slip boundary condition, and $D$ is the diameter of the tube. Maxwell predicted a slip length of gas flowing past a solid surface that is in the order of the mean free path of the fluid [26]. Thus, from Eq. (1.5) for macroscopic flows the flow enhancement is so small and the no-slip boundary condition can be used without loss of accuracy. In case of nanofluidics, the slip length is comparable with the tube diameter, hence the flow enhancement is significantly important. In nanochannels both intrinsically hydrophobic surface or a hydrophobized surface the slip lengths will be in the order of or greater than the channel diameter [28].

Numerous experimental and simulation studies have been carried out to examine the slip length and flow enhancement in CNTs. However, the data for the slip length is scattered both in experiments and simulations and the precise quantification of the slip length is still a subject of great interest. Majumder *et al.* reported experimental results of slip lengths in the range of $39 - 68$ μm for a 7 nm diameter CNT, which is equivalent to flow enhancements of $(44 - 77) \times 10^3$ [15]. Holt *et al.* examined smaller nanotube

_____

membranes and found 0.14 − 1.4 μm slip length for diameters 1.3 – 2.0 nm [18]. For
more detail, the results of slip length of other experimental and simulation studies have
been summarized in Ref. 27. In summary, the slip lengths from experimental studies
vary over 5 orders of magnitude for tubes of diameters 0.81 – 10 nm and from
simulations studies between ~1 and 1100 nm for the diameter in the range 0.81 – 7 nm
[27]. The wide range of the results from one study to the others even at the same
diameter indicates that the mechanism of flow enhancement in nanotubes is still unclear.
There are more fundamental questions: Can we analytically describe water transport in
CNTs using continuum theory of fluid dynamics? Does the underlying continuum model
of fluid dynamics break down when applied on nanofluidics? Consensus on the exact
scale in which the continuum models break down has not emerged yet [23,24].
Moreover, gas dissolved in the liquid can induce nucleation of gaseous nanobubbles at
the hydrophobic surface [29]. The presence of the surface nanobubbles reduces friction
at the interface and enhances the slip length [29,30].
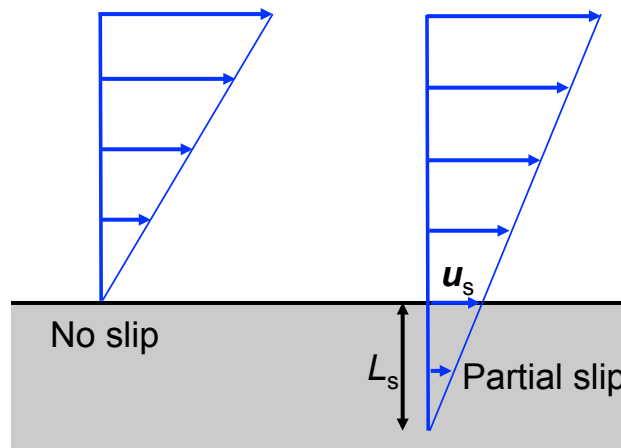


**Fig. 3**  Description of no-slip and slip condition at fluid-solid interface.

    When liquids are confined in narrow gap such as in porous medium or in between
solid walls separated by a few molecular diameters, their dynamical and structural
properties are drastically changed compared to that of the bulk. The flow of liquids under
extreme confinement cannot be understood simply by intuitive extrapolation of bulk
properties [31].  Confinement of water in nanometer gap can induce freezing at ambient
conditions [32]. Therefore, knowledge of the behavior of water confined in CNTs is
crucial for fundamentals of transport in nano channels and for development of

nanofluidic devices. Physical and dynamical properties of water in CNTs such as structure, density, hydrogen bond, dipole orientation, proton transport, diffusivity, phase transition, *etc*. become the subjects of intense research recently [33].

The extremely high flux in very small pore size potentially offers numerous advantages over traditional membrane materials for separation processes. Another important aspect is the flow can be tuned or manipulated using chemical modifications of the CNTs by attaching functional groups. Experimental study shows how the selectivity of chemical transport is influenced by chemical functionalization at the entrance of CNTs [34]. Changing some variables such as diameter of the tube, kind of functional groups, or others can optimize the separation effect.

MD simulations to demonstrate desalination with CNTs show that rejection of ions from water is very high for narrow CNTs due to larger energy barrier of the ions than that of water [35]. However, flow rates in narrow CNTs are much lower than in larger nanotubes because water transport in the narrow tubes is limited to single-file flow. Larger CNTs have much higher water flux, but the ability to reject ions decreases. Modification of CNTs by attaching charges (functional groups) at the entrance of the pore can help to prevent the passage of ions [36,37]. However, some functional groups also reduce the flow of water due to the increase of electrostatic interactions between the water molecules and the CNT. Employing charges around the tube surface can change the ions rejection property as well. The fluxes of water and ions depend on the nanotube diameter, the charge patterns, and pressure difference [38]. Obtaining high ions removal effect while allowing rapid flow of water is still a challenge for designing CNT membrane for desalination.

CNTs with sufficient pore sizes are able to separate gas mixtures such as nitrogen and oxygen [39,40], methane and hydrogen [41], as well as gases and water [42]. Other important applications are for delivery of drugs and biomolecules for therapeutics [43,44]. CNTs offer high efficiency in delivery of drugs and biomolecules especially in the specific target such as for anticancer therapy.

## 1.3 Effect of Electric Field

Study concerning the effect of an electric field on water molecules in nanotubes is very important for fundamentals of nanofluidics and for engineering applications. The combination of confinement in nano-space and strong electric field enable the water to have many interesting behaviors. Moreover, study of water molecules under the

influence of an electric field is important for biological science as well. The difference of ion concentrations between the inside and outside of biological cell membranes induces strong electric field in the cell channels [45-47]. Furthermore, the effects of an electric field on water are also significant for electrochemistry, geochemistry, *etc.* and they have been extensively studied [48-50].

Water molecules are easily influenced by an electric field due to their polarity. The electric field tends to align the orientation of the dipole moment and consequently affects the water behavior. The permeation of water through nanopores can be controlled and enhanced with the electric fields generated by ionic concentration [51]. An electric field along the axis of a narrow CNT orients the water dipoles in the tube in the direction of the field and water favors filling the CNT [52]. Electric fields can promote phase transition of water in CNTs from liquid to solid (electrofreezing) and solid to solid [53]. The electrofreezing also occurs on the water molecules confined between parallel plates [54,55].

The effects of an electric field on water confined in nano-space are also potential to design novel nanofluidic devices and molecular separation. Nano pumping of water through a CNT can be induced with time-dependent electric fields. The electric fields are generated by oscillating charges in a gigahertz frequency range that are attached laterally to the tube [56]. The pumping effect can be obtained by employing rotating electric field on water confined in a nano-channel as well [57]. The effects of an electric field is also promising to be applied for separation membranes. Water flux in a reverse osmosis of water purification can be enhanced with an electric field [58].

As a conclusion of this chapter, the field of study on nanofluidics in CNTs is still immature. The fundamental questions about physical principles that govern fast flow in the nanotubes have not been fully comprehended. Compared to the one in bulk, properties of water in the nanotubes both without and with an electric field have not been profoundly explored. Moreover, developing new devices based on CNTs nanofluidics remains a great challenge. Therefore, there will be more studies both simulation and experimental works to establish in this field.

## 1.4  Objectives of Research

This research aims to clarify effects of axial electric fields on water molecules in carbon nanotubes by performing molecular dynamics simulation. We focus on the investigation of water molecules structure and their dynamical behavior under the

influence of the electric fields. Molecular dynamics simulation is suitable tool for this study because it can reveal the structure and the dynamical behavior of molecules microscopically. Furthermore, for application, we examine the effects of the electric fields for separation of alcohol from aqueous solution. It is well known that to separate water–alcohol solution, distillation process is commonly applied. However, the distillation is very expensive due to a large amount of energy consumption.

This thesis is organized in the following order. After introduction in chapter 1, we introduce basic theory of molecular dynamics simulation in chapter 2. Then, results of the research are presented in chapter 3 to 5 as follows, Chapter 3: effects of axial electric fields on water molecules in carbon nanotubes. Chapter 4: separation of water–methanol mixtures with carbon nanotubes and electric fields. Chapter 5: separation of water–ethanol mixtures with carbon nanotubes and electric fields. Finally, the conclusions are presented in chapter 6.

# Chapter 2

# PRINCIPLES OF MOLECULAR DYNAMICS SIMULATION

Molecular simulations play an important role in science today to understand the molecules structure and the microscopic interactions between them. It allows us to reveal the properties of many-particle systems in microscopic scales. The observable thermodynamics quantity is then simply obtained by employing statistical mechanics, which is as the link between the microscopic behavior and the measurable macroscopic quantities.

There are two main categories of molecular simulations, *i.e.* molecular dynamics (MD) and Monte Carlo (MC) simulations. In the MD method, the motion of molecules (particles) is simulated according to the equation of motion and therefore it is applicable to both thermodynamic equilibrium and more advantageous for investigating the dynamical properties of a system in a non-equilibrium situation. In contrast, the MC method generates a series of microscopic states under a certain stochastic law, irrespective of the equation of motion. Basically, MC is a simulation technique for phenomena in thermodynamic equilibrium although it can be developed to study dynamical evolution of a system. However, MC and MD methods can be complementary to one another. MC is often considered as the most appropriate method to investigate systems in certain ensembles such as grand canonical or constant temperature and pressure. In this research, we investigate effects of electric fields on the structure and dynamical behavior of water molecules in carbon nanotubes, hence, MD is a suitable method for this work. In this chapter we introduce some fundamental theories of the MD simulations that are summarized from Ref. 59 to 64.

## 2.1  Molecular Dynamics

MD simulation is a technique for computing the equilibrium and transport properties of a classical many-body system [59]. In this context, classical means that the motion of the particles obeys the law of classical mechanics. The trajectory of a particle is obtained

_____

by solving the differential equation embodied in Newton's second law *(F = ma)*,

$$F_i = m_i \frac{d^2 r_i}{dt^2}$$
(2.1)

This equation describes the motion of a particle of mass $m_i$ at position vector $r_i$ with $F_i$ being the force on the particle. Therefore, in contrast to the MC method, MD is a deterministic technique, *i.e.* given an initial set of positions and velocities, the subsequent time evolution is in principle completely determined.

MD is a very powerful technique but of course it has limitations. The fundamental assumption in MD is the use of classical mechanics equation to describe the motion of atom rather than quantum mechanics. A simple test to check the validity of the classical approximation is based on the thermal de Broglie wavelength [60], defined as,

$$\Lambda = \sqrt{\frac{h^2}{2\pi m k_B T}}$$
(2.2)

where $h$ is Planck constant, $m$ is mass of the particle, $k_B$ is the Boltzmann constant, and $T$ is temperature. The classical approximation is justified if $\Lambda << a$, where $a$ is the mean distance between the particles. Almost all the system in fluid phases can be treated with the classical approximation. The typical value of $\Lambda/a$ for liquids at the triple point of light elements such as Li and Ar is of the order of 0.1 [60]. The value decreases for heavier elements. The approximation is not completely suitable for very light systems such as hydrogen ($H_2$), helium (He), and neon (Ne). Moreover, the quantum effects become important in any system with sufficiently low temperature ($T$).

## 2.2  Intermolecular Interaction

Molecular dynamics simulation consists of step-by-step numerically solution of the classical equations of motion. The forces served on the atoms are usually derived as the gradients of a potential energy. The intermolecular potential energy represents non-bonded interactions between atoms, in which it does not depend on a specific bonding between atoms. The non-bonded terms in the force field are considered in two groups, *i.e.* the van der Waals interactions and electrostatic interactions [61].

### *2.2.1 The Lennard-Jones potential*

The most widely function used to represent the van der Waals interaction of two atoms is Lennard-Jones (LJ) 12-6 function, which is expressed in the following form,

$$U_{ij}^{LJ} = 4\varepsilon \left[ \left( \frac{\sigma}{r_{ij}} \right)^{12} - \left( \frac{\sigma}{r_{ij}} \right)^{6} \right]$$

(2.3)

The LJ 12-6 potential contains two adjustable parameters, the collision diameter $\sigma$ (the separation for which the energy is zero) and the well depth $\varepsilon$. The two parameters are determined by fitting empirical properties. The LJ potential is characterized by an attractive part that varies as $r^{-6}$ and a repulsive part that varies as $r^{-12}$. The $1/r^6$ attraction part comes from the quantum mechanical calculations of the van der Waals dispersion forces, which is from dipole-dipole interaction between atoms. The term $1/r^{12}$, dominating at short distance, is to model the repulsion between atoms when they are very close to each other. Its physical origin is related to the Pauli principle, which is when the electronic clouds surrounding the atoms start to overlap, the energy of the system increases abruptly. The exponential 12 was chosen exclusively based on a practical basis, as $r^{-12}$ can be rapidly calculated by squaring the $r^{-6}$ term. The $r^{-6}$ term can also be calculated from the square of the distance without having to perform a computationally expensive square root calculation.

The LJ potential falls off very rapidly with the distance, at $r = 2.5\sigma$ the potential has around 1.7 % of the well depth [59]. The LJ potential thus represents a short-range potential. The most popular way to deal with the non-bonded interactions is to use a cut-off. When the cut-off is employed, the interactions between all pairs of atoms that are further apart than the cut-off value are set to zero. When considering periodic boundary conditions, the cut-off distance should be no greater than half the length of the shortest side. Periodic boundary condition is explained in section 2.4.

### *2.2.2 Electrostatic interaction*

Electronegative elements attract electrons more than less electronegative elements. This causes an unequal distribution of charge in a molecule. One common approach to consider the charge distribution is by arrangement of point charges throughout the molecule. These charges are designed to reproduce the electrostatic properties of the molecule. The electrostatic potential (or Coulomb potential) between two molecules is then calculated as a sum of interaction between pairs of point charges,

$$U_{ij}^{c} = \sum_{i=1}^{N_A} \sum_{j=1}^{N_B} \frac{q_i q_j}{4\pi\varepsilon_0 r_{ij}}$$

(2.4)

where $q_i$ and $q_j$ are the charges, $\varepsilon_0$ is the vacuum permittivity or electric constant, $N_A$ and

$N_B$ are the number of point charges in the two molecules.

The electrostatic interaction is a kind of long-range potential. That is because the interaction decays not faster than $r^{-d}$, where $d$ is the dimensionality of the system. The charge-charge interaction between ions decays as $r^{-1}$ and that for dipole-dipole interaction is $r^{-3}$. These potentials are a serious problem for the simulation because their range is greater than half of the box length for a typical simulation. The Ewald summation is a widely applied method to handle the problem. It can efficiently sum the interaction of a charge to all its periodic images in the periodic boundary conditions [59,61].

In the Ewald method, a particle interacts with all the other particles in the simulation box and with all of their images in an infinite array of box. The position of each image box can be related to the central box by specifying a vector $\pm iL_x, \pm jL_y, \pm kL_z$ where $i, j, k$ = 0, 1, 2, 3, … and $L_x$, $L_y$, $L_z$ are length of box. The potential energy of all pairs of charges in the central simulation box can be written,

$$U_{ij}^c = \frac{1}{2} \sum_{i=1}^{N} \sum_{j=1}^{N} \frac{q_i q_j}{4\pi\varepsilon_0 r_{ij}} \tag{2.5}$$

The charge-charge interaction between the charges in the central box and all periodic images at a cubic lattice point $n = (n_x L_x, n_y L_y, n_z L_z)$ with $n_x$, $n_y$, $n_z$ being integers,

$$U_{ij}^c = \frac{1}{2} \sum_{n}{}' \sum_{i=1}^{N} \sum_{j=1}^{N} \frac{q_i q_j}{4\pi\varepsilon_0 |r_{ij} + n|} \tag{2.6}$$

where the symbol ' is introduced to exclude the term $j = i$ if and only if $n = 0$ (at the central box). The infinite sum in Eq. (2.6) is not only converged very slowly but also conditionally converged, meaning that the result depends on the order of the summation. The Ewald method evaluates $U_{ij}^c$ by transforming it into summations that converges not only rapidly but also absolutely.

The main idea of the Ewald method is to convert the summation into two series, each of which converges much more rapidly. Every particle $i$ with charge $q_i$ is surrounded by a diffuse charge distribution of the opposite sign, such that the total charge of this cloud exactly cancels $q_i$. In that case the electrostatic potential due to particle $i$ is due to the unscreened fraction of $q_i$ exclusively. At large distances, this fraction rapidly decays to zero. The decays rapidity depends on the functional form of the screening charge distribution. Gaussian charge distribution of the following form is commonly used for

the screening charge cloud [59,61],

$$\rho_i(\boldsymbol{r}) = \frac{q_i\alpha^3}{\pi^{3/2}}\exp(-\alpha^2\boldsymbol{r}^2) \tag{2.7}$$

The contribution to the electrostatic potential at a point $\boldsymbol{r}_i$ due to a set of screened charges can be easily computed by direct summation in real space because it rapidly decays. However, we must apply the correction factor due to we have added a screening charge cloud to every particle. Therefore, we need to add compensating charge clouds as seen in the second term of the right side in Fig. 2.1. This compensating charge is summed in reciprocal space (or $k$-space) in which it converges rapidly. In summary, the electrostatic potentials calculated in the real and the reciprocal spaces are,

- Real-space term

$$U_R^c = \frac{1}{2}\frac{1}{4\pi\varepsilon_0}\sum_{i\neq j}^{N}q_iq_j\frac{erfc(\alpha r_{ij})}{r_{ij}} \tag{2.8}$$

- Reciprocal-space term

$$U_K^c = \frac{1}{2}\frac{1}{\varepsilon_0 V}\sum_{k\neq 0}\frac{1}{k^2}\exp\left(\frac{-k^2}{4\alpha^2}\right)|\rho(k)|^2 \tag{2.9}$$

$$\text{where } \rho(k) = \sum_{i=1}^{N}q_i\exp(i\boldsymbol{k}.\boldsymbol{r}_i)$$

The sum of Gaussian functions in reciprocal space includes the interaction of each Gaussian with itself. The third self-term must therefore be subtracted,

- Self term

$$U_{self}^c = \frac{\alpha}{\sqrt{\pi}}\frac{1}{4\pi\varepsilon_0}\sum_{i=1}^{N}q_i^2 \tag{2.10}$$

Hence, the Coulumb potential energy is,

$$U^c = U_R^c + U_K^c - U_{self}^c \tag{2.11}$$

The real-space term contains the complementary error function *erfc (αr)* that rapidly decays to approximately zero. This is an important point to determine the cut-off distance $r_{\text{cut-off}}$. The rate of convergence depends on the width of Gaussian distribution $\alpha$. The cut-off distance $r_{\text{cut-off}}$ will be shorter for the larger $\alpha$. On the other hand, the reciprocal-space term converges more slowly for the larger $\alpha$. The term $\alpha$ is thus an important parameter to balance the convergence of the real-space and the reciprocal-space summations. Commonly, the $\alpha$ should be chosen so that only pairwise interaction involving charges in the central box are included.

_____
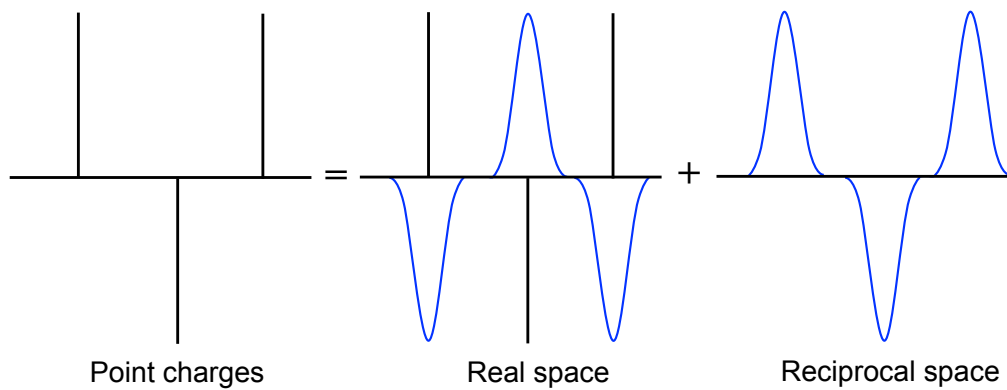


**Fig. 2.1** A schematic diagram of the Ewald summation method. The point charges are spitted into two rapidly convergent series in real space and in reciprocal space.

### 2.3  Time Integration Algorithm

The general idea to solve an ordinary differential equation such as Eq. (2.1) numerically is as follows [61,62]. Given the molecular positions, velocities, and other dynamics information at time $t$, then we attempt to obtain the positions, velocities, *etc.* at a later time $t + \Delta t$ to a sufficient degree of accuracy. The total force on each particle at a time $t$ is calculated as the vector sum of its interactions with other particles. From the force we can determine the acceleration of the particles, which are then combined with the positions and velocities at a time $t$ to calculate the positions and velocities at a time $t + \Delta t$. The force is assumed to be constant during the time step. The forces on the particles in their new positions are then determined, leading to new positions and velocities at time $t + 2\Delta t$, and so on.

All continuous quantities of classical trajectory including the positions, velocities, acceleration, *etc.* at time $t + \Delta t$ can be approximated with Taylor series expansions,

$$\boldsymbol{r}(t+\Delta t) = \boldsymbol{r}(t) + \boldsymbol{v}(t)\Delta t + \frac{1}{2}\boldsymbol{a}(t)\Delta t^2 + \frac{1}{6}\boldsymbol{b}(t)\Delta t^3 + \frac{1}{24}\boldsymbol{c}(t)\Delta t^4 + ... \tag{2.12}$$

$$\boldsymbol{v}(t+\Delta t) = \boldsymbol{v}(t) + \boldsymbol{a}(t)\Delta t + \frac{1}{2}\boldsymbol{b}(t)\Delta t^2 + \frac{1}{6}\boldsymbol{c}(t)\Delta t^3 + ... \tag{2.13}$$

$$\boldsymbol{a}(t+\Delta t) = \boldsymbol{a}(t) + \boldsymbol{b}(t)\Delta t + \frac{1}{2}\boldsymbol{c}(t)\Delta t^2 + ... \tag{2.14}$$

$$\boldsymbol{b}(t+\Delta t) = \boldsymbol{b}(t) + \boldsymbol{c}(t)\Delta t + ... \tag{2.15}$$

where $\boldsymbol{v}$ is the velocity (the first derivative of the positions with respect to time), $\boldsymbol{a}$ is the acceleration (the second derivative), $\boldsymbol{b}$ is the third derivative, and so on.

_____

### 2.3.1   The Verlet algorithm

With the Taylor series, we can write down position of a particle at time $t + \Delta t$ and $t - \Delta t$ as,

$$r(t + \Delta t) = r(t) + v(t)\Delta t + \frac{1}{2}a(t)\Delta t^2 + ...$$  (2.16)

$$r(t - \Delta t) = r(t) - v(t)\Delta t + \frac{1}{2}a(t)\Delta t^2 - ...$$  (2.17)

Adding these two equations gives,

$$r(t + \Delta t) = 2r(t) - r(t - \Delta t) + a(t)\Delta t^2$$  (2.18)

The velocities do not explicitly appear in the Verlet algorithm of Eq. (2.18). The velocities can be calculated in a varied ways, a simple approach is to divide the difference in positions at time $t + \Delta t$ and $t - \Delta t$ by $2\Delta t$,

$$v(t) = [r(t + \Delta t) - r(t - \Delta t)] / 2\Delta t$$  (2.19)

Implementation of the Verlet algorithm is straightforward and the storage requirements are modest, comprising two sets of positions *r(t)* and *r(t − Δt)* and the accelerations *a(t)*. The Verlet algorithm has some drawbacks. The positions *r(t +Δt)* are obtained by adding a small term $a(t)\Delta t^2$ to the two much larger terms *2r(t)* and *r(t − Δt)*. This may cause significant round-off error. The lack of an explicit velocity term in the equations makes it difficult to obtain the velocities, and indeed the velocities are not available until the positions have been computed at the next step. In addition, it is not a self-starting algorithm, the new positions are obtained from the current positions *r(t)* and the positions from the previous time step *r(t − Δt)*. At *t = 0*, there is obviously only one set of position and so it is necessary to employ some other means to obtain positions at *t − Δt*. One way to obtain *r(t − Δt)* is to use the Taylor series of Eq. (2.12), thus $r(-\Delta t) = r(0) - v(0)\Delta t$.

### 2.3.2   The leap-frog algorithm

The leap-frog is a variation of the Verlet algorithm, which uses the following relationships,

$$r(t + \Delta t) = r(t) + v(t + \frac{1}{2}\Delta t)\Delta t$$  (2.20)

$$v(t + \frac{1}{2}\Delta t) = v(t - \frac{1}{2}\Delta t) + a(t)\Delta t$$  (2.21)

_____

To implement the leap-frog algorithm, the velocities $v(t + \frac{1}{2}\Delta t)$ are first calculated from

the velocities at time $t - \frac{1}{2}\Delta t$ and the accelerations at time $t$. The positions $r(t + \Delta t)$ are

then determined from the velocities just calculated together with the positions at time *r(t)*

using Eq. (2.20). The velocities at time $t$ can be calculated from,

$$v(t) = \frac{1}{2}\left[ v(t + \frac{1}{2}\Delta t) + v(t - \frac{1}{2}\Delta t) \right] \tag{2.22}$$

The velocities thus "leap-frog" over the positions to give their values at $t + \frac{1}{2}\Delta t$ (as the

name). The positions then leap over the velocities to give their new values at $t + \Delta t$,

ready for the velocities at $t + \frac{3}{2}\Delta t$, and so on. The leap-frog method has two advantages

over the standard Verlet algorithm, it explicitly includes the velocity and also does not

require the calculation of the differences of large numbers. However, it has obvious

disadvantage that the positions and velocities are not synchronized. This means that it

needs additional calculation with Eq. (2.22) to determine the kinetic energy contribution

to the total energy at the same time as the positions are defined.

### 2.3.3   The velocity Verlet algorithm

The velocity Verlet algorithm uses the following equations to evolve the positions

and velocities simultaneously,

$$r(t + \Delta t) = r(t) + v(t)\Delta t + \frac{1}{2}a(t)\Delta t^2 \tag{2.23}$$

$$v(t + \Delta t) = v(t) + \frac{1}{2}\left[ a(t) + a(t + \Delta t) \right]\Delta t \tag{2.24}$$

Note that the velocity Verlet algorithm is actually implemented as a three-step

procedure,

$$r(t + \Delta t) = r(t) + v(t)\Delta t + \frac{1}{2}a(t)\Delta t^2$$

$$v(t + \frac{1}{2}\Delta t) = v(t) + \frac{1}{2}a(t)\Delta t$$

Recalculate the force at $r(t + \Delta t)$ to give $a(t + \Delta t)$

$$v(t + \Delta t) = v(t + \frac{1}{2}\Delta t) + \frac{1}{2}a(t + \Delta t)\Delta t \tag{2.25}$$

### *2.3.4   Predictor-corrector algorithm*

These methods have three basic steps. First, new positions, velocities, accelerations and higher-order terms are predicted according to the Taylor expansion Eq. (2.12) to (2.15). Second, the forces are evaluated at the predicted positions to give accelerations $a^c(t+\Delta t)$. The calculated accelerations are then compared with the accelerations that are predicted from the Taylor series expansion $a^p(t+\Delta t)$ in step 1. The difference between the calculated and the predicted accelerations is to estimate the size of the error in the prediction step,

$$\Delta a(t+\Delta t) = a^c(t+\Delta t) - a^p(t+\Delta t) \tag{2.26}$$

Third, the value of $\Delta a$ is then used to 'correct' the positions, velocities, accelerations, *etc.*,

$$r^c(t+\Delta t) = r^p(t+\Delta t) + c_0\Delta a(t+\Delta t) \tag{2.27}$$

$$v^c(t+\Delta t) = v^p(t+\Delta t) + c_1\Delta a(t+\Delta t) \tag{2.28}$$

$$a^c(t+\Delta t)/2 = a^p(t+\Delta t)/2 + c_2\Delta a(t+\Delta t) \tag{2.29}$$

$$b^c(t+\Delta t)/6 = b^p(t+\Delta t)/6 + c_3\Delta a(t+\Delta t) \tag{2.30}$$

Gear has suggested best values of the coefficients. The appropriate coefficients for the Eq. (2.27) to (2.30) are $c_0 = 1/6$, $c_1 = 5/6$, $c_2 = 1$, and $c_3 = 1/3$ [61].  The set of the coefficients depends upon the order of the Taylor series expansion.


## 2.4 Periodic Boundary Conditions

The number of particles in MD simulation is frequently less than 1000. In a system of 1000 water molecules, most of them would be within the influence of the walls of the boundary. The ratio between the number of surface molecules and the total number of molecules would be much larger than the actual one in macroscopic. Clearly, a simulation with a few thousands particles would not be an appropriate way to derive bulk properties. A solution to this problem is to use periodic boundary conditions (PBCs). When using PBCs, the particles are enclosed in a box, and we can imagine that this box is replicated in all directions to give a periodic array [61,62]. In two-dimensional each box is surrounded by eight neighbours (Fig. 2.2), in three-dimensions each box would have 26 neighbours. All these image particles move together, and in fact only one of them is represented in the computer program. When a particle leaves the box during the simulation then it is replaced by an image particle that enters from the opposite side as

_____

illustrated in Fig. 2.2. The number of particle within the central box thus remains constant.

Let us suppose that we are considering a short-range potential such as LJ potential. When separated by an equal or larger distance than a cut-off distance $r_{\text{cut-off}}$, two particles do not interact towards each other. And let us suppose that we are considering interaction of particle $i$ with $j$. Particle $j$ of course has images $j_1$, $j_2$, and so on at the image boxes. Which particle $j$ should we choose to interact with particle $i$ ? To solve this condition, there is a criterion, which is *minimum image convention.* Among the possible image of a particle $j$, select the closest and throw away all the others. In fact only the closest is a candidate to interact with particle $i$ because the distance of $i$ to all the others is larger than half of the box length. Of course, one must always make sure that the box size is at least $2r_{\text{cut-off}}$ along the all directions where the PBCs are considered.

The purpose of PBCs is to eliminate the surface effects and it is thus suitable to obtain bulk properties. However, we may also be interested in situation where we want to have surfaces. Some systems such as liquid droplet or van der Waals cluster inherently contains a boundary. Another example of simulation with surface boundary is water molecules confined between two parallel plates. This can be obtained by removing PBCs in one direction (usually taken to be $z$) while retaining them in the $x$ and $y$ directions. Therefore, the molecules is replicated to infinity in $x$ and $y$ directions, but there is no replication along the $z$ direction. The system is thus combination of PBCs and surface boundary.
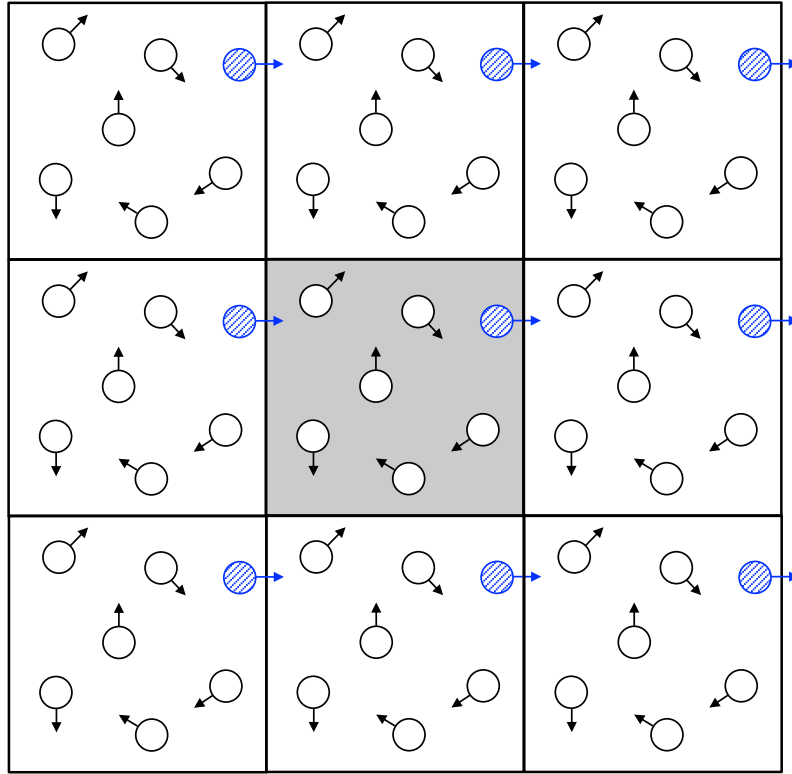
**Fig. 2.2** Periodic boundary conditions in two dimensional. When a particle moves out of from the simulation box (the central box), an image particle from opposite site moves in to replace it.


## 2.5 Temperature Control

The temperature is directly related to the kinetic energy of the system as follows,

$$E_k = \frac{k_B T}{2}(3N - N_C) \tag{2.31}$$

According to the theorem of the equipartition of energy each degree of freedom contribute $k_B T/2$. If there are $N$ particles, each with three degrees of freedom, then the kinetic energy should be $3Nk_B T/2$. $N_C$ in Eq. (2.31) is the number of constraint on the system. In MD simulations, there are some methods to control the temperature (thermostat) as follows [61,62].


• Velocity rescaling

If the temperature at time $t$ is $T(t)$ and the velocities are multiplied by a factor $\lambda$, then the change of temperature is

$$\Delta T = \frac{1}{2}\sum_{i=1}^{N}\frac{2}{3}\frac{m_i(\lambda v_i)^2}{Nk_B} - \frac{1}{2}\sum_{i=1}^{N}\frac{2}{3}\frac{m_i v_i^2}{Nk_B} \tag{2.32}$$

_____

$$\Delta T = (\lambda^2 - 1)T(t) \qquad (2.33)$$

where $\lambda = \sqrt{T_{new}/T(t)}$ .

The simple way to control the temperature is thus to multiply the velocities at each time step by the factor $\lambda = \sqrt{T_{new}/T_{curr}}$ , where $T_{curr}$ is the current temperature as calculated from the kinetic energy and $T_{new}$ is the desired temperature. The new velocity is thus,

$$v_{i,new} = v_{i,curr}\lambda \qquad (2.34)$$

- Berendsen thermostat

This method maintains the temperature by connecting the system to an external heat bath that is fixed at the desired temperature. The bath acts as a reservoir of thermal energy, supplying or removing heat from the system. The velocities are scaled at each step, such that the rate of change of temperature is proportional to the difference in temperature between the bath and the system,

$$\frac{dT(t)}{dt} = \frac{1}{\tau}(T_{bath} - T(t)) \qquad (2.35)$$

$\tau$ is a coupling parameter whose magnitude determines how tightly the bath and the system are coupled together. This method gives exponential decay of the system towards the desired temperature. The change in temperature between successive time step is,

$$\Delta T = \frac{\Delta t}{\tau}(T_{bath} - T(t)) \qquad (2.36)$$

The scaling factor for the velocities is thus,

$$\lambda^2 = 1 + \frac{\Delta t}{\tau}\left(\frac{T_{bath}}{T(t)} - 1\right) \qquad (2.37)$$

If $\tau$ is large, the coupling will be weak and when the coupling parameter equals the time step ($\tau = \Delta t$) then it is equivalent to the simple velocity scaling method. The suggested value is $\Delta t/\tau \approx 0.0025$ .

- Andersen thermostat

This thermostat implements stochastic collisions to control the temperature. This is equivalent to the system being in contact with a heat bath that randomly emits thermal particle which collides with the atoms in the system. The collision frequency of each particle is estimated as,

$$\upsilon = \upsilon_c / N^{2/3} \qquad (2.38)$$

_____

where $\upsilon_c$ is the intermolecular collision. If the collision rate is too low then the system does not sample a canonical distribution of energy. If it is too high then the temperature control dominates and the system does not show the expected fluctuation in kinetic energy.

• The Nosé-Hoover thermostat

The method is originally introduced by Nosé and subsequently developed by Hoover. This is a kind of extended system method in which the thermal reservoir is considered as an integral part of the system. The reservoir is represented by an additional degree of freedom, labeled as $s$. The reservoir has potential energy $(f+1)k_BT\ln s$, where $f$ is the number of degree of freedom in the physical system and $T$ is the desired temperature. The reservoir also has kinetic energy $(Q/2)(ds/dt)^2$. The Hamiltonian for Nosé mechanics is written as,

$$H = \sum_{i=1}^{N}\frac{p_i^2}{2m_is^2}+U(r)+\frac{p_s^2}{2Q}+(f+1)k_BT\ln s \qquad (2.39)$$

$Q$ is a parameter with the dimensions of *energy × (time)²* and can be considered as the fictitious mass of the extra degree of freedom. The magnitude of $Q$ determines the coupling between the reservoir and the real system and so influences the temperature fluctuations. If $Q$ is too large then there is no energy exchange and the temperature control is poor. However, if $Q$ is too small then the energy and temperature oscillates with high frequency, resulting problem of equilibration. $Q$ is suggested to be proportional to $fk_BT$.

## 2.6 Pressure Control

The pressure is calculated via the virial theorem. The virial is defined as the value of the sum of the products of the coordinates of particles and the forces acting on them. The virial theorem states that the virial is equal to $-3Nk_BT$. From the theorem, the pressure can be derived and expressed as follows,

$$P = \frac{1}{V}\left[Nk_BT-\frac{1}{3}\sum_{i=1}^{N}\sum_{j=i+1}^{N}r_{ij}f_{ij}\right] \qquad (2.40)$$

The first term in the right side is contribution of the ideal gas where the forces are only due to the interaction between the gas and the container. The second term comes from the interaction forces of the real gas.

_____

As shown in Eq. (2.40), the pressure can be maintained by changing the volume of the simulation cell. The volume fluctuation is related to the isothermal compressibility $\kappa$ as follows,

$$\kappa = -\frac{1}{V}\left(\frac{\partial V}{\partial P}\right)_T \tag{2.41}$$

Since compressible substance has a larger value of $\kappa$, therefore the volume fluctuation is higher compared to the more incompressible substance. The methods for controlling pressure (barostat) are analog to those used in thermostat [61,62], as follows.

- Volume rescaling

The instantaneous pressure is maintained to the target pressure by rescaling the volume of system at periodic intervals.

- Berendsen barostat

This barostat couples the system to a constant pressure bath, analogous to a temperature bath. The rate of change of pressure is given by,

$$\frac{dP(t)}{dt} = \frac{1}{\tau_p}(P_{bath} - P(t)) \tag{2.42}$$

$\tau_p$ is the coupling constant, $P_{bath}$ is the pressure of the bath, and $P(t)$ is the actual pressure at time $t$. The volume of the simulation box is scaled by a factor $\lambda$, which is equivalent to scaling the atomic coordinates by a factor $\lambda^{1/3}$,

$$\lambda = 1 - \kappa \frac{\Delta t}{\tau_p}(P_{bath} - P(t)) \tag{2.43}$$

The new position is thus given by,

$$r_{i,new} = \lambda^{1/3} r_i \tag{2.44}$$

The pressure can be fixed at constant value by applying the scaling factor to the all three directions equally (isotropically) or the scaling factor is calculated independently for each or the three axes (anisotropically).

- Andersen barostat

This is an extended ensemble barostat, in which the system is coupled to a pressure bath, *i.e.* similar to the Nosé-Hoover thermostat. The method uses a fictitious piston with a mass $Q$ to control the volume of the simulation cell. A small $Q$ makes rapid oscillation of the simulation box, whereas a large $Q$ has the opposite effect.

- Parrinello-Rahman barostat

The Andersen barostat changes the volume of the simulation box isotropically. Parrinello-Rahman method allows the simulation box to change shape as well as size. This technique is particularly useful for simulation of solids, since it allows for phase changes in the simulation that may involve changes in the unit cell dimension and angle.

## 2.7 Constraint Dynamics

It is common in MD simulations not to include potential energy of molecular bonds, because these bonds have very high vibration frequencies. The vibration of the molecular bonds should be treated in a quantum mechanical way rather than in the classical approximation. In MD simulation, the bonds can be treated to have fixed length by imposing constraint in the equation of motion [62,63]. For example a molecule has two atoms (1 and 2) with fixed bond length $b$, one may write a constraint equation as,

$$\chi(r_1, r_2) = (r_1 - r_2)^2 - b^2 = 0 \tag{2.45}$$

By considering the constraint, the equation of motion can be expressed as,

$$m_i \ddot{r}_i = F_i + \lambda g_i \tag{2.46}$$

where $\lambda$ is the Lagrange multiplier and

$$g_1 = -\frac{\partial \chi}{\partial r_1} = -2(r_1 - r_2) \tag{2.47}$$

$$g_2 = -\frac{\partial \chi}{\partial r_2} = 2(r_1 - r_2) \tag{2.48}$$

In general, if there are $N_c$ equations of constraint, the equation of motion can be written as,

$$m_i \ddot{r}_i = F_i + \sum_{k=1}^{N_c} \lambda_k \nabla_i \chi_k \tag{2.49}$$

Although it is possible to obtain an exact solution for the Lagrange multipliers, but that is not what we want. In practice, the equations of motion are solved numerically in discrete time steps. The numerical integration of the equations of motion obtained by substituting the exact solution of the Lagrange multipliers $\lambda$ would not exactly preserve the constraint condition due to numerical errors. Moreover, it may lead to unwanted instabilities. These problems can be solved using SHAKE and RATTLE schemes for computing the multipliers so that the constraints are satisfied exactly at the end of each time step. SHAKE is developed based on the Verlet algorithm and RATTLE is based on the

_____

velocity Verlet algorithm.

# Chapter 3

# WATER IN CARBON NANOTUBES UNDER THE INFLUENCE OF ELECTRIC FIELDS

## 3.1  Introduction

One of the outstanding properties of carbon nanotubes (CNTs) is the rapid transport of water molecules [4,15-18]. Thus, CNTs could be used for membrane desalination [10,36,38,58], nano-pumping [56,65-69], and therapeutic and diagnostic medicine [44,70-72]. Therefore, it is very important to understand the properties of water in the CNTs. Water molecules confined in nanoscale tubes can form a variety of structures that can significantly differ from those in the bulk. Under high axial pressures of $50 - 500$ MPa, ice nanotubes were formed in CNTs with 1.1- to 1.4-nm diameters. The results were heptagonal, hexagonal, pentagonal, and square ice structures which were not observed in bulk ice [73]. At higher axial pressures of 500 MPa to 4 GPa in 1.35- to 1.90-nm diameter CNTs, multi-walled ice nanotubes with helical and $n$-gonal structures were observed [74]. At atmospheric pressure (0.1 MPa) and 300 K, helical structures of water molecules in (7,7), (8,8), (9,9), and (10,10) CNTs were obtained [75], as well as for (10,10) CNTs at 298 K [76]. According to the phase diagram of water in CNTs at 0.1 MPa, the water structures below the freezing temperature were either helical or $n$-gonal ice nanotubes, depending on the CNT diameter [77]. Ice nanotubes have been characterized experimentally [78-82].

When a membrane separates different ion concentrations, water molecules in the membrane can be affected by strong electric fields [46,47,58]. Strong electric fields affect water molecules in CNTs in different manners. They change the orientation of the water molecules in the CNT such that their dipole vectors parallel to the electric field [52,53,83-87]. The new orientation causes anomalous behavior of the water molecules. Free energy analysis has shown that the orientation induced by the electric field in (6,6) CNTs shifted the equilibrium state towards the condition where water preferentially fill the CNT [52]. The dipole vector orientation of single lines of water molecules in a CNT can be tuned with the electric field, which results in a pumping effect [83,84]. However,

other studies disproved that the pumping is caused by force discontinuity due to cut off of Lennard-Jones interaction [88,89]. The dipole orientation due to the electric field, together with the confinement of the CNT wall, created new water structures which is not observed in the absence of the electric field [53,85-87]. Electric-field-induced phase transitions of water molecules in the finite length, 1.20- to 1.31-nm diameter CNTs immersed in bulk water at atmospheric pressure exhibited structures that were a function of the electric field strength [53,86]. At 0 V/nm, the structures were initially *n*-gonal, and then changed to helical as the electric field increased. This electric-field-induced phase transition was also observed for water in infinite-length CNTs with 1.11- to 1.25-nm diameters [87].

Here, we perform molecular dynamics (MD) simulations to investigate the effect of an axial electric field on the structure of water in the finite-length CNTs with 0.95- to 1.36-nm diameters. The electric fields are 0, 1, and 2 V/nm under ambient conditions (300 K). In contrast to previous studies [53,86], we mimic a membrane in our simulation with CNTs and graphene sheets with reservoirs on both sides. We demonstrate that the electric field changes the orientation of the water molecules and causes formation of solid ice-like structures in all of the CNTs. Moreover, we analyze the effect of electric fields on the dynamical behavior of the water molecules in the CNTs and compare it to the dynamics in the reservoir and in bulk water.

## 3.2  Simulation Method

In the simulation, the CNT length was 2.95 nm, while the diameters were 0.95 nm, 1.08 nm, 1.22 nm, and 1.36 nm for (7,7), (8,8), (9,9), and (10,10) CNTs, respectively (see Fig. 3.1(a,b)). The graphene sheets were $3.7 \times 3.7$ nm. The initial number of water molecules in each reservoir was 4000. Periodic boundary conditions were considered in all axial directions. The water model was SPC [90]. The Lennard-Jones (LJ) parameters for the water oxygen atom were $\sigma_O = 0.3166$ nm and $\varepsilon_O = 0.65$ kJ/mol, and for the CNT carbon they were $\sigma_C = 0.34$ nm and $\varepsilon_C = 0.3612$ kJ/mol. The LJ parameters to determine the interaction between different atoms were calculated with the combination rules $\sigma_{OC} = (\sigma_O \times \sigma_C)^{1/2}$ and $\varepsilon_{OC} = (\varepsilon_O \times \varepsilon_C)^{1/2}$. As shown in Fig. 3.1, the system includes water molecules, a CNT, and two graphene sheets in a rectangular cell with dimensions $L_x L_y L_z$ in the *x*, *y*, and *z* directions. Hereafter, we refer to the direction along the CNT as the *z*-axis. A homogeneous electric field was introduced along the positive *z*-axis. The MD

simulation was performed with Gromacs 4.5.5 software [91].

The van der Waals interactions were cut off at 1.5 nm, while electrostatics were treated with a particle mesh Ewald method [92] with a real-space cut-off of 1.5 nm. The SHAKE algorithm [93] was employed to fix the chemical bonds between the atoms of the water molecules. CNT and graphene sheet atoms were frozen to avoid deformations. The time step was 2 fs, and the temperature ($T$) was maintained at 300 K with the Nosé-Hoover coupling scheme [94,95]. Constant pressure in the $z$ direction was maintained at 0.1 MPa with the Parrinello-Rahman technique for pressure coupling [96]. We performed $NL_xL_yP_zT$ simulations for 25 ns. We observed time evolution of occupancy of molecules in the CNTs to determine an equilibrium condition. In general, the systems reached an equilibrium state less than 3 ns and we analyzed data of the last 22 ns.

We also performed MD simulations for 2000 bulk water molecules in a simulation box. The water model, temperature, pressure, electric fields, and other simulation conditions were the same as above. The simulation time was 5 ns and the analyzed data was taken from the last 3 ns.
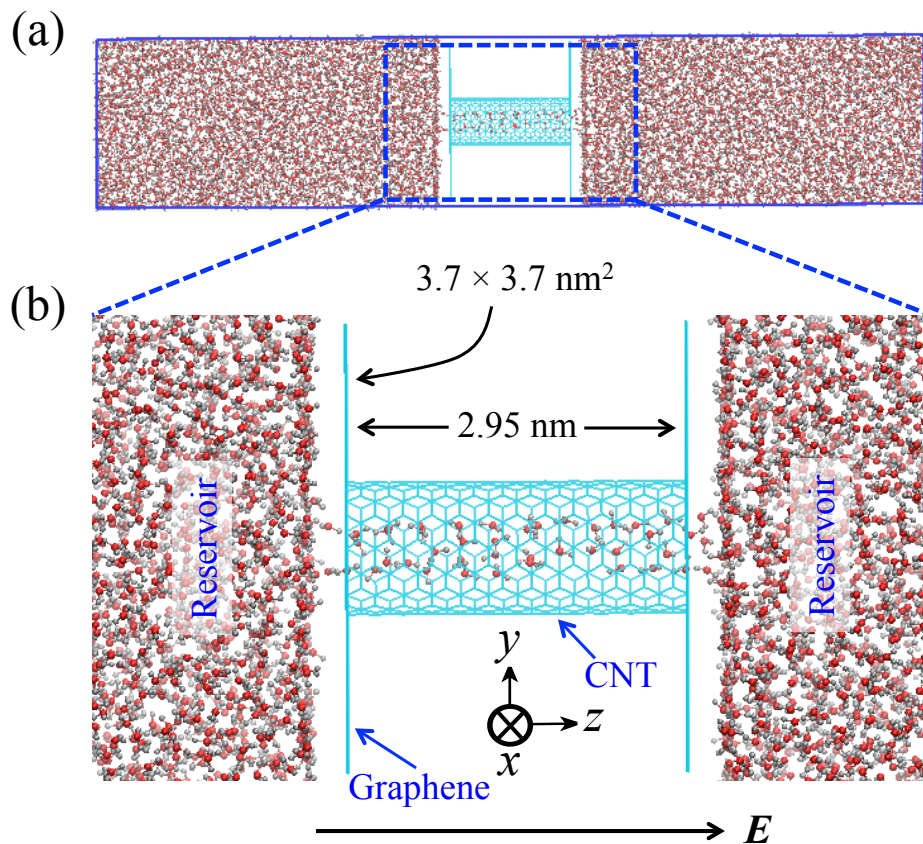


**Fig. 3.1** (a) The MD simulation consists of two graphene sheets, a CNT, and water molecules. (b) Magnified view. A homogeneous electric field ($E$) is applied along the $z$-axis.

_____

## 3.3  Results and Discussion

### *3.3.1  Orientation of water molecules*

To verify the density profile of water near the graphene sheets, we calculated the density of oxygen atoms in the axial direction (Fig. 3.2). As previously reported, the typical water density near hydrophobic surfaces can be divided into three regions: the first layer from the wall to the first minimum, the second layer between the first and the second minimum, and a bulk-like layer [97,98]. Here, the water molecules were divided as follows: (a) NL and NR are the first layer regions < 0.5 nm (the first minimum) from the left and right sides of the graphene walls, respectively; (b) R is the reservoir region after the third minimum (> 1.24 nm from the walls).

The direct effect of the electric fields on the water molecules is the change of molecular orientation. Figure 3.3 shows the probability density functions (PDFs) of orientation (cos $\alpha$) of water molecules in each region, where $\alpha$ is the angle between the water dipole vector $\boldsymbol{\mu}$ and the electric field $\boldsymbol{E}$ (or positive $z$-axis). In the absence of the electric field (green data), the orientation of the water molecules in the bulk and in the reservoir is exactly the same in all directions (Fig. 3.3(a)). Under the electric field, the angle $\alpha$ tends to be zero as indicated by the peaks at cos $\alpha = 1$. However, the peak for the reservoir is significantly lower than that for the bulk, which implies that water molecules in the reservoir are affected by the graphene walls. The dipole vector is not statically parallel along the electric field, it oscillates instead. The amplitude of the oscillation decreases as the strength of electric field increases, which indicated by the relatively higher and narrower peak for 2 V/nm compared to that for 1 V/nm. The presence of the graphene wall affects the rotational dynamics of the water in the reservoir and promotes a significantly larger amplitude compared to the one in the bulk.

At 0 V/nm, water molecules near the graphene walls tend to have two orientations. In the NL region, cos $\alpha$ has two peaks at −0.5 and 0, and in the NR region, those are at 0.5 and 0 (Fig. 3.3(b)). Thus, the dipole vectors form 60° and 90° angles with respect to the outward-pointing normal vector of the graphene walls. These are the usual orientations of water molecules in the first layer near a hydrophobic surface [97-99]. In the 60° molecules, one OH bond forms a 0° angle with the outward-pointing normal vector, while the other (dangling) OH bond is oriented towards the graphene wall. In the 90° molecules, the OH bonds are parallel to the graphene surface. With an electric field, cos $\alpha$ in the NL region has one peak at 0.5 and 0.7 for 1 V/nm and 2 V/nm, respectively.

Those values in the NR region are 0.5 and 0.6, respectively. Therefore, under the electric fields, the dipole vectors in the NL region tend to point towards the graphene wall, while they point away from the graphene wall in the NR region. Hence, the electric field induces different water structures in the NL and NR regions. The density of oxygen atoms at 2 V/nm in the NR region is higher than that in the NL region, which indicates a structural difference (Fig. 3.2). Moreover, the field induces polarization, which is positive and negative near the left and the right graphene walls, respectively (see subsection 3.3.2). The polarization generates internal electric field in the reservoir in the opposite direction to the external electric field. Thus, the effective electric field in the reservoir is lower than the field in the bulk. This promotes the different dynamical behavior of water molecules in the reservoir compared to the one in the bulk.

Figure 3.4 shows the orientation of water molecules inside the CNTs. At 0 V/nm, there are two peaks at −0.8 and 0.8 symmetric about $\cos \alpha = 0$. It confirms the previous work where water molecules in CNTs have two orientations, opposite to each other [100]. With the increase of electric fields, the direction of the dipole vector is more concentrated at $\alpha = 0$. Thus, the electric field reorients the dipole vector to be parallel to that of the field, is in agreement with previous studies [52,53,83-87].
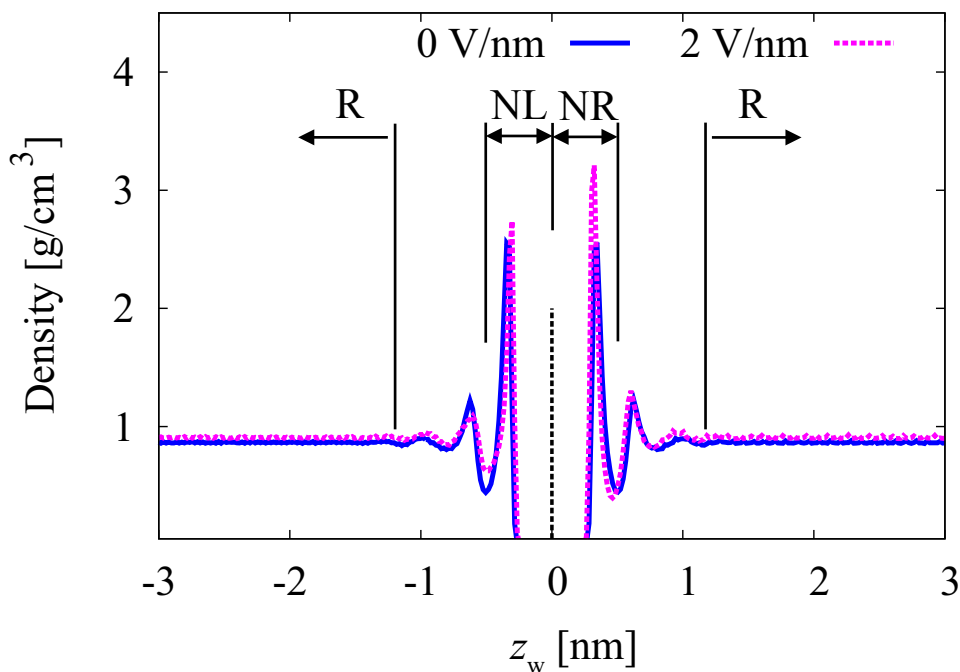


**Fig. 3.2** Density distribution of oxygen atoms along the axial direction under 0 V/nm and 2 V/nm. $z_\mathrm{w}$ is the distance away from the graphene walls, where the negative and positive values indicate the position from the left and right walls respectively. NL and NR denote the first layer regions near the graphene walls at left side and right side, respectively. R is the reservoir region.
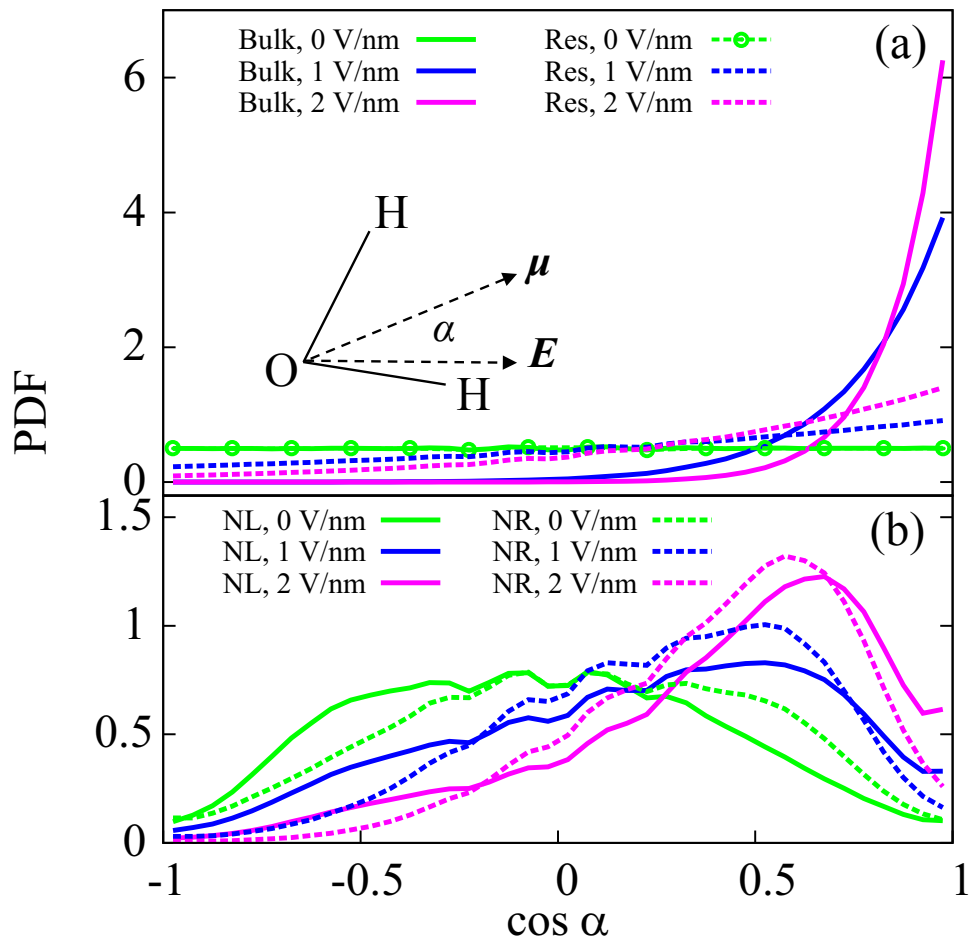
**Fig. 3.3** Orientation of water molecules. (a) PDFs of cos $\alpha$ in the bulk (solid lines) and the reservoir (dashed lines), and (b) in the NL (solid lines) and NR regions (dashed lines). The colored lines indicate values of the electric field. The value $\alpha$ is the angle between the dipole vector $\boldsymbol{\mu}$ and the electric field $\boldsymbol{E}$.
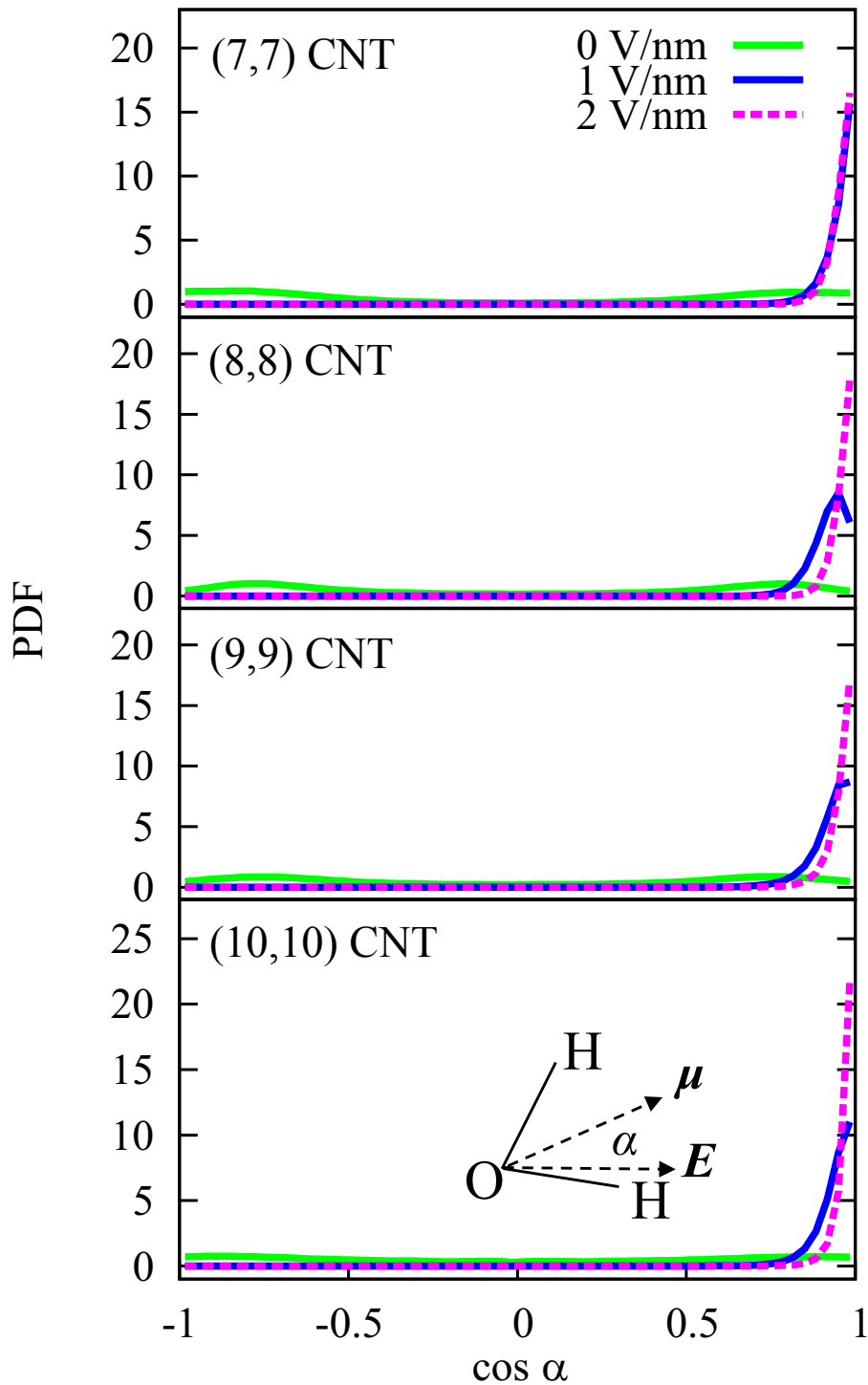
**Fig. 3.4** Effect of electric fields on the orientation of water molecules in CNTs, where $\alpha$ is the angle between the water dipole vector $\boldsymbol{\mu}$ and the electric field $\boldsymbol{E}$. The electric field forces the dipole vector to be parallel to it.

_____

### *3.3.2  Polarization*

To examine the polarization, we calculated distribution of charge density and internal electric field. The simulation box was divided into thin slices of 0.02 nm thickness along the *z*-axis and the charge density of each slice was then computed. Figure 3.5 shows the distribution of charge density in the reservoir between the right and left graphene walls (R-wall and L-wall) with 0 and 2 V/nm of external electric field. Axial position of the R-wall and the L-wall are $z = 0$ and $z = l$, respectively. The charge density near the walls fluctuates and then becomes constant at zero in the region $> 1.24$ nm from the walls. On the other hand, the charge density distribution for bulk water remains constant at zero.

Then, the axial distribution of the internal electric field was calculated with equation,

$$\frac{dE_z}{dz} = \frac{\rho_z}{\varepsilon_0} \tag{3.1}$$

where $E_z$ is the axial distribution of the internal electric field, $\rho_z$ is the distribution of charge density (Fig. 3.5), and $\varepsilon_0$ is the vacuum permittivity. The internal electric field was obtained by integrating Eq. (3.1) with boundary condition $E_z = 0$ at $z = 0$, numerically. With 0 V/nm, the internal electric field near the walls fluctuates and then becomes constant at 0 V/nm (Fig. 3.6). This indicates the internal electric field in the reservoir 0 V/nm and the polarization does not occur near the walls. With 2 V/nm, the internal electric field decreases to a constant value around $-10$ V/nm and then increases near the L-wall to a constant 0 V/nm. This implies that the polarization of water molecules occurs near the walls, which is negative and positive near the right and left graphene walls, respectively (Fig. 3.6). At 1 V/nm, the internal electric field is $-5$ V/nm. Variation of the slice thickness from 0.01 nm to 0.1 nm does not change the results. The results are also consistent for 5 ns, 10 ns, and 22 ns of simulation data indicating the number of sample is sufficient to observe the polarization. Direction of the internal electric field is from L-wall to R-wall, which is opposite to the external field. Thus, the internal electric field weakens the external electric field in the reservoir. Strength of the internal electric field must be lower than the external electric fields. However, the result in Fig. 3.6 shows that the internal electric field is larger than the external field. This suggests that the vacuum permittivity $\varepsilon_0$ should be multiplied by a dielectric constant. The dielectric constant of bulk SPC water is about 65. In case of bulk water, the internal electric field is constant zero. Actually, the polarization is only an artifact. In the real reservoir, behavior of water should be same as the bulk.
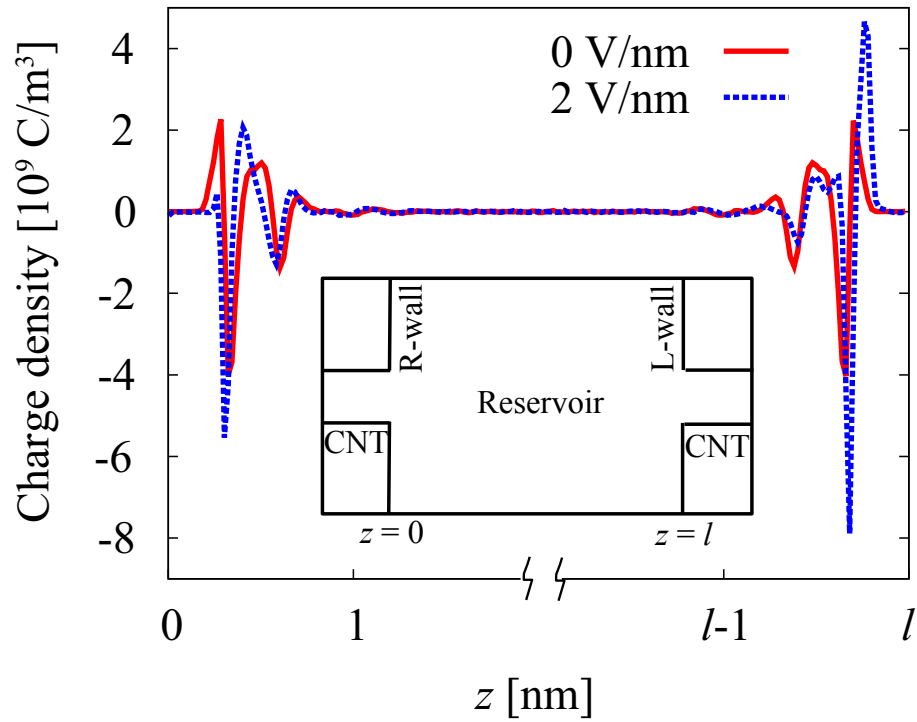
**Fig. 3.5** Distribution of charge density in the reservoir between the right and left graphene wall (R-wall and L-wall) with 0 V/nm and 2 V/nm. The axial position of R-wall and L-wall are $z = 0$ and $z = l$, respectively.
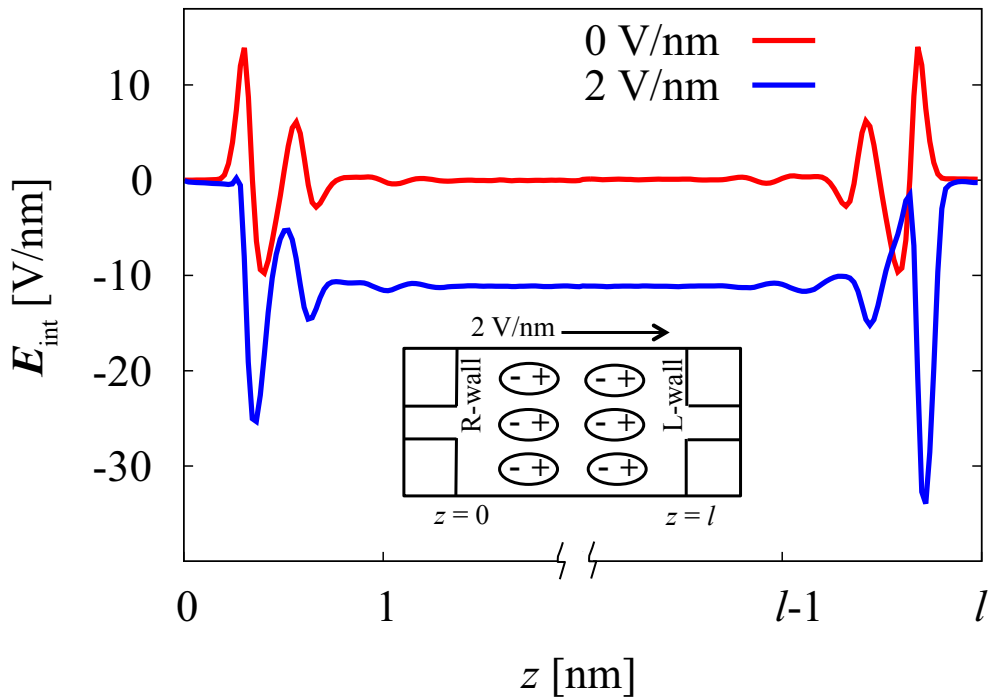


**Fig. 3.6** Distribution of internal electric field ($E_{int}$) in the reservoir between the R-wall and the L-wall with 0 V/nm and 2 V/nm of external electric fields. When 2 V/nm is applied to the direction from R-wall to L-wall, polarization occurs which is negative near the R-wall and positive near the L-wall.

### *3.3.3 Radial density distribution of water molecules in CNTs*

To provide a distribution profile of water in the CNTs, the density of oxygen atoms in the radial direction was calculated (Fig. 3.7). In the presence of the electric field, the peaks are higher, narrower, and located far from the center of the CNTs. Thus, the water molecules form a tube-like structure. The structure is ice nanotube structure as reported in previous studies [53,73,74,77,101]. Using X-ray diffraction [78,79], proton nuclear magnetic resonance [80], neutron scattering [81], and vibrational spectroscopy [82], the tube-like structure of the ice nanotubes were observed experimentally. When the magnitude of the electric field increases, the radius of the tube-like structure increases as well, and the structure accommodates more water molecules. This is consistent with occupancy data presented in subsection 3.3.5 that the electric field increases the number of water molecules in the CNTs. If the diameter of the CNT is sufficiently large, such as in case of (9,9) and (10,10) CNTs, the water molecules form two structures in the inner and outer regions, as shown by two peaks in the density profile.
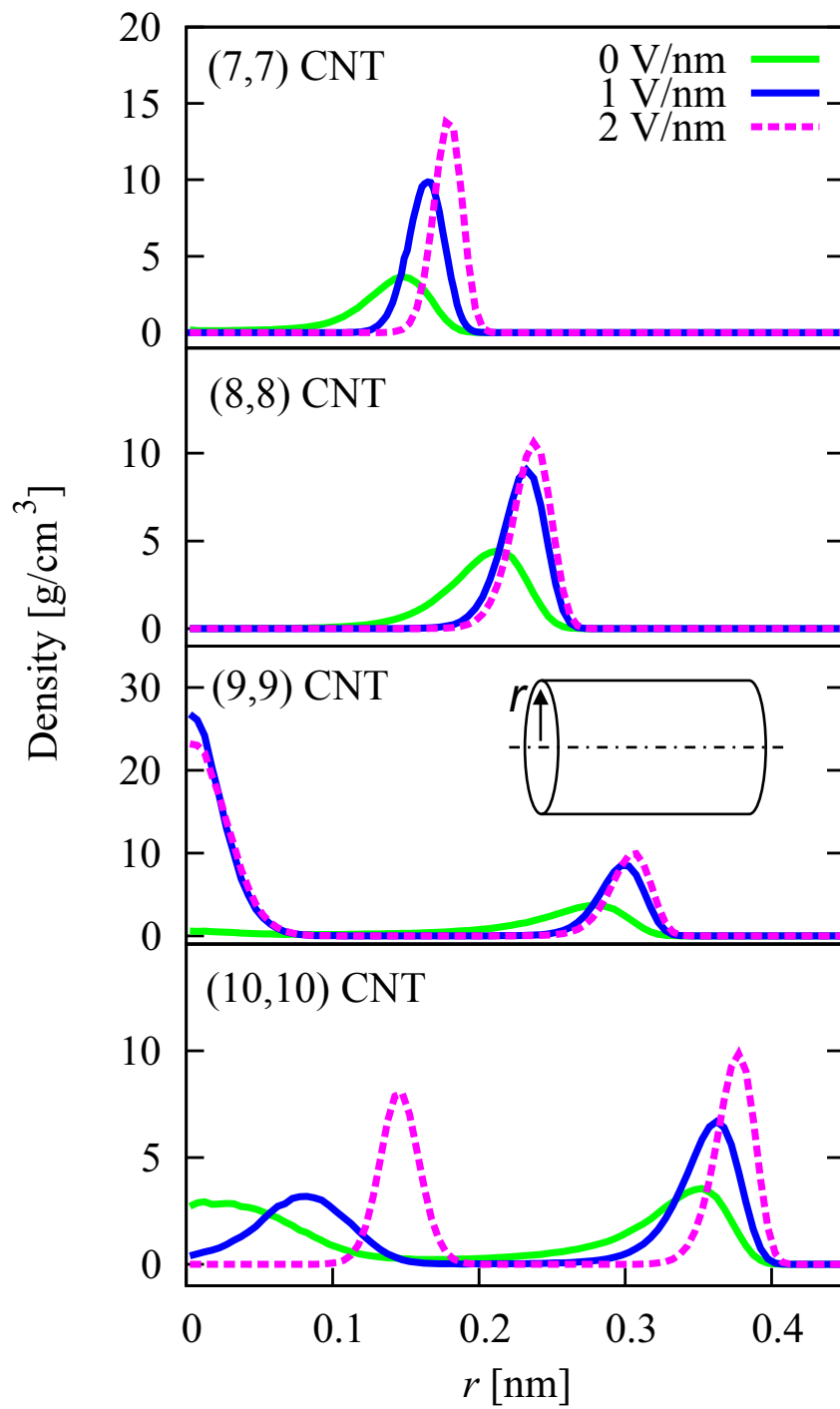
**Fig. 3.7** Radial density distribution of oxygen atoms inside CNTs under electric fields, where $r = 0$ is at the center axis of the CNTs.

_____

### *3.3.4 Structure of water molecules in CNTs*

Water structures in CNTs under electric fields are shown in Fig. 3.8(a). It is clear that there is a transition from disordered to ordered structures when the electric field is introduced. For example, the structure in the (7,7) CNT at 0 V/nm is disordered and formation of a helical structure occurs at 1 V/nm and 2 V/nm. The helical structures are also observed in the (8,8) CNT under 1 V/nm and 2 V/nm, the outer structure in the (9,9) CNT under 1 V/nm and 2 V/nm, and the outer structure in the (10,10) CNT under 1 V/nm. The (9,9) CNT under 1 V/nm and 2 V/nm and the (10,10) CNT under 1 V/nm have single line structures in the center. The (10,10) CNT under 2 V/nm has other ordered structures for the inner and outer that are not helical. These results indicate that the electric field induces formation of ice nanotubes as reported in previous studies without [73,74,77,101] and with electric fields [53,86,87].

To characterize the structure in more detail, we can "unroll" the tube-like structure into two-dimensions. Figure 3.8(b) shows the two-dimensional square net water structure in the (7,7) CNT, marked by two index numbers ($n$, $m$) [77,101]. When the sheet is rolled up to form a tube, two black circles in Fig. 3.8(b) are connected as indicated with the magenta arrow. From each point, a line can be drawn along the rows (black dotted line) and the columns (blue dotted line) formed by the arrangement of water molecules. The rows and columns directions are determined by the angle formed with the tube axis, where the columns have a smaller angle. The structure index is obtained from the black and blue arrows. In the case of the (7,7) CNT under 2 V/nm, the length of the black arrow is four unit columns and the length of blue arrow is two unit rows. Thus, the structure is a (4,2) ice nanotube. Similarly, the structure index of the (7,7) CNT under 1 V/nm is a (3,2) ice nanotube. Table 3.1 is a summary of structure indices for all the cases. If $n \neq m$, the structure is helical, and if $m = 0$ the structure is $n$-gonal [73,77,101]. For the (10,10) CNT under 2 V/nm, the other ordered structure is $n = m$ for both inner and outer, which has not been reported previously [53,73,77,86,87,101]. The index for the inner ice nanotube structure is (2,2) and is (6,6) for the outer ice nanotube structure. The inner structures inside the (9,9) CNT under 1 V/nm and 2 V/nm, and the (10,10) CNT under 1 V/nm, are single lines (1L).
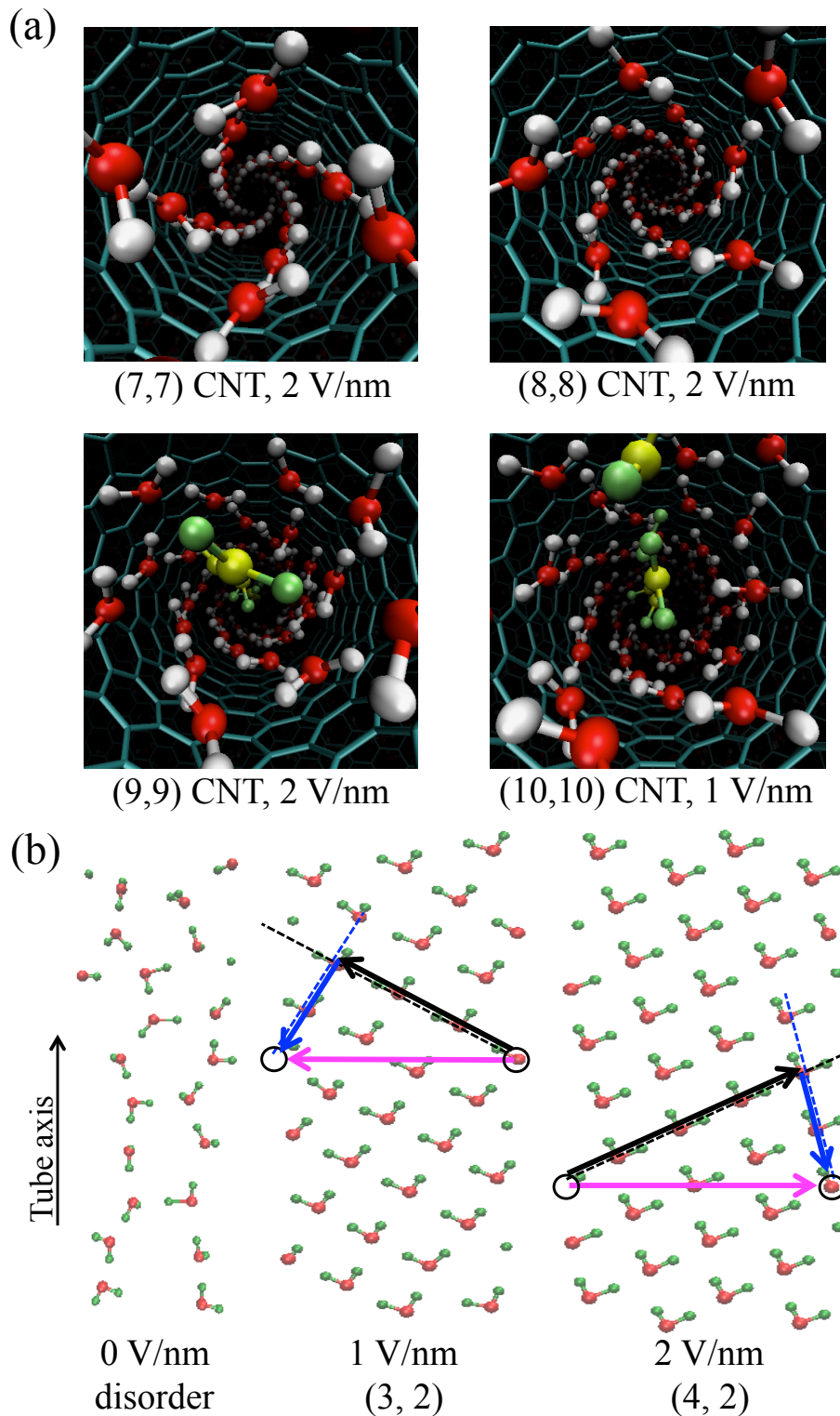
**Fig. 3.8** Tube-like structures of water molecules in CNTs. (a) Structures of water molecules in the (7,7) CNT under 2 V/nm, the (8,8) CNT under 2 V/nm, the (9,9) CNT under 2 V/nm, and the (10,10) CNT under 1 V/nm. The oxygen and hydrogen atoms are colored red and white, respectively. In the case where there are inner and outer structures, the water molecules in the inner structure are drawn with yellow for oxygen and green for hydrogen. (b) Two-dimensional structures of water molecules in the (7,7) CNT. Disordered, (3,2) ice nanotube, and (4,2) ice nanotube structures are observed for 0 V/nm, 1 V/nm, and 2 V/nm of electric fields, respectively. The red and green atoms indicate oxygen and hydrogen atoms, respectively.

_____

**Table 3.1** Structure indices of water molecules in CNTs. For the (9,9) CNT and the (10,10) CNT under 1 V/nm and 2 V/nm there are inner (in) and outer (out) structures.

| *E* [V/nm] | (7,7) CNT | (8,8) CNT | (9,9) CNT | (10,10) CNT |
|:---:|:---:|:---:|:---:|:---:|
| 0 | disorder | (4, 0), disorder | (6, 0), disorder | disorder |
| 1 | (3, 2) | (5, 2) | out: (6, 3) in: 1L | out: (7, 4) in: 1L |
| 2 | (4, 2) | (5, 3) | out: (6, 4) in: 1L | out: (6, 6) in: (2, 2) |

The water structures in the (8,8) CNT under 0 V/nm are (4,0) ice nanotubes and disordered, *i.e.*, not stable. The ordered (4,0) structure can be easily converted to a disordered one, as shown in Fig. 3.9(a). The (6,0) ice nanotube in the (9,9) CNT under 0 V/nm is easily broken as well (see Fig. 3.9(b)). The unstable structures most likely occur in the (8,8) and (9,9) CNTs because the temperature is close to the freezing point.

For the (8,8) CNT, the electric-field induced change of water structure from (4,0) to (5,2), (5,3), and for the (9,9) CNT, the induced change from (6,0) to (6,3), (6,4), is from *n*-gonal to helical. This was previously observed for the finite length CNTs with 1.20-nm and 1.31-nm diameters [53,86] and in infinite-length CNTs with 1.11-nm and 1.25-nm diameters [87]. However, for the (9,9) CNT under 0 V/nm and 2 V/nm, Fu *et al.* [53] reported (5,0) and (5,1) ice nanotubes instead of (6,0) and (6,4) + 1L ice nanotubes. This may be because of a simulation system where they immersed CNT in bulk water molecules, which allows the water in the CNT to be affected by water outside the CNT. They also applied a different water model (TIP4P).

The change from a disordered structure under 0 V/nm to an ordered ice nanotube under 1 V/nm and 2 V/nm in all CNTs (Table 3.1) indicates an increase of the freezing point. Previous studies also reported an increase of freezing point as the electric field increases [53,86,87]. Qian *et al.* immersed a 1.31-nm diameter CNT [86], which is between the diameters of the (9,9) and (10,10) CNTs, in TIP4P water and found that under 1 V/nm and 2 V/nm, the freezing points are 230 K and 245 K, respectively. Those freezing temperatures are significantly lower than in this study, which should be $\geq$ 300 K at 1 V/nm and 2 V/nm. The simulation system and/or the water model may cause the difference of the freezing point.
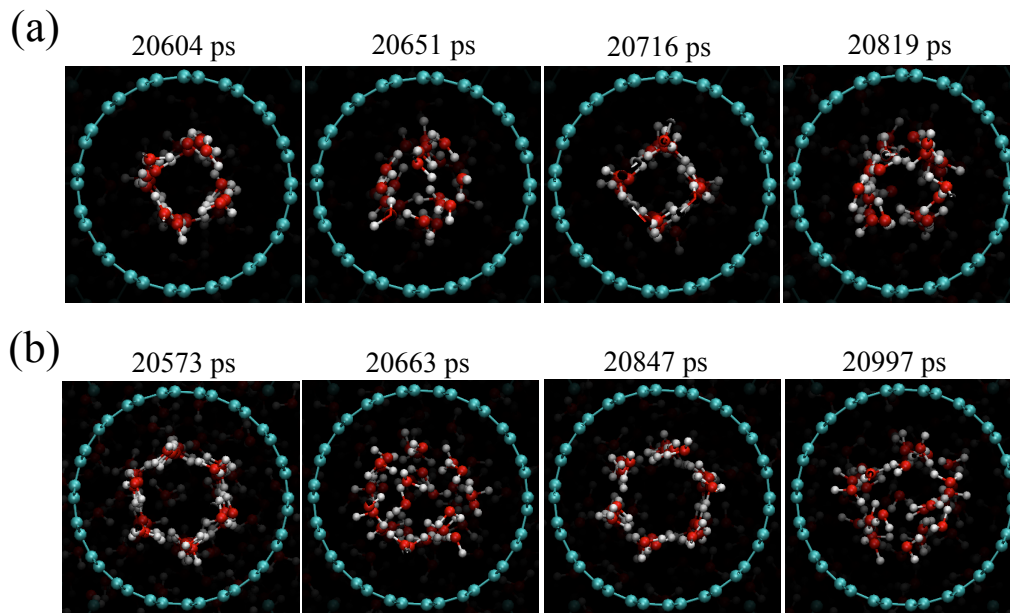
**Fig. 3.9** Unstable water molecule structures. (a) In the (8,8) CNT under 0 V/nm of electric field, the (4,0) ice structure can be converted to a disordered structure. (b) In the (9,9) CNT under 0 V/nm, the (6,0) ice structure is unstable and can be easily broken.

### *3.3.5  Occupancy of water molecules in CNTs*

The number of water molecules inside the CNTs increases significantly when the electric field is introduced (Table 3.2), confirming the previous work [52]. Moreover, the standard deviation of the number of water molecules under electric fields is smaller than that without electric fields. This is because under electric fields the water molecules form ordered structures and between the molecules are bonded by strong hydrogen bonds as explained in subsection 3.3.9. Therefore, the molecules are packed more tightly in the CNTs and the number of molecules less fluctuates.

**Table 3.2** Average number of water molecules inside CNTs. (with standard deviation).

| CNT | $E$ [V/nm] | Number of water molecules |
|---|---|---|
| (7,7) | 0 | 18.1 ± 1.9 |
| | 1 | 31.4 ± 0.7 |
| | 2 | 36.6 ± 0.8 |
| (8,8) | 0 | 35.9 ± 1.6 |
| | 1 | 47.7 ± 0.8 |
| | 2 | 49.6 ± 0.8 |
| (9,9) | 0 | 48.0 ± 2.5 |
| | 1 | 69.4 ± 1.1 |
| | 2 | 72.4 ± 1.0 |
| (10,10) | 0 | 66.3 ± 2.5 |
| | 1 | 85.2 ± 1.3 |
| | 2 | 96.7 ± 1.2 |

### 3.3.6 Lindemann index

The Lindemann index is an empirical rule that can be applied to estimate a melting point based on the amplitude of atomic vibrations relative to their average lattice constant position. Melting phenomenon takes place when the amplitude is sufficiently large to disturb the neighboring atoms and destroy the structure. As shown below, another way to determine the Lindemann index is based on fluctuations in the distance between a pair of atoms. Here, the local Lindemann index for $i$-th atom in the system is given by [102-105]:

$$\delta_i = \frac{1}{N-1} \sum_{j(\neq i)} \frac{\sqrt{\langle r_{ij}^2 \rangle - \langle r_{ij} \rangle^2}}{\langle r_{ij} \rangle} \tag{3.2}$$

and for the whole system,

$$\delta = \frac{1}{N} \sum_i \delta_i \tag{3.3}$$

where $r_{ij}$ is the distance between the $i$-th and $j$-th atoms, and $N$ is the number of atoms in the system.

Under electric fields, water molecules form ordered structures and move collectively inside CNTs. Hence, the fluctuation method is appropriate to determine the Lindemann index. Calculation of the Lindemann index was performed for every 100 ps and then the average over the entire simulation time was determined. The results are given in Table

3.3.

Generally, the melting transition occurs when the Lindemann index is in the range of 0.10 – 0.15. A smaller criterion of 0.03 – 0.05 has been reported for clusters, homo-polymers [103], and CNTs [105]. Since there are only three settings of the electric field, the criterion cannot be established here. However, as indicated in Table 3.3, when the electric field was applied, the Lindemann indices decrease to one order lower, which suggests a phase transition is occurred. This is in contrast to the water in the reservoir and in the bulk, where the electric field does not change the indices significantly. The average Lindemann index for the (8,8) and (9,9) CNTs under 0 V/nm is 0.3, although it is frequently as low as 0.1 (see Fig. 3.10). It indicates the formation of unstable (4,0) and (6,0) ice nanotubes. To distinguish the Lindemann index for the disordered and ordered structures in the (8,8) and (9,9) CNTs under 0 V/nm, the average of high (hi) and low (lo) indices was calculated (Table 3.3). The low index is defined as < 0.2; otherwise it is considered as high index.

**Table 3.3**  Lindemann indices for water molecules in CNTs, reservoir (Res.), and bulk. For (8,8) and (9,9) CNTs with 0 V/nm, there are high (hi) index and low (lo) indexes.

| $E$ [V/nm] | CNT (7,7) | CNT (8,8) | CNT (9,9) | CNT (10,10) | Res. | Bulk |
|---|---|---|---|---|---|---|
| 0 | 0.423 | hi: 0.296 lo: 0.145 | hi: 0.309 lo: 0.091 | 0.338 | 0.162 | 0.202 |
| 1 | 0.043 | 0.036 | 0.073 | 0.078 | 0.163 | 0.200 |
| 2 | 0.032 | 0.031 | 0.062 | 0.034 | 0.165 | 0.190 |

(a)



(b)



(c)



(d)
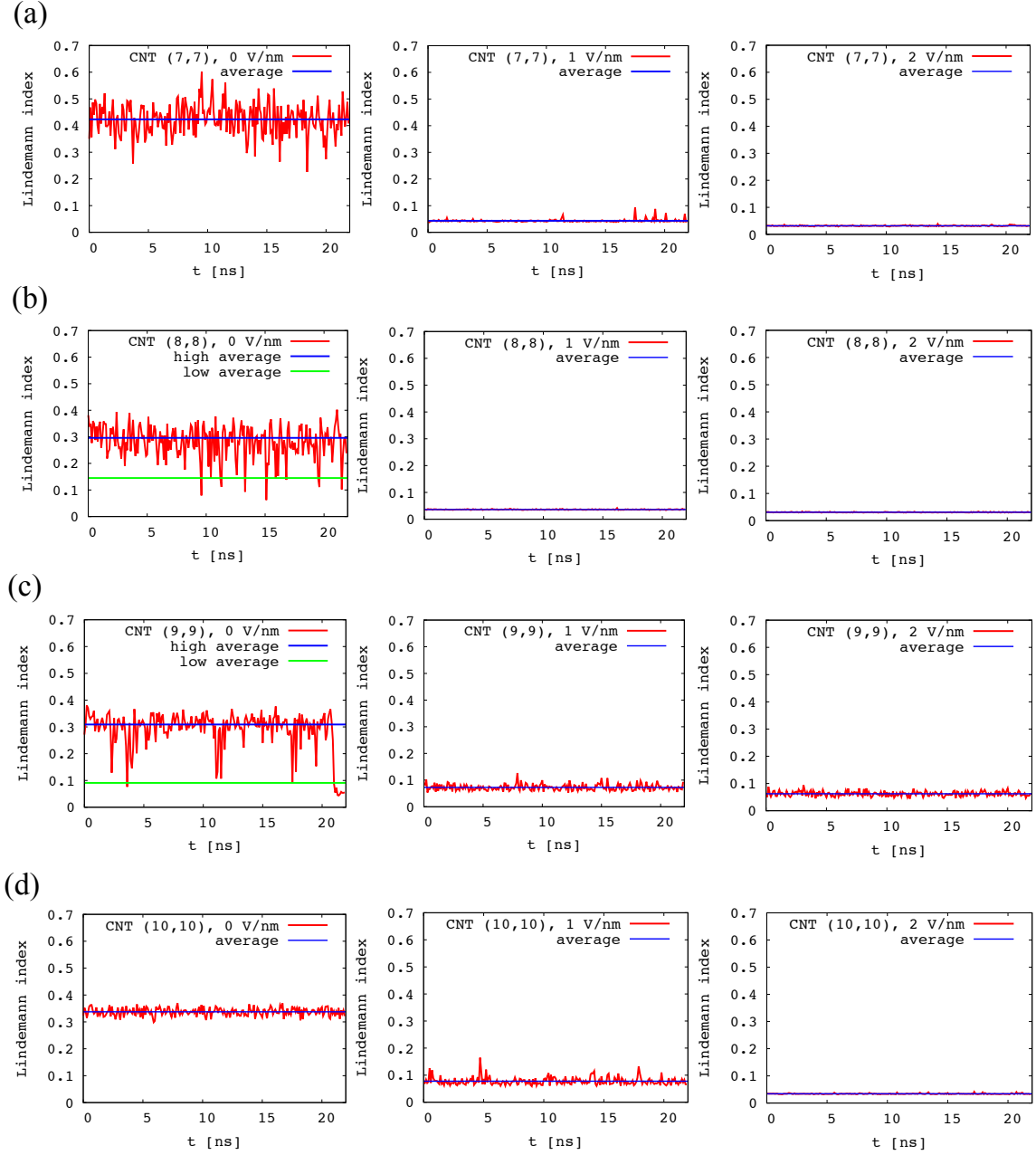


**Fig. 3.10** Time evolution of Lindemann index with 0, 1, and 2 V/nm: (a) in (7,7) CNT, (b) in (8,8) CNT, (c) in (9,9) CNT, and (d) in (10,10) CNT.

### 3.3.7  Diffusion coefficient

The diffusion coefficient $D_z$ of water molecules in a CNT is given by:

$$D_z = \lim_{t \to \infty} \frac{\left\langle \left| z(t) - z(0) \right|^2 \right\rangle}{2t}$$

(3.4)

where $z(t)$ is the axial position of a water molecule at time $t$, and $\langle ... \rangle$ denotes an

ensemble average. We exclude the water molecules exit from the CNTs out of the ensemble. In the absence of the electric field, the diffusion coefficient of water inside CNTs is in the same order as that in the reservoir and in the bulk (see Table 3.4). As expected, the diffusion coefficient decreases significantly under 1 V/nm; under 2 V/nm it decreases the magnitude to one order lower than that with no electric field.

The electric field slightly decreases the diffusion coefficient for water molecules in the reservoir and in the bulk. The dynamics of water molecules are affected by the electric field because its torque restrains the rotational motion of the molecules. As discussed above, the graphene walls can induce polarization that promotes the rotational motion in the reservoir to be different from that in the bulk. That is in good agreement with the diffusion coefficient analysis where water molecules in the reservoir have higher coefficients than does bulk water under the electric field.

**Table 3.4** Diffusion coefficients of water along axial direction ($D_z$) [$10^{-5}$ cm$^2$/s] in CNTs, reservoir (Res.), and bulk.

| $E$ [V/nm] | CNT (7,7) | CNT (8,8) | CNT (9,9) | CNT (10,10) | Res. | Bulk |
|---|---|---|---|---|---|---|
| 0 | 7.13 | 3.66 | 4.03 | 4.76 | 5.00 | 5.08 |
| 1 | 1.38 | 0.98 | 1.22 | 1.18 | 4.88 | 3.92 |
| 2 | 0.99 | 0.78 | 0.92 | 0.73 | 4.60 | 3.17 |

### 3.3.8  Orientational correlation function

Rotational dynamics of water molecules were analyzed with the orientational correlation function (OCF) $C_\theta(t) = \langle \boldsymbol{\mu}(0) \cdot \boldsymbol{\mu}(t) \rangle$, where $\boldsymbol{\mu}(t)$ is a unit of the dipole vector at time $t$. The OCF of water molecules are shown in Fig. 3.11. At 0 V/nm, water molecules in the reservoir and in the bulk rotate freely and the OCFs decay to zero within 20 ps (Fig. 3.11(a)). In the CNTs, even though the molecules can rotate 360°, they need a longer time to reach zero because of confinement by the CNT walls. In larger diameter CNTs where there is less confinement, the rotational dynamics are closer to that in the bulk. The OCF of (7,7) CNT decreases fast at the initial state and then decays more slowly than that of the other CNTs. This implies that water in (7,7) CNT oscillates rapidly within a narrow angle. However, it is more difficult to rotates 180° compared to water in the larger CNTs. Meanwhile, the torque from the electric field restrains the

rotational motion of water molecules. Under 2 V/nm, the OCF in the reservoir and in the bulk decays to constant values of 0.17 and 0.75, respectively (Fig. 3.11(b)). The constant OCFs that are > 0 implies that rotational motion occurs over < 180°. The reservoir OCF decays to a lower value than that in the bulk because water molecules in the reservoir can rotate over a wider angle. This is consistent with graphene walls inducing rotational motion due to the polarization and it also agrees with the fact that the diffusion coefficient in the reservoir is higher than that in bulk. Under electric fields, the OCFs for water in all the CNTs slightly decrease to a constant value of 0.9 in < 1 ps. This indicates that the water molecules rotate in very narrow angle and exhibit librational motions.
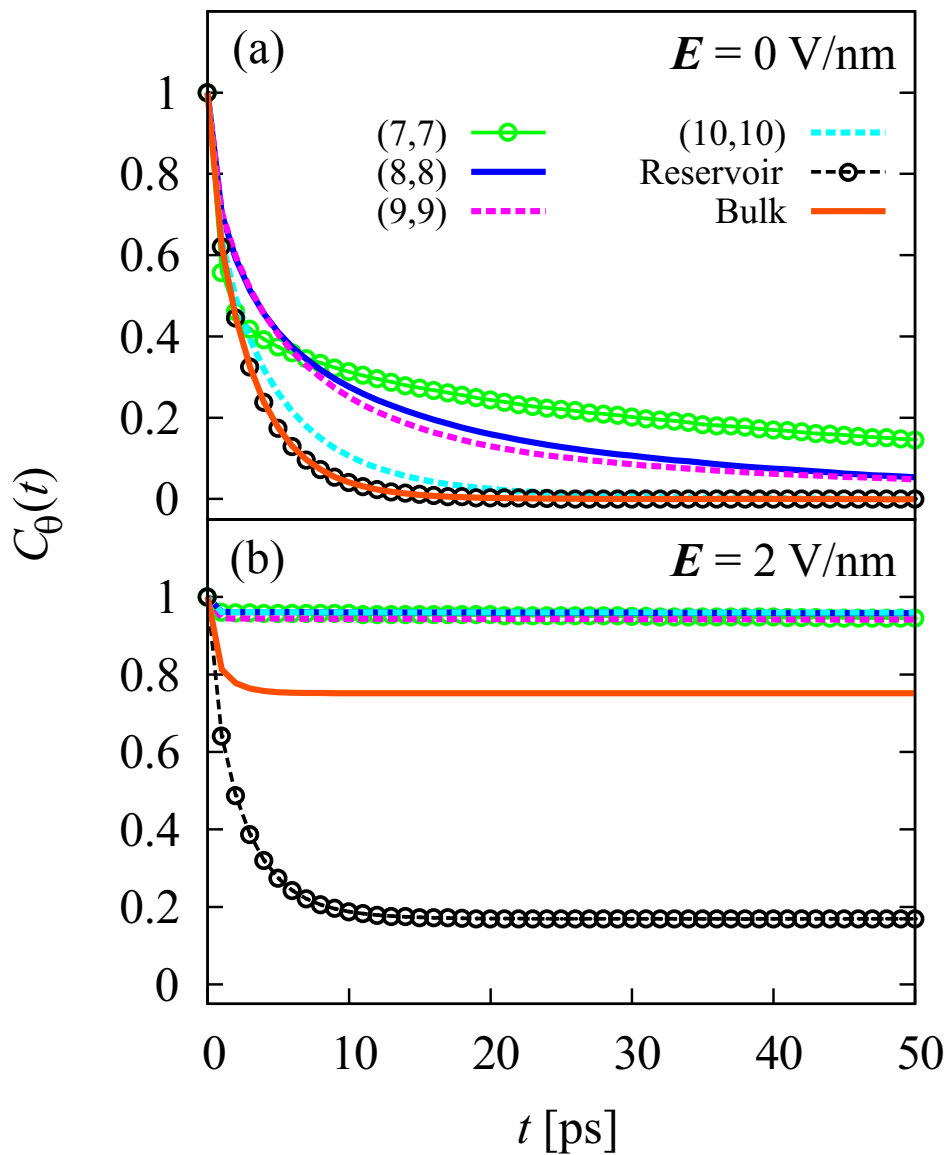


**Fig. 3.11** Rotational motion of water molecules. (a) OCF of water molecules inside the (7,7), (8,8), (9,9), (10,10) CNTs in the reservoir, and in the bulk under 0 V/nm, and (b) 2 V/nm.

### 3.3.9 Hydrogen bond dynamics

Hydrogen bonds (HBs) between water molecules are obtained with the following geometrical conditions [106,107]: the distance between the oxygen (O) atoms of the two molecules ($R_{OO}$) is < 0.36 nm; the distance between the O of the acceptor molecule and the hydrogen (H) atom of the donor ($R_{OH}$) is < 0.24 nm; and the angle between O-O direction and the O-H direction of the donor molecules is < 30°. Table 3.5 lists the average number of HBs per water molecule in bulk and in the reservoir. It is the same in the absence of the electric field. Under an electric field, when the dipole vector orientation is more uniform, the average number of HBs increases. Because the graphene wall induces rotation in the reservoir water molecules due to the polarization effect, and makes the direction of the dipole vector less uniform relative to that in bulk, the number of HBs in the reservoir is lower than that in the bulk.

**Table 3.5** Average number of hydrogen bonds per water molecule.

| $E$ [V/nm] | Bulk | Reservoir |
|:---:|:---:|:---:|
| 0 | 3.31 | 3.31 |
| 1 | 3.38 | 3.32 |
| 2 | 3.44 | 3.35 |

To investigate the dynamics of HBs, we calculate the HB autocorrelation function [108,109]:

$$C_{HB}(t) = \frac{\langle h(0)h(t)\rangle}{\langle h^2\rangle} \tag{3.5}$$

where $h(t) = 1$ if each pair of molecules (or pair of atoms) is bonded at time $t$ and $h(t) = 0$ otherwise. The denominator $\langle h^2\rangle$ is for normalization and is the number of HBs tagged at $t = 0$. In the calculation, a HB is not broken if it bonds the same pair of molecules; similarly, a HB is not broken if it bonds the same pair of atoms. Note that a HB can reform on the same pair of molecules but involve a different pair of atoms.

Figure 3.12 plots the behavior of HB dynamics in the CNTs. With an electric field, the HB autocorrelation functions based on a pair of molecules (dotted-lines) decrease slightly within 1 ps and then becomes constant. This indicates that the HB lifetime is very long and the water structures are strong. This also reduces the fluctuation in the

number of water molecules inside the CNTs (see Table 3.2). Moreover, the results reveal that librational motion breaks a few HBs which then reform again. If the HB autocorrelation functions are based on pair of atoms (bold-lines), they decrease quickly within 1 ps, and then decay slowly. This indicates that after a HB is broken, the molecules in the pair do not diffuse away from each other but remain adjacent. Thus, a HB can reform on the same pair of molecules. Because an HB can reform on the same pair of molecules, but involve a different pair of atoms, the HB autocorrelation functions decay when it is based on pair of atoms. Furthermore, these results support the notion that the water diffusion coefficients in CNTs (Table 3.4) are from collective translational motion.

There is no significant difference in the HB autocorrelation functions when comparing those based on molecules (dotted lines) or atoms (bold lines) for the (7,7) CNT under 2 V/nm and the (8,8) CNT under 1 V/nm and 2 V/nm. This implies that the structures are strong (stable). It differs for the case of the (7,7) CNT under 1 V/nm, where the function based on atoms decays significantly, indicating that the structure is less stable.

For the (9,9) CNT under 1 V/nm and 2 V/nm, and the (10,10) CNT under 1 V/nm, the HB autocorrelation function decreases to < 0.75 within 1 ps, which is lower than that for other cases under electric fields. This is consistent with the Lindemann index analysis where the indices of those cases are higher (more distance fluctuation) than the other cases (Table 3.3). Moreover, there are two water structures in those cases, and the inner structures are single lines. The HB autocorrelation function indicates that HBs are weaker between molecules in the single line structure on one side and molecules in the outer structure on the other side, or that HBs are weaker along the single line structure. It differs from the (10,10) CNT under 2 V/nm where the inner structure is an (2,2) ice nanotube, and the HB autocorrelation function shows that all HBs are stable.

Unlike axial electric field that strengthens the HBs, perpendicular electric field interrupts HBs structure in CNT [110]. Similar condition was exhibited by water molecules confined between two plates, where parallel electric field stabilizes monolayer ice structures [111], but perpendicular field melts the ice by disruption of the HBs structure [112].
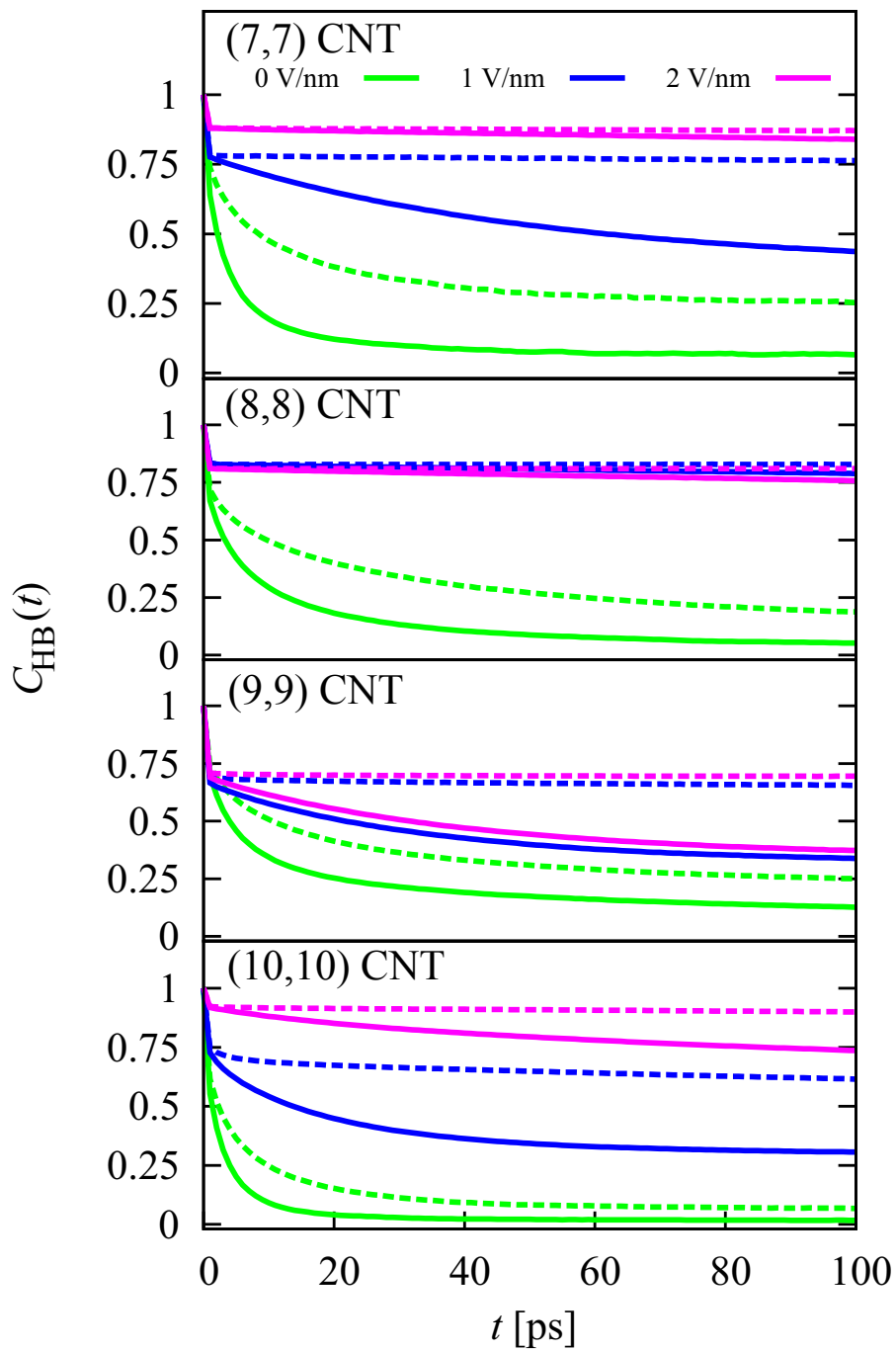
**Fig. 3.12** HB autocorrelation function for water molecules in CNTs under 0 V/nm (green), 1 V/nm (blue), and 2 V/nm (magenta). Bold and dotted curves are HB autocorrelation functions based on pairs of atoms or pairs of molecules, respectively.

_____

### 3.3.10  Permeation of water molecules

Permeation is defined here as the number of water molecules that enter a CNT on one side and then either remain inside or leave the CNT on the other side. We do not consider molecules entering and leaving at the same side. Table 3.6 lists estimated permeation rates for water molecules into CNTs under 0 V/nm, 1 V/nm, and 2 V/nm. Permeation from left and right sides are shown with L and R, respectively. They were obtained by plotting the number of molecules *vs.* time and then fitting a linear curve; the slope determines the permeation rate. As expected, the permeation rate decreases when the electric field is applied. This is consistent with the decreased diffusion coefficient in the axial direction in the presence of the electric field (Table 3.4). Moreover, permeation occurs at the both sides indicating no pumping to the electric field direction as seen in previous studies [83,84]. The permeation should be only from one side if the electric field generates pumping effect. This supports the finding that the pumping effect is caused by the force discontinuity from the Lennard-Jones cut off scheme [88,89]. The effect vanishes when the cut off is longer than 1.2 nm, while in this works 1.5 nm was applied.

Diffusion and permeation analyses verify that the ordered-structure water molecules can flow along the CNT. Therefore, we may conclude that their structure is like ice but they can flow like liquid.

**Table 3.6** Estimated permeation rates of water into CNTs [number of molecules/ns] under 0 V/nm, 1 V/nm, and 2 V/nm. L and R indicate permeation from left and right sides, respectively.

| $E$ [V/nm] | (7,7) CNT | | (8,8) CNT | | (9,9) CNT | | (10,10) CNT | |
|---|---|---|---|---|---|---|---|---|
| | L | R | L | R | L | R | L | R |
| 0 | 8.8 | 7.3 | 7.5 | 8.0 | 13.1 | 14.5 | 30.0 | 30.2 |
| 1 | 0.5 | 2.7 | 1.8 | 2.0 | 2.7 | 1.1 | 2.1 | 2.7 |
| 2 | 2.1 | 5.1 | 0.5 | 1.4 | 2.6 | 1.4 | 2.3 | 8.3 |

## 3.4 Conclusions

Electric field effects on systems of water, carbon nanotubes, and graphene sheets were investigated with MD simulation. The electric field reorients the dipole vector of the water molecules parallel to the field. The uniformity of molecular orientation facilitates water in CNTs to form ordered structures. Formation of the ordered structures then strengthens the hydrogen bond network, and hence the structures are more compact and contain more molecules. The density of water molecules inside the CNTs increases with an electric field. This indicates that water molecules favor to fill CNTs under the influence of the electric field. Moreover, we analyzed dynamical behavior of the water structures. Lindemann indices and diffusion coefficients decrease by one order of magnitude. Dynamic analysis of hydrogen bonding shows that molecules in a HB pair do not diffuse away from each other when the HB is broken, it remains close to each other instead. Thus, the electric field induces a liquid-to-solid phase transition in the CNTs.

Due to a strong HB, a pair of molecules is kept from diffusing away from each other, therefore the ordered water structures move collectively. This decreases the axial diffusion coefficient when an electric field is applied, and consequently, decreases the permeation of water molecules through CNTs as well.

The preference of water molecules to fill CNTs with an electric field is an interesting behavior and it may induce a separation effect. We investigate the effect of the electric fields on the separation of water–methanol mixtures and water–ethanol mixtures as presented in chapter 4 and 5, respectively.

# Chapter 4

# SEPARATION OF WATER–METHANOL WITH CARBON NANOTUBES AND ELECTRIC FIELDS

## 4.1  Introduction

Methanol is used as an alternative energy resource to reduce the use of fossil fuels consumption [113-115]. Methanol mixed with gasoline improves the thermal efficiency of engines and reduces the emission of exhaust gas [116-119]. Another application of methanol is in fuel cells to directly convert chemical energy to electric energy, and offers clean energy conversion [120-123]. In addition, methanol is important in chemical industrial processes [124].

As renewable energy, methanol can be produced by fermentation of biomass, such as corn, sugarcane, sorghum, and microalgae [125-128]. In the production processes, separation of methanol from aqueous solution is required. Conventionally, methanol is separated from aqueous solution by distillation, but this process consumes large amounts of energy [129,130]. Some alternative methods have been developed and applied, such as pervaporation [131-133], adsorption to zeolite [134-136], gas stripping [137], ionic liquids utilization [138,139], and filtering with nanotubes [140]. However, developing an innovative technique to enhance the effectiveness to separate methanol from aqueous solution is still a challenge.

In the recent years, carbon nanotubes (CNTs) have shown a promising performance as separation membranes for gas [39,40,141], desalination [10,36,37], gas–water [42], and organics–water separation [142]. Moreover, study regarding the separation of methanol from aqueous solution with CNTs has attracted considerable attention. Under a chemical potential gradient, methanol molecules flow through CNTs in preference to water molecules [143]. Modification of CNT hydrophobicity by attaching carboxyl acid (COOH) groups to the inner wall of the CNTs slightly increases the selectivity of methanol molecules over water molecules [143]. When CNTs are immersed in water–methanol solution, methanol molecules preferentially fill and occupy the CNTs over water molecules, resulting in a separation effect [144]. However, the selectivity

significantly decreases with the increase of CNT diameter [144]. Immersing CNTs in methanol and other alcohol solutions shows that the selectivity for alcohols over water in occupying CNTs also depends on the number of alcohol-carbon atoms [145].

Water confined in nanoscale space under electric field has many interesting properties, which is very important for nanotechnology and biological science. A significant number of studies concerning the effects of an electric field of the order up to 8 V/nm on water confined in CNTs and between two-plates were reported recently [52,53,86,87,111,146-148]. The strength of that field is still comparable with the typical field in biological transmembrane channels, which is 0.06 to 0.3 V/nm [46,47]. Moreover, various strategies to explore the field effects to develop nanofluidic devices have been reported as well. Nanopumping can be performed by employing a time-dependent, vibration, and rotating electric field [56,57,68,149]. Introducing an electric field along the CNT can enhance reverse osmosis for water purification [58]. The axial electric field can control the dynamics of water molecules in the CNT to induce flow [84]. As presented in chapter 3, an electric field induces formation of ordered structures and facilitates water to fill CNTs. These phenomena may enhance the separation effect for water–methanol solution with CNTs.

In this chapter, we investigated the separation of water and methanol from water–methanol solutions using CNTs with and without an axial electric field using molecular dynamics (MD) simulations. We investigated the effect of an electric field on the selectivity of a water-methanol mixture flowing into (6,6) to (30,30) CNTs. In the absence of an electric field, methanol molecules preferentially enter and occupy the CNTs over water molecules, resulting in a separation effect for methanol. However, a strong separation effect for methanol is observed only for the small CNT diameter and this effect considerably decreases with the increase of CNT diameter. In contrast, when an electric field is applied, water molecules strongly prefer to enter and occupy the CNTs over methanol molecules, which produces a separation effect for water. More importantly, the selectivity for water molecules does not depend on the CNT diameter, indicating a strong separation effect for water.

## 4.2  Simulation Method

Similar to Fig. 3.1 in the chapter 3, the simulation system consisted of a CNT, two graphene sheets, and water–methanol reservoirs on both sides (Fig. 4.1(a) and (b)), which differs from other studies [144,145]. In the simulation system, the length of the

CNT was 2.95 nm with various diameters: 0.81, 0.95, 1.08, 1.22, 1.36, 1.63, 2.03, 2.71, 3.39, and 4.07 nm for (6,6), (7,7), (8,8), (9,9), (10,10), (12,12), (15,15), (20,20), (25,25), and (30,30) CNTs, respectively. The reservoirs were filled with a mixture of water and methanol molecules. In the reservoirs, we considered mole fractions of water molecules ($\chi_{water}$) of 0.81 and 0.19, which are equivalent to 70% and 12% mass fractions, respectively. Periodic boundary conditions were applied in all directions (*x*, *y*, and *z* axes).

The SPC model [90] was used for water and the OPLS united-atom potentials [150,151] were employed for methanol. The OPLS united-atom force field has been widely used for molecular simulation studies [143,144,152]. The Lennard–Jones (LJ) parameters are $\sigma_O = 0.3166$ nm and $\varepsilon_O = 0.6500$ kJ/mol for the oxygen of water, $\sigma_C = 0.3400$ nm and $\varepsilon_C = 0.3612$ kJ/mol for carbon of the CNT, $\sigma_O = 0.3070$ nm and $\varepsilon_O = 0.7113$ kJ/mol for the oxygen of methanol, and $\sigma_{CH_3} = 0.3775$ nm and $\varepsilon_{CH_3} = 0.8661$ kJ/mol for $CH_3$ (methyl). The LJ parameters for determining the interactions between different atoms were calculated with the combination rule $\sigma_{ij} = (\sigma_i \sigma_j)^{1/2}$ and $\varepsilon_{ij} = (\varepsilon_i \varepsilon_j)^{1/2}$. A homogeneous electric field of up to $E = 2$ V/nm was applied in the direction of the positive *z* axis. Here, the magnitude of the electric field was still lower than the threshold value of $E = 3.5$ V/nm where dissociation of water molecules occurs [153], and within the range of an experimental study of graphene [154].

The MD simulations were carried out using GROMACS 4.5.5 software [91]. The van der Waals interactions were cut off at 1.5 nm, and electrostatics interactions were treated using the particle mesh Ewald method [92] with the real space cut off set to 1.5 nm. The length of the chemical bonds of the water and methanol molecules and the angles between the bonds were maintained at constant with the SHAKE algorithm [93]. The CNTs and graphene were made rigid by fixing the lengths and angles of the chemical bonds. The simulations were performed with $NL_xL_yP_zT$, where the temperature (*T*) was kept at 300 K with the Nosé–Hoover coupling scheme [94,95]. The pressure in the axial direction (*z* axis) was maintained at 0.1 MPa using the Parrinello–Rahman technique [96]. The time step was set to 2 fs and the simulations were run for a minimum of 25 ns. We observed time evolution of occupancy of molecules in the CNTs to determine equilibrium state of the systems. In general, the systems reached an equilibrium state within 2 ns.
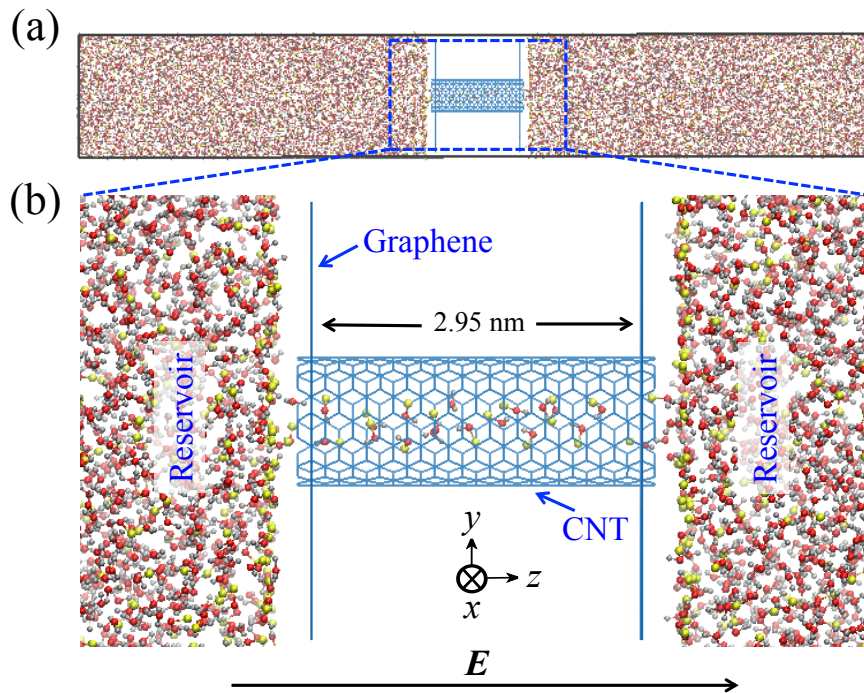
**Fig. 4.1**  (a) Molecular dynamics (MD) simulation system consists of two graphene sheets, a CNT, and reservoirs filled with a water–methanol mixture. (b) Magnified image of the MD system. A homogeneous electric field $E$ was applied in the $z$ axis direction.

## 4.3  Results and Discussion

### *4.3.1 Separation effect*

To determine the preferential occupancy of molecules in the CNTs, we calculated the mole fractions in the CNTs and compared them with those in the reservoirs, as shown in Fig. 4.2. With no electric field (*i.e.*, $E$ = 0 V/nm), $\chi_{water}$ in the CNTs is lower (or $\chi_{methanol}$ in the CNTs is higher) than that in the reservoirs for both $\chi_{water}$ = 0.81 and 0.19 (black dotted lines) in the reservoirs, as shown in Fig. 4.2(a) and (b), respectively. The preference for methanol molecules to occupy the CNTs over water molecules produces a separation effect for methanol. This separation effect is strong for the (6,6) CNT. However, it significantly decreases with the increase of CNT diameter, confirming the results of the previous study [144].

In contrast, with an electric field, water molecules occupy the CNTs in preference to methanol molecules. With $E$ = 0.25 V/nm, $\chi_{water}$ in the CNTs increases with the increase of CNT diameter. With the stronger electric fields of $E$ = 1 V/nm and 2 V/nm, $\chi_{water}$ = 1.0 for all CNT diameters (Fig. 4.2(a)). In Fig. 4.2(b), even though $\chi_{water}$ in the reservoirs is very low (0.19), $\chi_{water}$ = 1.0 in the CNTs with 2 V/nm for (6,6) to (15,15) CNTs. For

the larger CNT diameters, it slightly decreases to 0.95, 0.99, and 0.86 for (20,20), (25,25), and (30,30) CNTs, respectively. These results indicate that the electric field leads to a very strong preference for water molecules in the CNTs. As a result, it produces a strong separation effect for water. Moreover, the separation effect for water is strong for a wide range of CNT diameters. This is advantageous because practical synthesis of CNTs produces various diameter sizes, and not uniformly small CNTs [155-157].
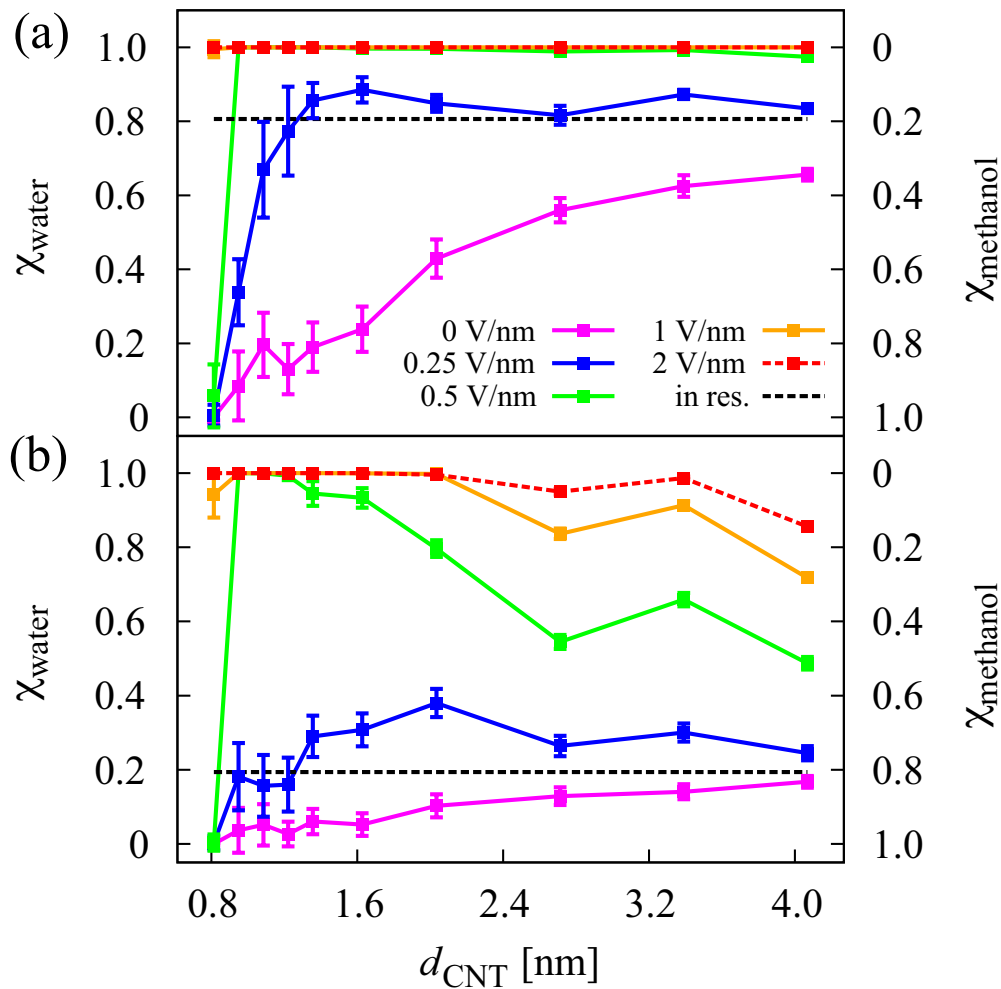


**Fig. 4.2** Mole fraction inside CNTs in the diameter range of 0.81–4.07 nm with **$E$** = 0, 0.25, 0.5, 1, and 2 V/nm. The left vertical axis shows the mole fraction of water molecules ($\chi_{water}$) and the right axis shows the mole fraction of methanol molecules ($\chi_{methanol}$). (a) $\chi_{water}$ = 0.81 (black dotted line) in the reservoirs and (b) $\chi_{water}$ = 0.19 (black dotted line) in the reservoirs. The error bars represent the standard deviation.

The separation effect for water in the CNTs is clear by plotting $\chi_{water}$ against $E$, as shown in Fig. 4.3. With $E = 0.25$ V/nm, the electric field effect is observed, where $\chi_{water}$ in the CNTs is high, except for CNT (6,6). For $E = 0.5$ V/nm, $\chi_{water} = 1.0$ in (7,7) to (30, 30) CNTs, but in the (6,6) CNT it is still very low (Fig. 3(a)). Similarly, for $\chi_{water} = 0.19$ in the reservoir and $E = 0.5$ V/nm, $\chi_{water}$ is high in all of the CNTs, except for the (6,6) CNT (Fig. 3(b)). The electric field effect in the (6,6) CNT is strong for $E \geq 1$ V/nm. The results in Fig. 4.3 show that for $E \leq 0.5$ V/nm the electric field effect on water–methanol separation in the (6,6) CNT is weaker than that in the other CNTs. Methanol molecules in the (6,6) CNT are more stable than water molecules, as seen in the case with no electric field. This strongly depends on the water molecule structure in the CNTs, which will be discussed in the following paragraph.
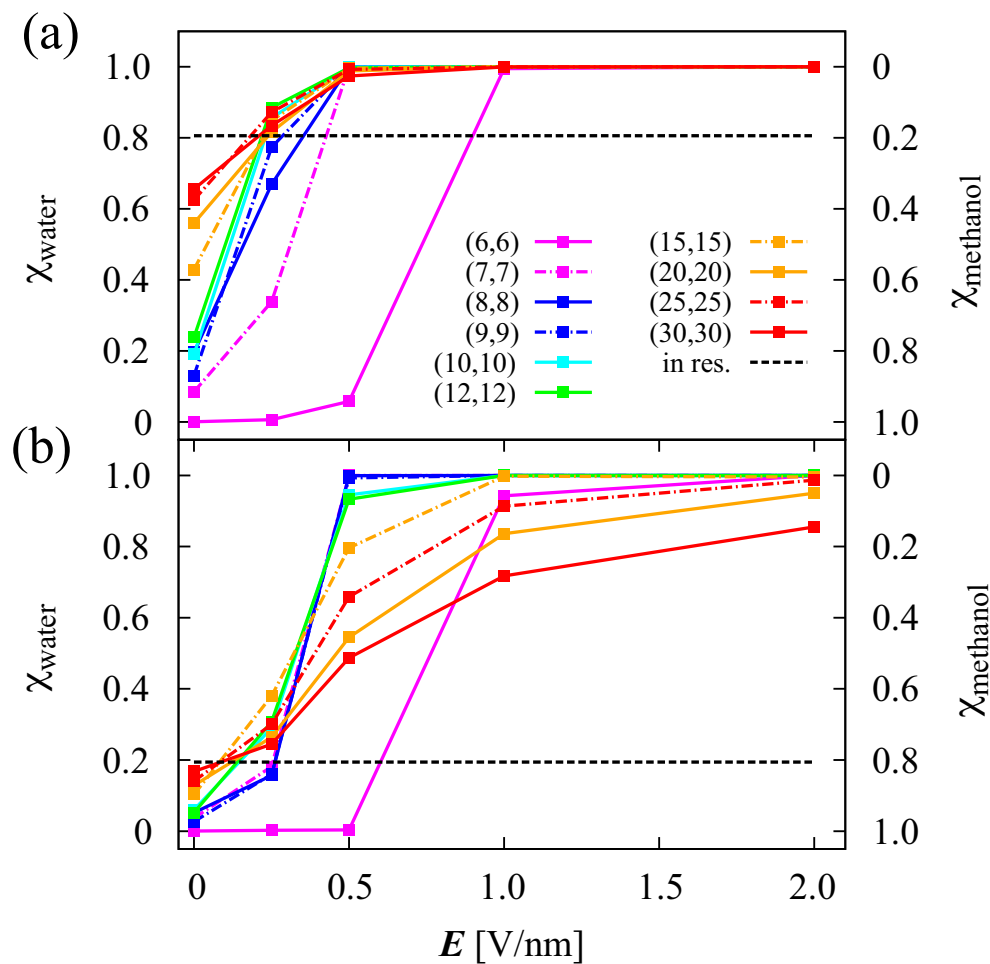


**Fig. 4.3** Dependency of $\chi_{water}$ (or $\chi_{methanol}$) on the electric field strength ($E$) in (6,6)–(30,30) CNTs. (a) $\chi_{water} = 0.81$ (black dotted line) in the reservoirs. (b) $\chi_{water} = 0.19$ (black dotted line) in the reservoirs.

_____

To determine the electric field effect on the mole fraction in the CNTs, we calculated the axial density distributions of the atoms around the original $z$ axis (Fig. 4.4). We considered water and methanol molecules in the region from 0 to $r_{CNT}$ (CNT radius), as shown by the dark area in Fig. 4.4(b). As shown in Fig. 4.4(a), for no electric field condition, the density of methanol molecules near the CNT entrance (vertical black dotted line) is much higher than that in the reservoir region. On the other hand, the density of water molecules is much lower than that in the reservoirs. This is because the van der Waals attraction between the CNT (and graphene) and methanol molecules is stronger than between the CNT (and graphene) and water molecules [144]. For $E = 0.25$ V/nm, the effect of the electric field on the mole fraction in the CNT occurs and $\chi_{water}$ increases (Fig. 4.4(b)). However, under these conditions, $\chi_{water}$ in the CNT is not uniform, where $\chi_{water}$ in the right region is higher than that in the left region. As expected, under an electric field, the density of methanol near the right entrance to the CNT is lower than that near the left entrance. On the other hand, the density of water near the right side is higher than that near the left side. That results in the higher $\chi_{water}$ in the right region of the CNT compared to that in the left region. Under an electric field, the dipole moments of water and methanol molecules are parallel to the field. The methyl group of methanol is far away from the right graphene sheet but close to the left graphene sheet. Thus, the van der Waals interactions between the right sheet and the methanol molecules are weaker. As a result, the density of methanol molecules near the right sheet is lower than that near the left sheet. This can affect the mole fraction in the CNTs. At the higher electric field of 1 V/nm, the condition changes completely, where the densities of water molecules near the entrances at both sides are much higher than that in the reservoir region (Fig. 4.4(c)). Consequently, only water molecules occupy the CNT.
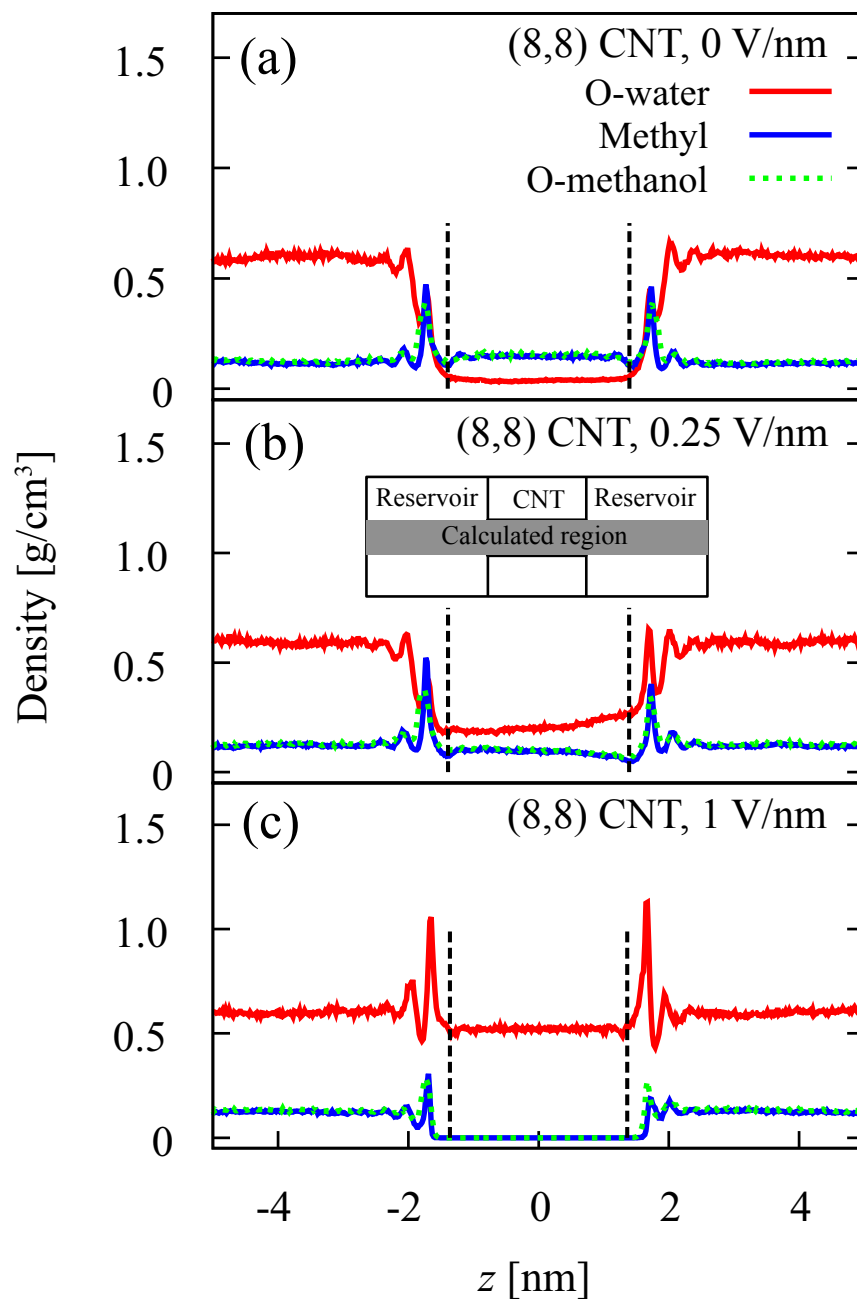
**Fig. 4.4** Axial density distribution of the atoms of water and methanol molecules: (a) $E = 0$ V/nm, (b) $E = 0.25$ V/nm, and (c) $E = 1$ V/nm. The simulation system was a (8,8) CNT with $\chi_{water} = 0.81$ in the reservoirs. Only the region from $0 - r_{CNT}$ (CNT radius) from the center axis in the $z$ direction was considered in the calculation, as shown by the dark area. The vertical black dotted lines show the positions of the graphene sheets. O-water and O-methanol denote oxygen atoms of water and methanol, respectively.
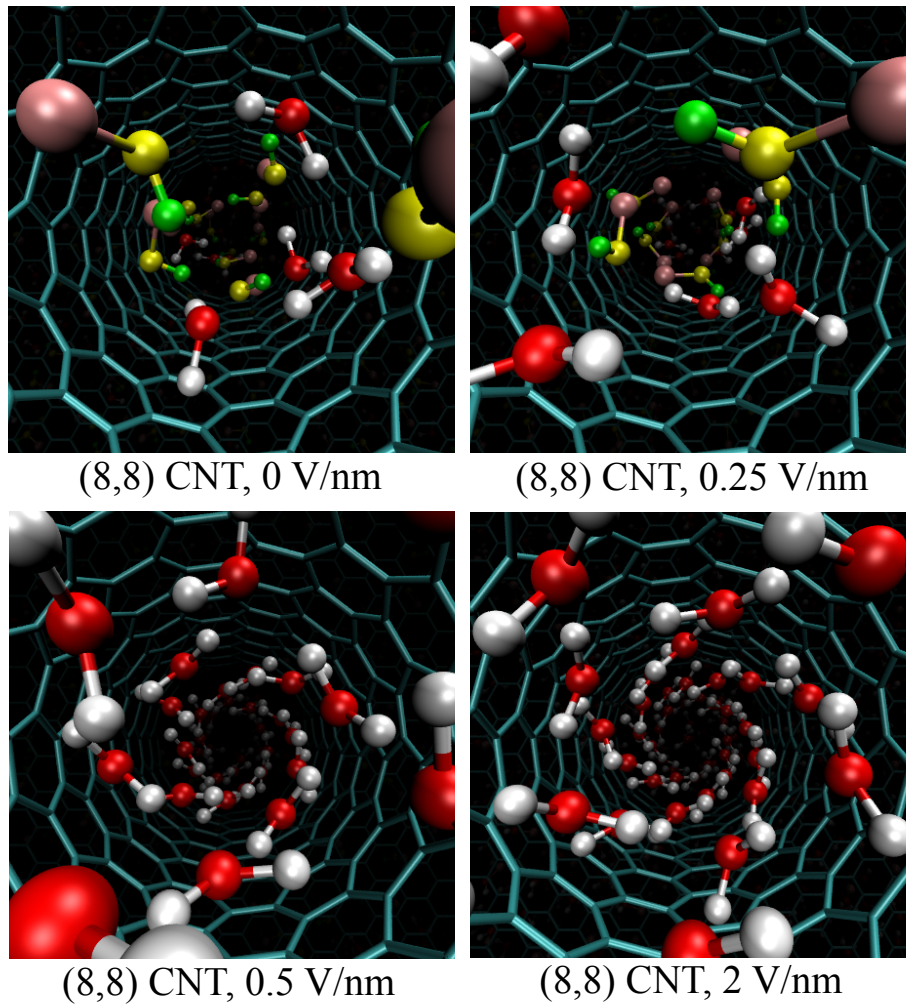
### *4.3.2 Structure of molecules in CNTs*

Figure 4.5 shows snapshots of the structures of molecules in the (8,8) CNT with $E = 0, 0.25, 0.5$, and 2 V/nm. With $E = 0$ and 0.25 V/nm, both water and methanol molecules occupy the CNTs. At the stronger electric fields ($E = 0.5$ and 2 V/nm), only water molecules occupy the CNT. Interestingly, the water molecules form helical structures, which are ordered solid-like structures. These structures are ice nanotube structures induced by the electric fields as shown in Fig. 3.8 (chapter 3, subsection 3.3.4). As explained in the chapter 3, the dipole moments of water molecules align parallel to the electric field, inducing the formation of ordered solid-like structures and increasing the density of water molecules in the CNTs. Although the water molecules form solid-like structures in the CNTs, permeation analysis showed that they can flow like liquid (see subsection 3.3.10). The formation of ordered structures induced by an electric field plays an important role in the separation of water–methanol solution. The ordered structures can be helical or non-helical, depends on the CNT diameter and strength of the electric field. As an example, the structure in (10,10) CNT with 1 V/nm is helical, and with 2 V/nm it is not helical where the structure index is $n = m$. Snapshots of structures in (7,7) to (30,30) CNTs with 2 V/nm are shown in Fig. 4.6.

To investigate the formation of the ordered structures, we calculated the radial density distributions of the atoms in the CNTs. For the (8,8) CNT with $E = 0.25$ V/nm, $\chi_{water} = 0.67$ in the CNT (Fig. 4.7(a) and (b)). Water and methanol molecules are concentrated in a narrow region around the center axis of the CNT. The orthographic projection of the snapshot in Fig. 4.7(b) confirms the results. With no electric field condition, the radial density distribution shows the same tendency as $E = 0.25$ V/nm (Fig. 4.8(a) and (b)). For an electric field of $E \geq 0.5$ V/nm, the width of the peak of the distribution is narrower and the peak position shifts towards the CNT (see Fig. 4.9(a), (b)).

An electric field aligns the orientation of the water and methanol molecules. For the water molecules, because they have the same orientation and are close together, it is easy to form an ordered hydrogen bonded network. Unlike water molecules, methanol molecules are not symmetrical. Moreover, for bulk methanol, hydrogen bonds form between the oxygen and hydrogen atoms only, while it is difficult for the methyl groups to form hydrogen bonds [158,159]. Thus, methanol molecules in the CNTs cannot form an ordered hydrogen bonded network with all of their atoms, such as the one formed by water molecules. The number of hydrogen bonds per methanol molecule in the methanol

molecule structure is less than the number of hydrogen bonds per water molecule in the water molecule structure. In other words, the water molecule structures are more stable than the methanol molecule structures in CNTs under an electric field.



| (8,8) CNT, 0 V/nm | (8,8) CNT, 0.25 V/nm |
| (8,8) CNT, 0.5 V/nm | (8,8) CNT, 2 V/nm |

**Fig. 4.5** Structures of molecules in the (8,8) CNT with $E$ = 0, 0.25, 0.5, and 2 V/nm. Red and white atoms denote water molecules. Methanol molecules are represented by yellow, green, and pink for oxygen, hydrogen, and methyl, respectively. $\chi_{water}$ = 0.81 in the reservoirs.

(a)
(b)

(7,7) CNT, 2 V/nm

(9,9) CNT, 2 V/nm

(c)
(d)

(10,10) CNT, 2 V/nm

(12,12) CNT, 2 V/nm

(e)
(f)

(15,15) CNT, 2 V/nm

(20,20) CNT, 2 V/nm

(g)
(h)

(25,25) CNT, 2 V/nm

(30,30) CNT, 2 V/nm
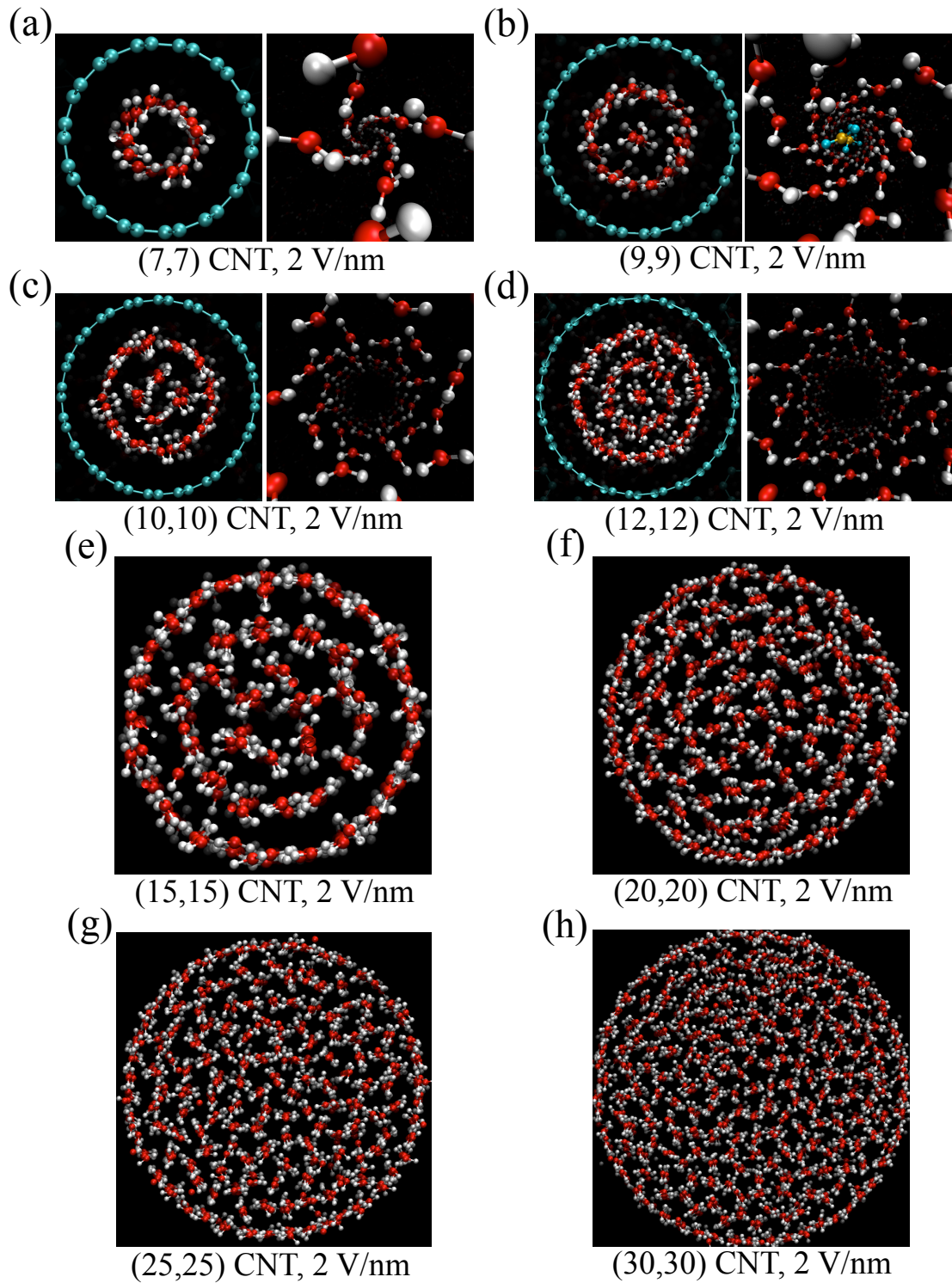
**Fig. 4.6** Snapshots of water molecules in CNTs under 2 V/nm of electric filed. The simulation condition is $\chi_{water}$ = 0.81 in reservoirs. (a) in (7,7) CNT with orthographic and perspective projections for the left and the right figures, respectively. Water molecules form helical structure. (b) in (9,9) CNT, water molecules have outer and inner structures. The outer structure is helical and the inner one is single-file structure as shown with orange and blue colors in the right figure. (c) in (10,10) CNT, water molecules form double-walls structure. The outer structure is not helical (the right figure). (d) in (12,12) CNT, the outer structure is not helical (the right figure). (e) to (h) in (15,15), (20,20), (25,25) and (30,30) CNTs, respectively. Water molecules form multi-walls structures.
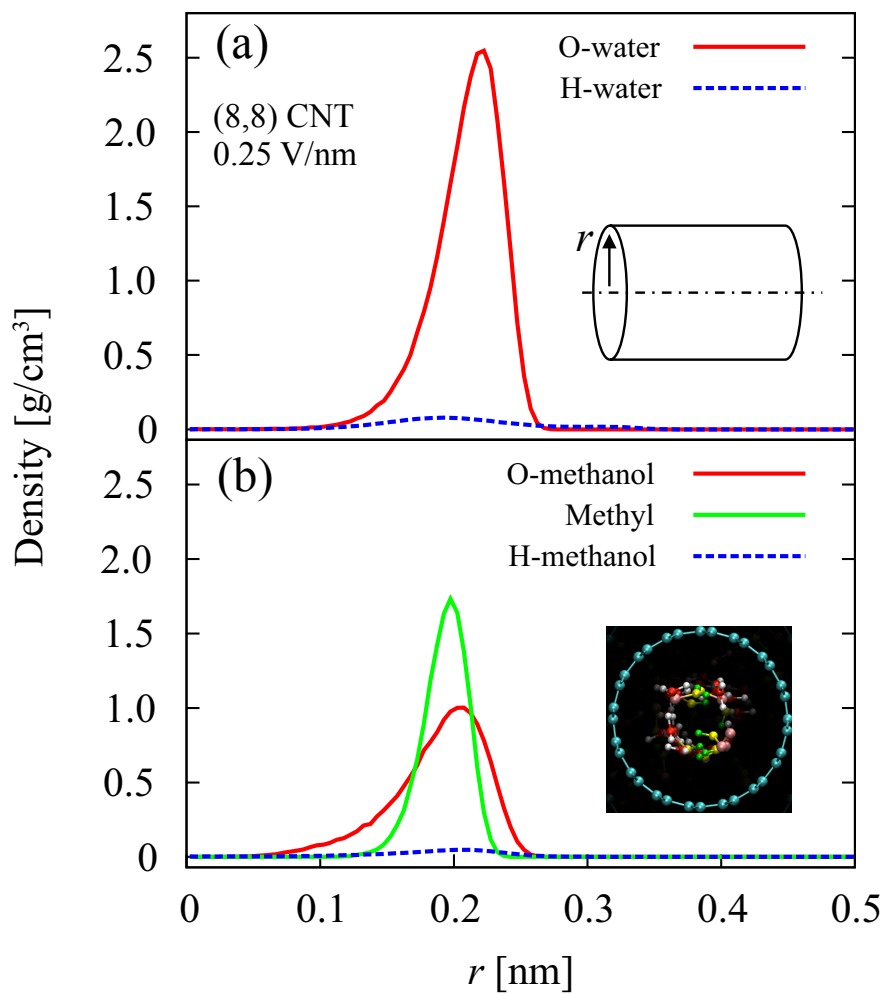
**Fig. 4.7**  Radial density distribution of atoms in the (8,8) CNT with $E$ = 0.25 V/nm and $\chi_{water}$ = 0.81 in the reservoirs for (a) water molecules, and (b) methanol molecules. O-water, H-water, O-methanol, and H-methanol indicate oxygen and hydrogen atoms of the water and methanol molecules. Only one hydrogen atom of every water molecule was considered for the calculation. Water and methanol molecules are concentrated in a narrow region in the radial direction, as confirmed by the snapshot in (b).
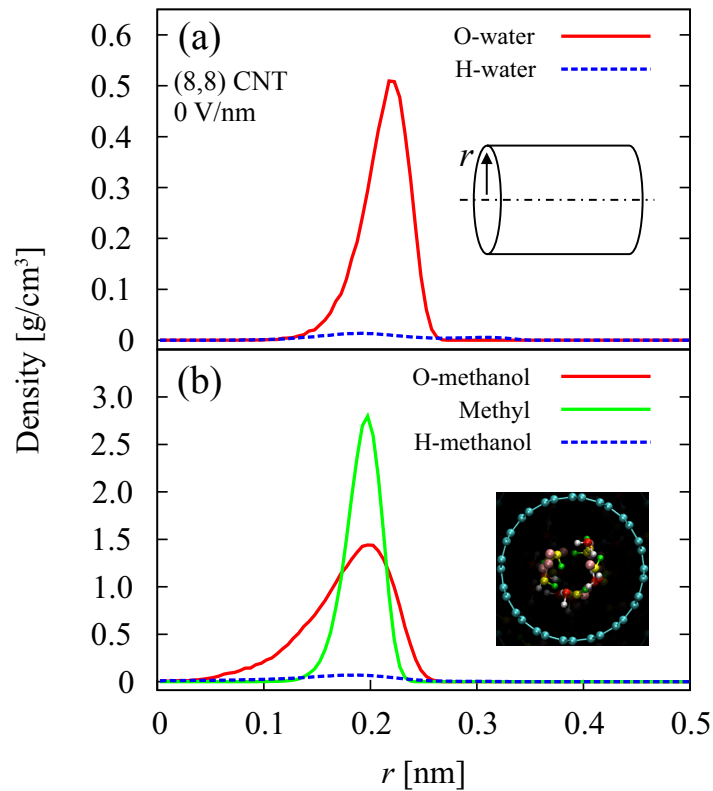
**Fig. 4.8** Radial density distribution of atoms in (8,8) CNT with 0 V/nm, (a) for water molecules, and (b) for methanol molecules. $\chi_{water}$ = 0.81 in reservoirs.
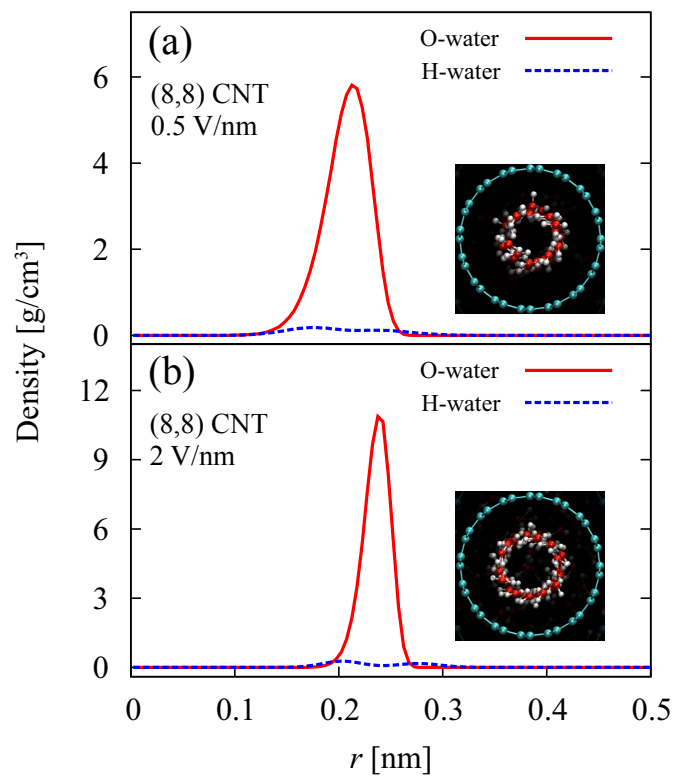


**Fig. 4.9** Radial density distribution of water molecules in (8,8) CNT, (a) with 0.5 V/nm, and (b) with 2 V/nm. $\chi_{water}$ = 0.81 in the reservoirs.

_____

Two-dimensional (2D) structures of the molecules in the (8,8) CNT for $E$ = 0, 0.25, and 0.5 V/nm are shown in Fig. 4.10. All of the atoms in the CNT were radially projected on the tube surface, as shown in Fig. 4.7. The 2D structures were obtained by unrolling the tube. The directions of the dipole moments of both water and methanol molecules with $E$ = 0.25 V/nm are more uniform than the one with no electric field. For $E$ = 0.25 V/nm, it is noticeable that the water molecules begin to form a hydrogen bonded network, whereas methanol molecules form a linear hydrogen bonded structure where only the oxygen and hydrogen atoms form hydrogen bonds with neighboring molecules. The methyl groups do not contribute the hydrogen bonded network. With $E$ = 0.5 V/nm, the density of water molecules in the CNT increases compared to the one with no electric field, and they form an ordered hydrogen bonded network with the (4,2) ice nanotube structure.

Under an electric field and confined between the CNT walls, the water molecule structures in the CNTs are stable. Moreover, the electric field increases the density of water molecules in the CNTs compared to the one with no electric field. This removes methanol molecules from the CNTs, and the methanol molecules cannot disrupt the water structures to permeate into the CNTs from the reservoirs. Confinement between the CNT walls is weaker with the increase of CNT diameter. The stability of the water structures decreases with the increase of CNT diameter. As a result, the separation effect for water decreases with the increase of CNT diameter (Fig. 4.2(b)).
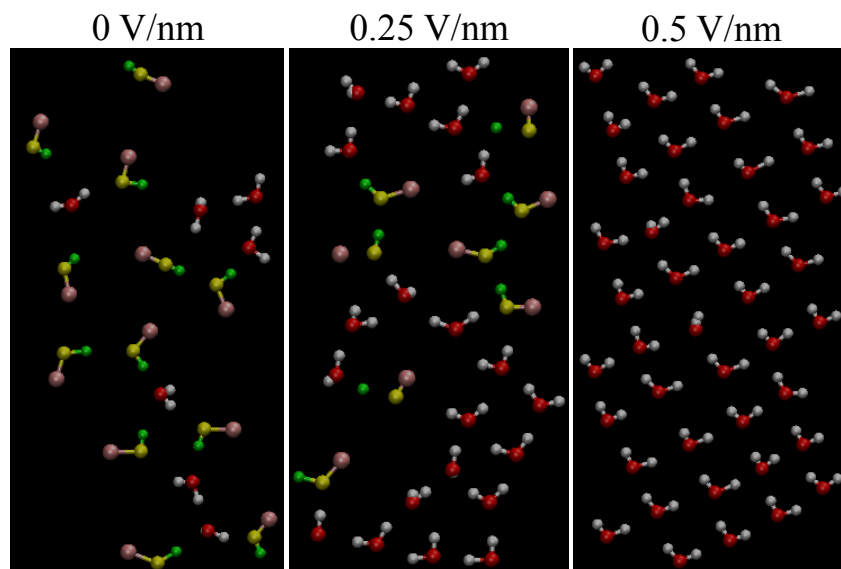


**Fig. 4.10** Two-dimensional structures of molecules in the (8,8) CNT for $E$ = 0, 0.25 and 0.5 V/nm. $\chi_{water}$ = 0.81 in the reservoirs.

Figure 4.3 shows that the separation effect for water with an electric field of $E \leq 0.5$ V/nm in the (6,6) CNT is weaker than that in the larger CNTs. The water structure in a narrow CNT, such as (6,6) CNT, is a single-file structure [4,160,161]. This implies that water molecules form a linear hydrogen bonded structure. Only one hydrogen atom of a water molecule forms a hydrogen bond with another water molecule. Thus, the maximum number of hydrogen bonds per water molecule is two. This differs from the water structures in the wider CNTs, where both hydrogen atoms of a water molecule can form hydrogen bonds with other molecules, generating a stable water structures. As a result, the separation effect for water in the (6,6) CNT with $E \leq 0.5$ V/nm is weaker than that in the larger CNTs (Fig. 4.3). With $E \geq 1$ V/nm, the water structure in the (6,6) CNT is a zig-zag single-file structure (see Fig. 4.11). As shown in Fig. 4.11, for $E = 0 - 0.5$ V/nm, methanol molecules prefer to fill the (6,6) CNT with single-file structures. For $E = 1$ V/nm, water molecules occupy the CNT and form a zig-zag structure instead of methanol molecules. The dipole moments of the water molecules are aligned parallel to the electric field with hydrogen bonds between water molecules, which builds a more stable structure than methanol molecule structures. At a stronger field of $E = 2$ V/nm, the density of water molecules in the CNT is higher than with weaker electric fields.

## (6,6) CNT, 0 V/nm

## (6,6) CNT, 0.25 V/nm

## (6,6) CNT, 0.5 V/nm

## (6,6) CNT, 1 V/nm

## (6,6) CNT, 2 V/nm
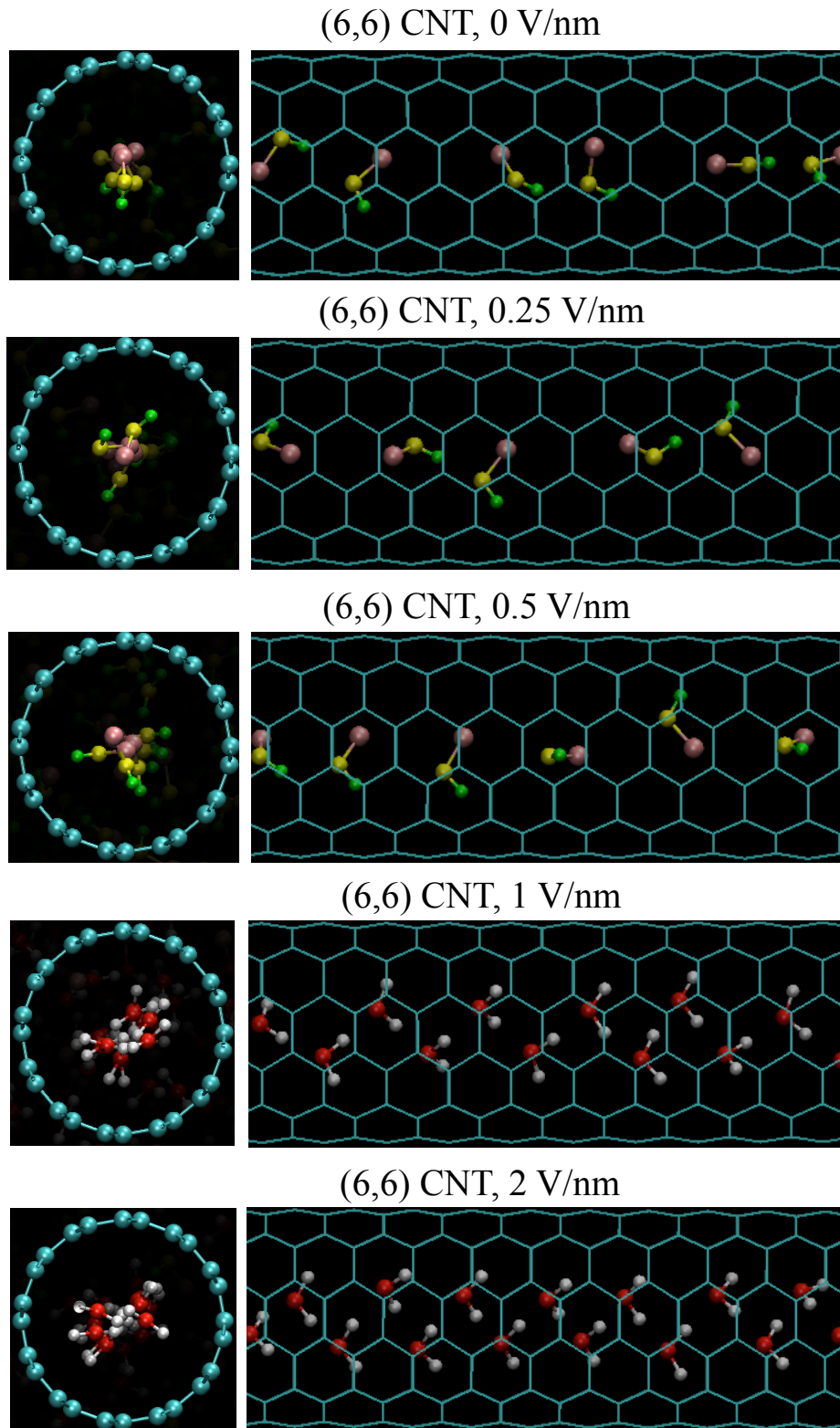
**Fig. 4.11** Structures of molecules in (6,6) CNT, with 0, 0.25, 0.5, 1, and 2 V/nm. Methanol molecules are represented with yellow, green, and pink for oxygen, hydrogen, and methyl, respectively. Water molecules are red and white for oxygen and hydrogen. With 1 and 2 V/nm, water molecules prefer to fill the CNT and they form zig-zag single-file structure. $\chi_{water}$ = 0.81 in the reservoirs.

### *4.3.3 Comparison of electric field effects on water and methanol molecules in CNTs*

To clarify the separation effect, we compared the effects of axial electric fields on the water molecules and methanol molecules in the CNTs. We performed additional simulations by filling the reservoirs with methanol molecules only (the system consisted of a CNT, methanol, and graphene). Then, we compared the dipole moment orientation, occupancy of molecules in CNTs, potential energies, structures, and hydrogen bond network with those of water. The dipole moment orientation, occupancy, and structures for the water molecules have been presented in the chapter 3.

a)  Orientation of dipole moment

Figure 4.12 shows direction of dipole moment for methanol molecules in (6,6) and (8,8) CNTs with 0, 1, and 2 V/nm. The direction of dipole moment is represented with angle $\alpha$, which is the angle between the dipole moment $\boldsymbol{\mu}$ and an electric field $\boldsymbol{E}$. The vertical axis denotes probability distribution function (PDF). With 0 V/nm, the peaks are at $\cos \alpha = -1$ and 1 for (6,6) CNT and $-0.8$ and 0.8 for (8,8) CNT. This suggests the dipole moment of methanol molecules in the CNTs has two orientations that are opposite to each other. With an electric field, the peak of $\cos \alpha$ is shifted to 1 implying the direction of the dipole moment tends to be parallel to that of the electric field. This is the same effect as for the water molecules where an electric field aligns the direction of the dipole moment parallel to that of the electric field.

b)  Occupancy of molecules in CNTs

The numbers of methanol molecules inside CNTs are shown in Table 4.1. The occupancy of methanol molecules in the CNTs increases with the electric field even in a small (6,6) CNT. Hence, same as the water molecules, an electric field causes the methanol molecules to preferably fill the CNTs.
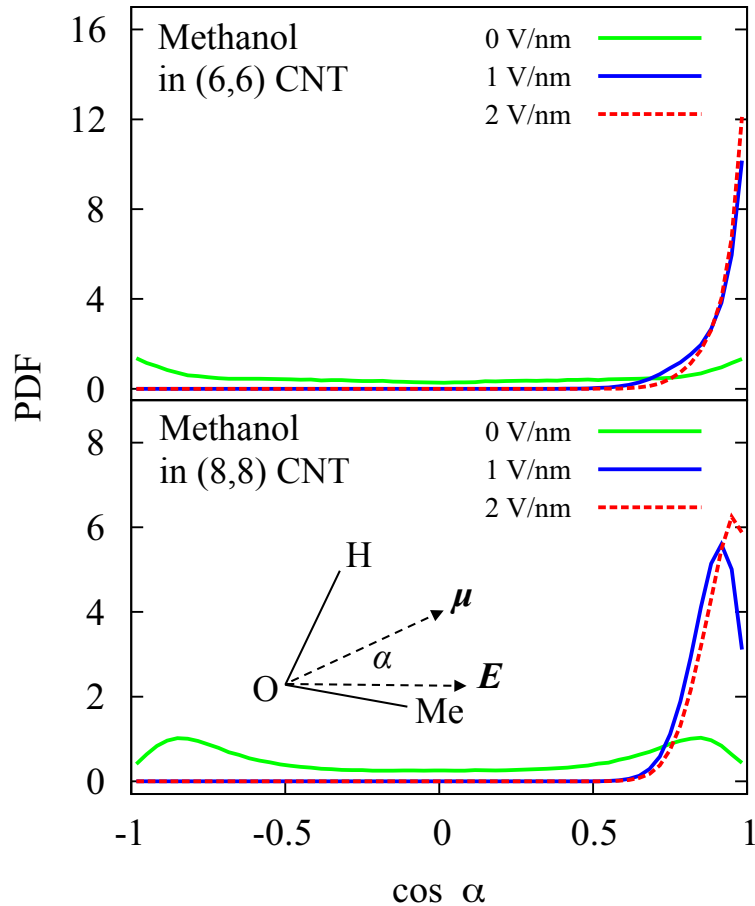
**Fig. 4.12** Effect of electric fields on the dipole moment orientation of methanol molecules in (6,6) and (8,8) CNTs. Direction of the dipole moment is indicated with angle $\alpha$, which is the angle between the dipole moment $\boldsymbol{\mu}$ and an electric field $\boldsymbol{E}$. O, H, and Me represent oxygen, hydrogen, and methyl, respectively. The vertical axis shows probability distribution function (PDF). Under an electric field, direction of dipole moment tends to be parallel to that of the field.

**Table 4.1** Average numbers of methanol molecules in CNTs. (with standard deviation)

| $E$ [V/nm] | (6,6) CNT | (8,8) CNT | (10,10) CNT |
|---|---|---|---|
| 0 | 6.4 ± 0.5 | 16.7 ± 1.1 | 29.6 ± 1.3 |
| 1 | 7.0 ± 0.4 | 19.7 ± 0.7 | 36.8 ± 1.2 |
| 2 | 6.7 ± 0.5 | 19.3 ± 0.7 | 37.6 ± 1.1 |

c) Potential energy

• *Lennard-Jones potential energy*

To compare the effect of CNT wall on the water and methanol molecules, we calculated the Lennard-Jones (LJ) potential energy per molecules in the reservoirs and in the (8,8) CNT. Distributions of the LJ potential energy for water and methanol molecules

with 0 and 2 V/nm are shown in Fig. 4.13(a) and (b), respectively. The difference of the LJ potential energy in the CNT and in the reservoir ($\Delta U_{LJ} = U_{LJ,\,CNT} - U_{LJ,\,res}$) indicates the van der Waals interaction of the water–CNT and the methanol–CNT (see Table 4.2 and 4.3). At 0 V/nm, $\Delta U_{LJ}$ for the water molecules is higher than that for the methanol molecules, which are −10.37 kJ/mol and −18.23 kJ/mol, respectively. This suggests that the van der Waals attraction for the methanol–CNT is stronger than that for the water–CNT. At 2 V/nm, $\Delta U_{LJ}$ for the methanol increases to −12.87 kJ/mol. This implies that the attraction of methanol–CNT decreases slightly with the electric field. At 0.5 V/nm, attractive interaction of water–CNT decreases compared to that at 0 V/nm. In contrast, with 1 and 2 V/nm, $\Delta U_{LJ}$ for water shift to positive values *i.e.* 0.90 and 6.29 kJ/mol, respectively, denoting repulsive interactions between the water and CNT. Thus, we can conclude that the preferential occupancy of the water molecules over the methanol molecules in the CNT with an electric field is not the consequence of the van der Waals interaction between the water and the CNT. The result suggests that the electrostatic interaction (hydrogen bond network) in the water molecules structure is the key factor for the separation effect with the electric field.
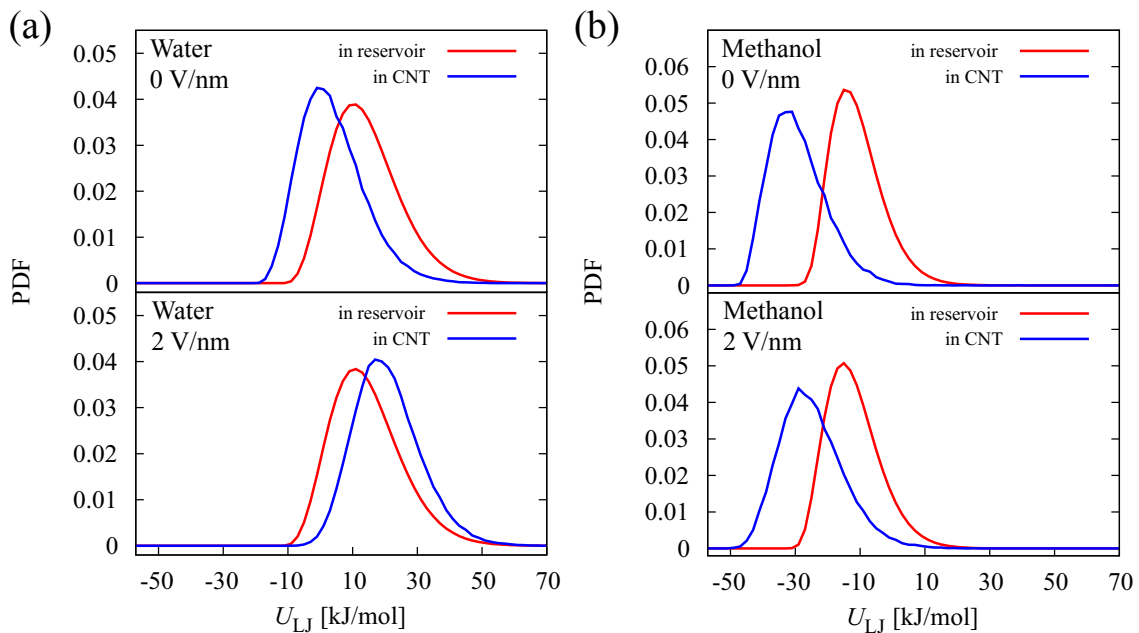


**Fig. 4.13** Distribution of the Lennard-Jones (LJ) potential energy for molecules in the reservoirs and in the (8,8) CNT with 0 and 2 V/nm; (a) for water molecules, and (b) for methanol molecules. The difference of the LJ potential energy in the CNT and in the reservoirs ($\Delta U_{LJ} = U_{LJ,\,CNT} - U_{LJ,\,res}$) indicates the van der Waals interaction of water–CNT and methanol–CNT. The $\Delta U_{LJ}$ for the methanol is lower than that for the water. This implies that the van der Waals attraction of the methanol–CNT is stronger than that of the water–CNT.

**Table 4.2** Average potential energies per molecule in the reservoirs and in (8,8) CNT for water with 0, 0.5, 1, and 2 V/nm. $\Delta U$ is the difference between the potential energy in the CNT ($U_{CNT}$) and in the reservoirs ($U_{res}$).

| $E$ [V/nm] | Energy ($U$) | in Reservoir [kJ/mol] | in CNT [kJ/mol] | $\Delta U = U_{CNT} - U_{res}$ [kJ/mol] |
|---|---|---|---|---|
| 0 | LJ | 14.08 | 3.71 | −10.37 |
| | Coulomb | −97.20 | −85.07 | 12.13 |
| | | | Total : | 1.76 |
| 0.5 | LJ | 14.12 | 5.50 | −8.62 |
| | Coulomb | −97.21 | −98.36 | −1.15 |
| | Dipole | −0.29 | −2.12 | −1.83 |
| | | | Total : | −11.60 |
| 1 | LJ | 14.20 | 15.10 | 0.90 |
| | Coulomb | −97.30 | −115.71 | −18.41 |
| | Dipole | −1.05 | −4.22 | −3.17 |
| | | | Total : | −20.68 |
| 2 | LJ | 14.52 | 20.81 | 6.29 |
| | Coulomb | −97.46 | −129.01 | −31.55 |
| | Dipole | −3.76 | −8.82 | −5.06 |
| | | | Total : | −30.32 |

**Table 4.3**  Average potential energies per molecule in the reservoirs and in (8,8) CNT for methanol with 0, 0.5, 1, and 2 V/nm. $\Delta U$ is the difference of the potential energy in the CNT ($U_{CNT}$) and in the reservoirs ($U_{res}$).

| $E$ [V/nm] | Energy ($U$) | in Reservoir [kJ/mol] | in CNT [kJ/mol] | $\Delta U = U_{CNT} - U_{res}$ [kJ/mol] |
|---|---|---|---|---|
| 0 | LJ | −10.87 | −29.10 | −18.23 |
|  | Coulomb | −59.68 | −52.17 | 7.51 |
|  |  |  | Total : | −10.72 |
| 0.5 | LJ | −11.06 | −28.37 | −17.31 |
|  | Coulomb | −59.98 | −66.19 | −6.21 |
|  | Dipole | −0.73 | −1.92 | −1.19 |
|  |  |  | Total : | −24.71 |
| 1 | LJ | −11.41 | −25.99 | −14.58 |
|  | Coulomb | −60.61 | −74.18 | −13.57 |
|  | Dipole | −2.50 | −3.93 | −1.43 |
|  |  |  | Total : | −29.58 |
| 2 | LJ | −11.93 | −24.80 | −12.87 |
|  | Coulomb | −62.08 | −80.05 | −17.97 |
|  | Dipole | −6.76 | −8.06 | −1.30 |
|  |  |  | Total : | −32.14 |

- *Coulomb potential energy*

Figure 4.14(a) and (b) show distribution of the Coulomb potential energy in the reservoirs and in (8,8) CNT for water and methanol molecules, respectively. The Coulomb potential energy for water and methanol in the CNT decreases significantly with the electric field. The difference of the Coulomb potential energy in the CNT and in the reservoirs ($\Delta U_{coulomb} = U_{coul., CNT} - U_{coul., res}$) for water decreases from 12.13 kJ/mol to −1.15, −18.41, and −31.55 kJ/mol with 0, 0.5, 1, and 2 V/nm, respectively (Table 4.2). $\Delta U_{coulomb}$ for methanol decreases as well from 7.51 kJ/mol to −6.21, −13.57, and −17.97 kJ/mol with 0, 0.5, 1, and 2 V/nm, respectively (Table 4.3). These results reveal that under the electric field, the electrostatic interaction within the molecules structure in the CNT facilitates water and methanol molecules to fill the CNT.
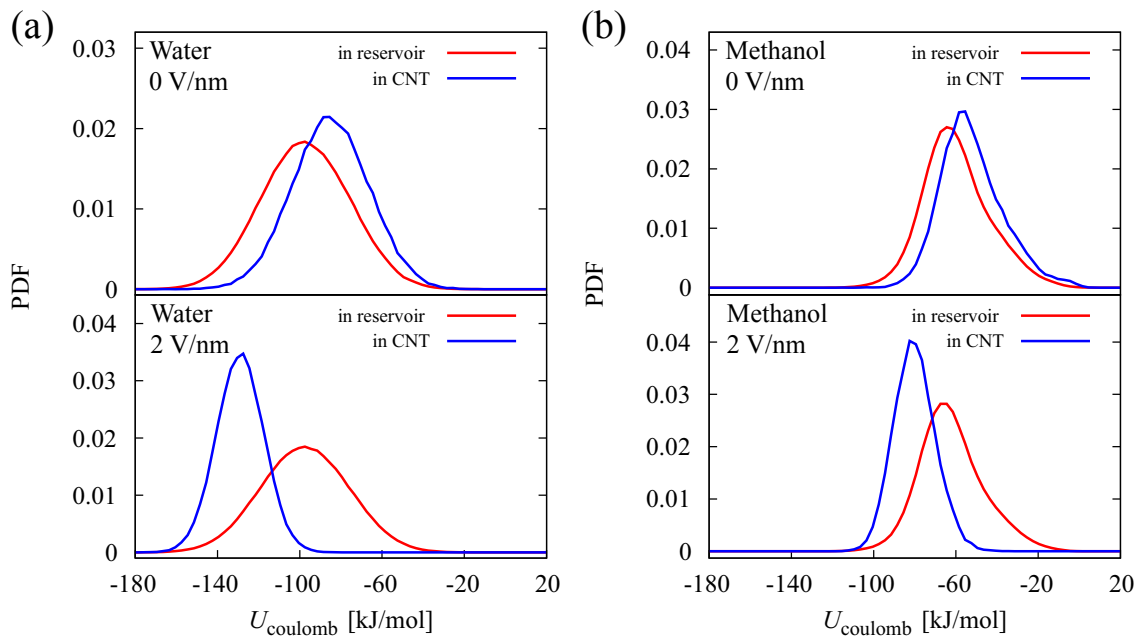
**Fig. 4.14** Distribution of the Coulomb potential energy for molecules in the reservoirs and in the (8,8) CNT with 0 and 2 V/nm; (a) for water molecules, and (b) for methanol molecules. With the electric field, the Coulomb potential energy in the CNT decreases significantly both for water and methanol. This means that under the electric field, the Coulomb potential energy facilitates the water and the methanol to fill the CNT.

- *Dipole potential energy*

When a dipole is subjected to an external electric field, it has the following potential energy,

$$U_{dipole} = -\boldsymbol{\mu} \cdot \boldsymbol{E} \tag{4.1}$$

where $\boldsymbol{\mu}$ is vector of dipole moment and $\boldsymbol{E}$ is the electric field. Thus, $U_{dipole}$ will be minimum when the direction of the dipole moment is parallel to that of the electric field. Figure 4.15(a) and (b) show distribution of $U_{dipole}$ in the reservoirs and in the (8,8) CNT with 2 V/nm for water and methanol molecules, respectively. The distribution of $U_{dipole}$ in the reservoirs is broader than in the CNT. This is because the direction of a dipole moment under the electric field is not statically parallel to the electric field but it oscillates. The amplitude of the oscillation for molecules in the reservoirs is larger than that of in the CNT. This is due to the effective electric field in the reservoirs is lower than that in the CNT. As we have discussed in chapter 3, the graphene sheet induces polarization. This signifies that the polarization induces internal electric field in the opposite direction to the external electric field. Thus, the effective electric field in the

reservoirs is the external electric field subtracted by the internal electric field. The distribution of dipole potential energy in the reservoirs for methanol decays faster than that for water (Fig. 4.15(b)). It indicates that the internal electric field due to the polarization for methanol is lower than that for water. The dipole moment of methanol is lower than that of water, which are 2.22 D and 2.27 D, respectively. This causes a lower charge density for methanol compared to that for water. As a result, the effect of polarization for methanol is weaker.

Since the peaks of $U_{dipole}$ distribution in the CNT are narrower than those in the reservoirs, the averages of dipole potential energy in the CNT are lower than those in the reservoirs. As a result, the differences of dipole potential energy in CNT and in the reservoirs ($\Delta U_{dipole}$) for water and methanol molecules are negative, which are −5.06 kJ/mol and −1.30 kJ/mol, respectively. This indicates that the dipole potential energy facilitates the water and methanol molecules to fill the CNT. $\Delta U_{dipole}$ with 0.5 and 1 V/nm are shown in Table 4.2 and 4.3.
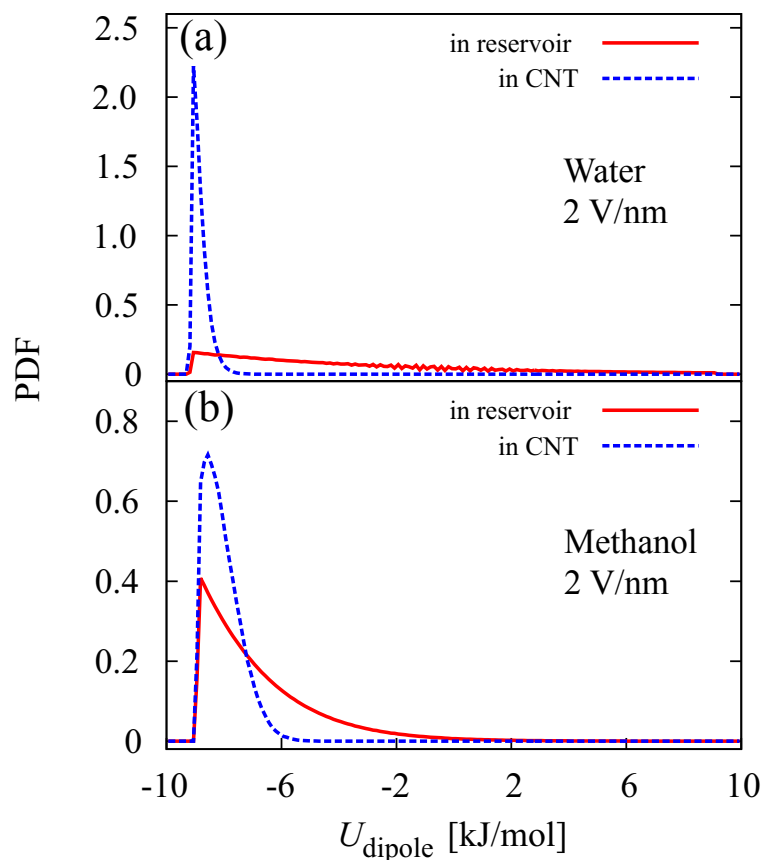


**Fig. 4.15** Distribution of the dipole potential energy for molecules in the reservoirs and in the (8,8) CNT with 2 V/nm; (a) for water molecules, and (b) for methanol molecules.

_____

$\Delta U_{total}$ per molecule in Table 4.2 and 4.3 decreases with the electric field. For water, the $\Delta U_{total}$ per molecule decreases from 1.76 kJ/mol to −11.60, −20.68, and −30.32 kJ/mol with 0, 0.5, 1, and 2 V/nm, respectively. For methanol, those values are −10.72 kJ/mol to −24.71, −29.58, and −32.14 kJ/mol with 0, 0.5, 1, and 2 V/nm, respectively. The decrease of the $\Delta U_{total}$ per molecule supports the notion that with the electric field, water and methanol molecules prefer to fill CNT. These results confirm the occupancy data where the number of molecules in CNTs increases with the electric field.

- *Comparison of the potential energy*

We calculated $\Delta U_{system}$ (see Table 4.4), which is defined as the $\Delta U_{total}$ per molecule in Table 4.2 and 4.3 multiplied by the number of all molecules occupied in (8,8) CNT. $\Delta U_{system}$ for water (CNT–water system) and methanol (CNT–methanol system) are shown in Fig. 4.16. At 0 V/nm, $\Delta U_{system}$ for methanol is lower than that for water, *i.e.* −179.02 kJ/mol and 63.18 kJ/mol, respectively. This suggests that without the electric field, methanol preferentially fill the CNTs over water, confirming the result of separation effect in Fig. 4.2 and 4.3. At 0 V/nm, $\Delta U_{LJ}$ is the main factor for facilitating methanol to fill CNT (Table 4.3). In other word, without the electric field, the van der Waals interaction of CNT–methanol is the key factor for the separation effect. This result confirms the previous study [144]. Figure 4.17(a) shows the distribution of LJ potential energy for methanol in (8,8) and (10,10) CNTs with 0 V/nm. The distribution in (10,10) CNT is shifted to the higher energy compared to that in (8,8) CNT. The average values are −29.10 kJ/mol and −24.45 kJ/mol in (8,8) and (10,10) CNTs, respectively. This indicates that the van der Waals interaction of CNT–methanol becomes weaker with the increase of CNT diameter. As a result, the separation effect without the electric field decreases significantly with the increase of the diameter (Fig. 4.2).

At 2 V/nm, $\Delta U_{system}$ for water is much lower than that for methanol, *i.e.* −1503.87 kJ/mol and −620.30 kJ/mol, respectively. This suggests water strongly prefers to fill CNTs over methanol. The Coulomb potential energy is the main factor for facilitating water to fill CNT under the electric field instead of the LJ potential (Table 4.2). Figure 4.17(b) shows that the electrostatic interaction within the water molecules is not weaker with the increase of CNT diameter. The average values for (8,8) and (10,10) CNTs are −129.01 kJ/mol and −132.66 kJ/mol, respectively. As a result, the separation effect with an electric field does not decrease as the CNT diameter increases.

The transition for the preference of water to fill CNT in Fig. 4.16 occurs at 0.5 V/nm.

However, in case of the reservoirs filled with water–methanol solutions, the potential energy of water and methanol can be slightly different from that in Table 4.2 and 4.3. This may shift the transition point to a lower electric field as indicated in Fig. 4.2 or 4.3.

**Table 4.4** Comparison of $\Delta U_{system}$ for water molecules (CNT–water system) and methanol molecules (CNT–methanol system) with (8,8) CNT. The $\Delta U_{system}$ is defined as the $\Delta U_{total}$ per molecule multiplied by the number of molecules occupied in the CNT.

| $E$ [V/nm] | Molecule | $\Delta U_{total}$ [kJ/mol] | Occupancy in CNT | $\Delta U_{system}$ [kJ/mol] |
|---|---|---|---|---|
| 0 | Water | 1.76 | 35.9 | 63.18 |
| | Methanol | −10.72 | 16.7 | −179.02 |
| 0.5 | Water | −11.60 | 40.6 | −470.96 |
| | Methanol | −24.71 | 19.6 | −484.32 |
| 1 | Water | −20.68 | 47.7 | −986.44 |
| | Methanol | −29.58 | 19.7 | −582.73 |
| 2 | Water | −30.32 | 49.6 | −1503.87 |
| | Methanol | −32.14 | 19.3 | −620.30 |
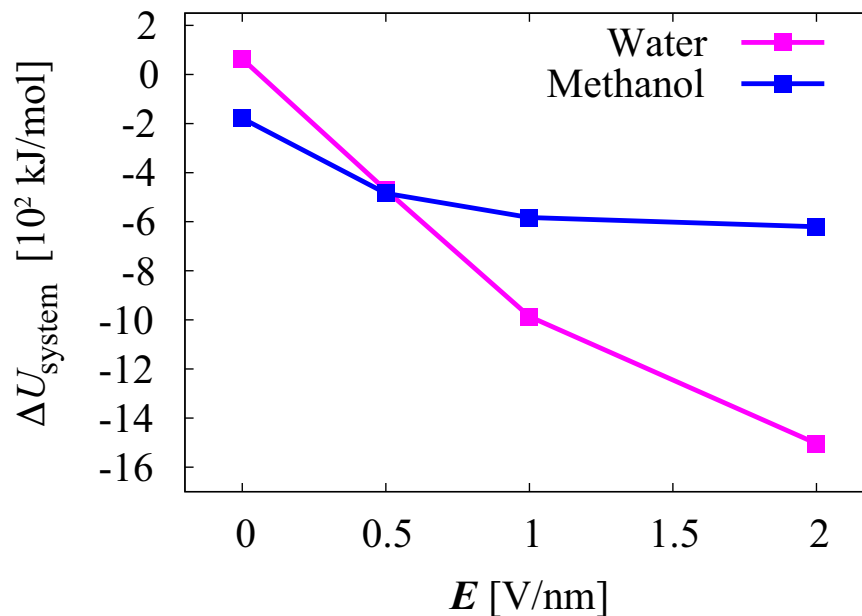


**Fig. 4.16** $\Delta U_{system}$ for water (CNT–water system) and methanol (CNT–methanol system) with (8,8) CNT. $\Delta U_{system}$ is defined as the $\Delta U_{total}$ per molecule multiplied by all molecules occupied in the CNT. At 0 V/nm, $\Delta U_{system}$ for methanol is lower than that for water suggesting the preference of methanol to fill CNT over water. With the electric field, $\Delta U_{system}$ for water tends to be lower than that for methanol. This suggests a reason that water prefers to fill CNT over methanol.
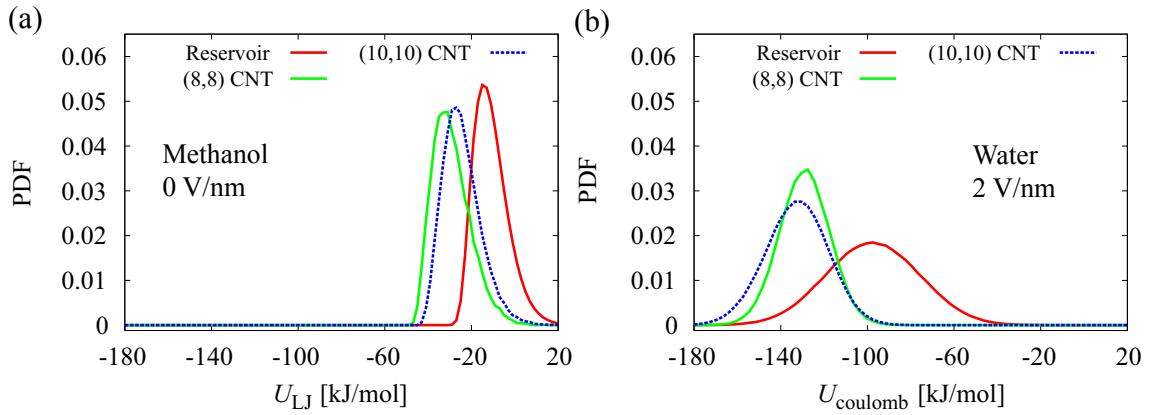
**Fig. 4.17** Effect of CNT diameter on the distribution potential energy: (a) The LJ potential energy of methanol molecules with 0 V/nm. The distribution in (10,10) CNT is shifted to higher energy compared to that in (8,8) CNT. This means the van der Waals interaction of CNT-methanol decreases with the increase of CNT diameter. (b) The Coulomb potential energy of water molecules with 2 V/nm. The electrostatic interaction of water molecules in (10,10) CNT is not weaker compared to that in (8,8) CNT.

d)  Structure and hydrogen bond network

Figure 4.18 shows structure of methanol molecules in (8,8) CNT with 2 V/nm. The molecules form two line-structures. The methyl groups from each line-structure are close to each other, implying that each line-structure is not connected by hydrogen bond to one another. Similar structure is shown for methanol molecules in (8,8) CNT with 1 V/nm. The structures of methanol molecules differ from those of water molecules, which are helical structures in the (8,8) CNT with 1 and 2 V/nm.

To analyze the hydrogen bond (HB), we employed the following geometrical criteria. For water molecules: $R_{OO} < 0.36$ nm, $R_{OH} < 0.24$ nm, and angle of HO---O < 30° [107] and for methanol molecules: $R_{OO} < 0.35$ nm, $R_{OH} < 0.26$ nm, and angle of HO---O < 30° [159]. The average numbers of HB per molecule for water in (8,8) CNT are 2.84, 2.93 and 2.77 with 0, 1 and 2 V/nm, respectively. Those values for methanol are 1.70, 1.89 and 1.83 with 0, 1 and 2 V/nm, respectively. Since the methyl groups cannot form HB, the number of HB of methanol is lower than that of water. The electric field does not significantly affect the number of HB per molecule both for water and methanol molecules. However, the electric field causes a very long lifetime of HBs in the water structure. The electric field strengthens the HBs in the water structure as shown in chapter 3. We determined the dynamics of HBs with the HB autocorrelation function as follows [108], which is same as Eq. (3.5) for water:

$$C_{HB}(t) = \frac{\langle h(0)h(t)\rangle}{\langle h^2\rangle} \tag{4.2}$$

where $h(t) = 1$ if a pair of molecules is bonded at time $t$ and $h(t) = 0$ otherwise. The denominator $\langle h^2\rangle$ is for normalization, which is the number of HBs tagged at $t = 0$. Same as to the water molecules, HB autocorrelation function for methanol with the electric field slightly decreases and then constant (Fig. 4.19). This indicates a very long lifetime of HBs. Similar to the water molecules, the electric field strengthens the HBs of the methanol structure in the CNT as well.

(a)                                (b)
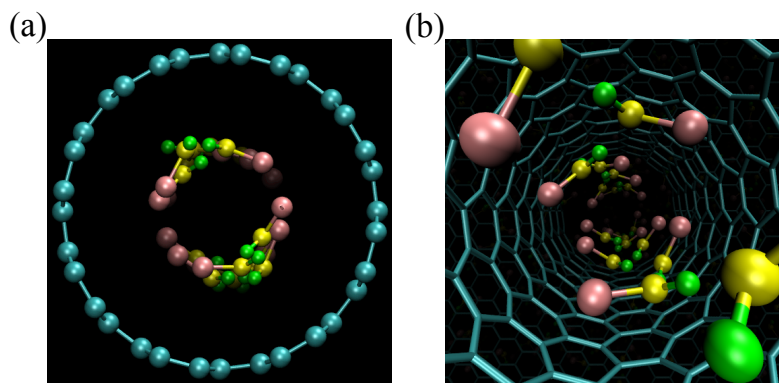


**Fig. 4.18**  Structure of methanol molecules in (8,8) CNT with 2 V/nm; (a) in orthographic projection and (b) perspective projection. The molecules form two line-structures where the methyl groups from each line-structure are close to each other. This indicates that the each line-structure is not connected by hydrogen bond to one another.
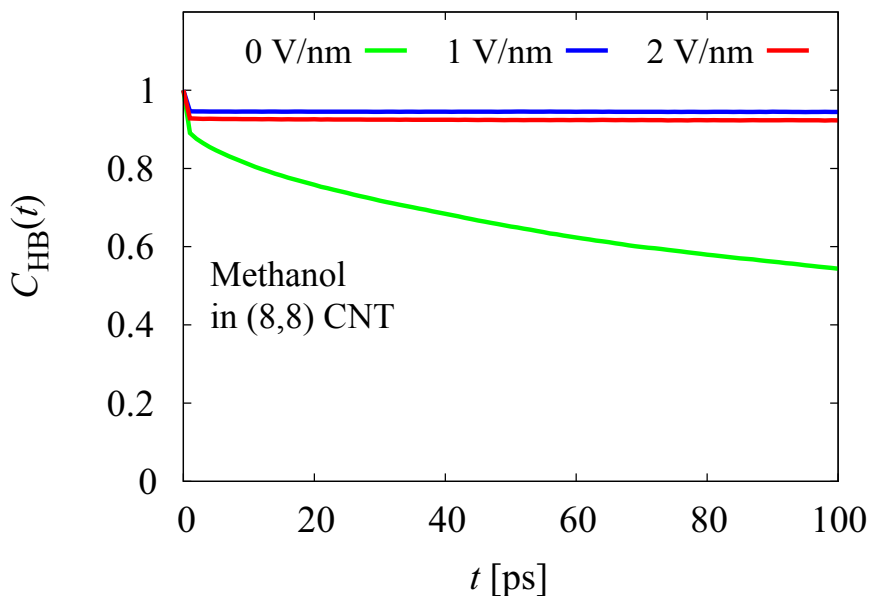


**Fig. 4.19**  HB autocorrelation function for methanol molecules in (8,8) CNT under 0, 1, and 2 V/nm. With the electric field, the lifetime of HBs of methanol molecules is very long.

_____

To characterize the HB network in the water and methanol structures, we calculated distribution of HB direction. The pairs of molecules bonded with HB are determined from the three-dimensional (3D) structures. Then, the structures are unrolled to obtained 2D structures as shown in Fig. 4.20(a) and (b) for water and methanol molecules in (8,8) CNT with 2 V/nm, respectively. The direction of HB in 2D structure is indicated with angle $\alpha$, which is measured from the $z$-axis to the clockwise direction. As an example, for the molecule $i$-th in Fig. 4.20(a), we identify all HBs from the $i$-th to all other molecules at $z \geq 0$. Position of the selected molecules $i$-th is set to $z = 0$ at the time, and $i$-th is applied the all molecules in the CNT. We analyze data from 22 ns of simulation time. The result is shown in Fig. 4.20(c) for water (red line) and methanol (dotted blue-line). There are two main-peaks at $\alpha_{w1} = 23°$, $\alpha_{w2} = 303°$, and a low peak at $\alpha_{w3} = 75°$ for HBs in the water molecules structure. The angle $\alpha_{w1}$ and $\alpha_{w2}$ are related to the column direction (magenta dashed-line) and the row direction (green dashed-line). This means the HB network is composed of a group of parallel lines in the column direction and a group of parallel lines in the row direction. In other word, the water molecules structure consists of line-structures that are connected by hydrogen bond to each other such as a net structure. In addition, few molecules create HB in the direction of $\alpha_{w3}$ (orange arrow-line). The 2D structure in Fig. 4.20(b) confirms the previous explanation that the methanol molecules have two line-structures. There are two peaks of HB direction, which are at $\alpha_{m1} = 25°$ and $\alpha_{m2} = 334°$ (Fig. 4.20(c)). The angle $\alpha_{m1}$ and $\alpha_{m2}$ are related to the directions of the magenta line and the green line in Fig. 4.20(b), respectively. There are two directions of HB within a line-structure as a result of the zig-zag configuration of methanol molecules. There is no hydrogen bond from one line-structure to the other line-structure. Hence, the two line-structures are independent. They are not connected by hydrogen bond to each other. Consequently, the methanol structure in the CNT is weaker than the water structure. With 2 V/nm, the Coulomb potential energy per molecule for water molecules is lower than that for methanol molecules, which are $-129.01$ kJ/mol and $-80.05$ kJ/mol, respectively (Table 4.2 and 4.3). Those data indicate that the electrostatic interaction in the water structure is stronger than that in the methanol structure. Moreover, the structure of water molecules is more compact because all atoms can contribute to create HB network. This causes the occupancy of water molecule in the CNT to be larger than that of methanol molecule (Table 4.4). In addition, the size of water molecule is smaller than that of methanol molecule.
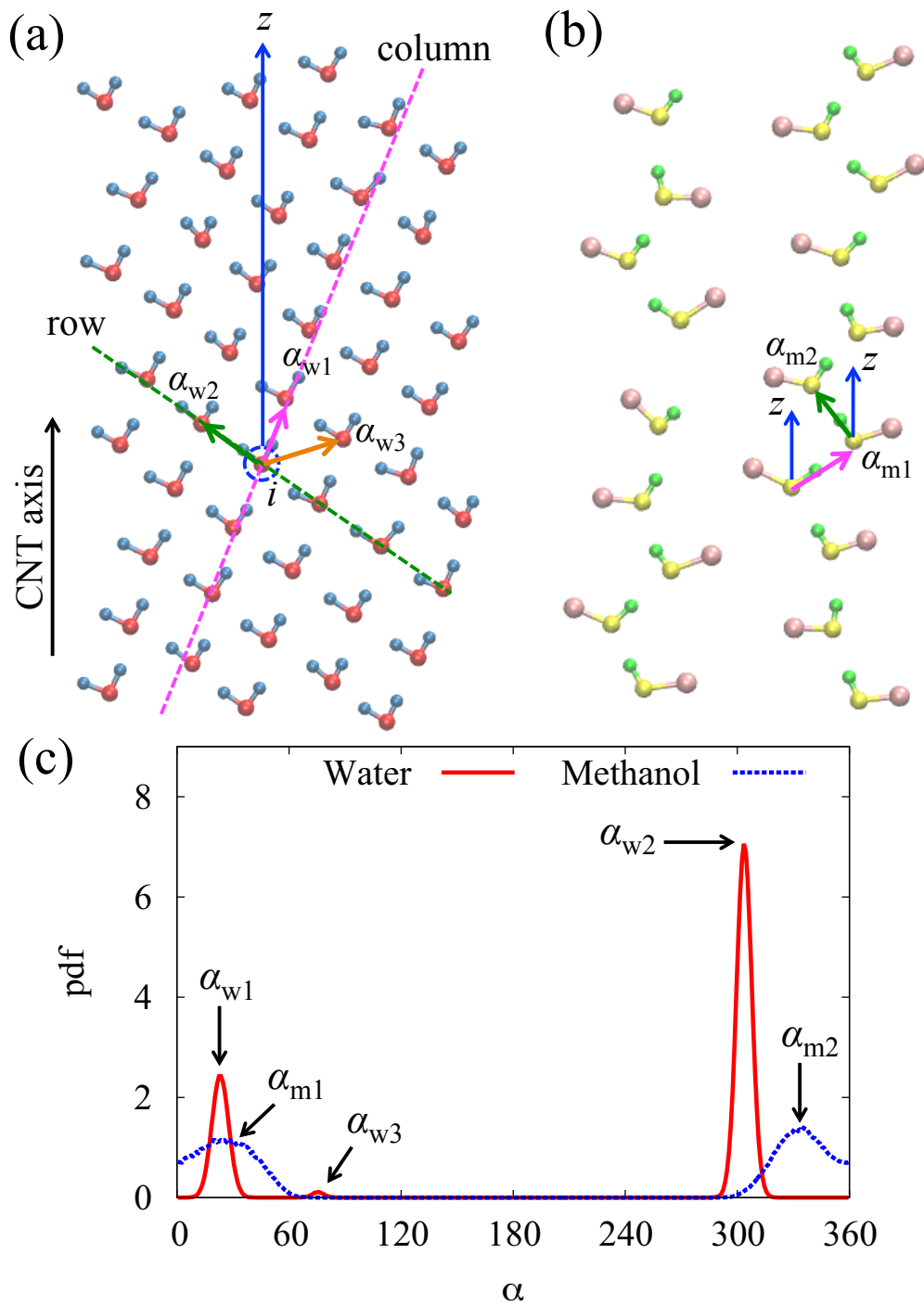
**Fig. 4.20** (a) Two-dimensional (2D) structure of water molecules in (8,8) CNT with 2 V/nm. (b) 2D structure of methanol molecules in (8,8) CNT with 2 V/nm. (c) Distribution of hydrogen bond direction in the water and the methanol structures. The direction is indicated with angle $\alpha$, which is measured from the $z$-axis to the clockwise direction.

## 4.4  Conclusions

MD simulations have been performed to a system consisting of a CNT, graphene sheets, and water–methanol reservoirs to investigate the effect of electric fields on the separation of water and methanol molecules. Without an electric field, methanol molecules fill the CNTs in preference to water molecules, resulting in a separation effect for methanol. However, the separation for methanol significantly decreases with the increase of CNT diameter. The van der Waals interaction of CNT–methanol is the main factor for the preference of methanol to fill CNT over water. However, the interaction decreases considerably with the increase of the diameter.

In contrast, under an electric field, water molecules occupy the CNTs in preference to methanol molecules. The preference for water molecules to flow through the CNTs over methanol molecules produces a separation effect for water. Interestingly, the separation effect for water is strong and does not significantly depend on the CNT diameter. The electric field induces the formation of ordered structures of water molecules in the CNTs. This results in the higher number of hydrogen bonds per molecule for the water molecule structures compared to that for the methanol molecule structures. Consequently, the water molecule structures are more stable and methanol molecules are removed from the CNTs. Moreover, methanol molecules from the reservoirs cannot disrupt the water molecule structures and permeate into the CNTs. Thus, with an electric field, the electrostatic interaction in the water structure is an important factor for the preference of water to fill CNTs. The electrostatic interaction does not decrease with the increase of CNT diameter. It depends more on the water molecules structure rather than the CNT diameter.

# Chapter 5

# SEPARATION OF WATER–ETHANOL WITH CARBON NANOTUBES AND ELECTRIC FIELDS

## 5.1  Introduction

In addition to its widely application in industrial processes, ethanol has been considered as a potential energy resource to reduce the use of fossil energy consumption, such as fuel for engines [162-165]. The use of ethanol as fuel of automobile engines has significantly increased the production of bioethanol [166-168]. The bioethanol is ethanol produced from various plants or biomass through fermentation processes [169-172]. To obtain a homogeneous ethanol–gasoline mixture, the water content in the ethanol is not desired, since nearly pure ethanol (≥ 99.5 vol%) or anhydrous ethanol is required [173-175]. However, the presence of water in the fermentation processes cannot be avoided. With a simple distillation, the purity of ethanol can be increased up to maximum 95 wt% due to the azeotropic point. Further anhydrous ethanol enrichment, can be achieved with azeotropic distillation or extractive distillation. Unfortunately, the distillation processes need a large amount of energy. Energy consumption is around 31% to 64% from the heating value of the anhydrous ethanol [174]. Therefore, developing more efficient methods is urgently required. Some alternative methods have been developed and applied, such as membrane pervaporation [132,176] and adsorption to zeolites [177-179]. Still, water–ethanol separation remains an important issue for the anhydrous ethanol production.

In this chapter, we demonstrate the separation of water–ethanol solution with CNTs and electric fields. Moreover, to clarify the separation effect, we investigate and compare the effects of axial electric fields on the ethanol and the water molecules confined in CNTs. Without an electric field, the van der Waals interaction of CNT–ethanol makes ethanol to preferentially occupy the CNTs over water, resulting in separation effect for ethanol. However, with the increase of CNT diameter, the separation effect for ethanol significantly decreases because of the decrease of the van der Waals interaction. In contrast, with an electric field, water prefers to fill CNTs over ethanol, *i.e.* separation

effect for water. The electrostatic interaction within water molecules structure is an important factor for the separation effect with the electric field. Interestingly, the electrostatic interaction depends on the water structure in CNT instead of CNT diameter. Consequently, the separation effect with an electric field is stronger and does not significantly decrease with the increase of the CNT diameter.

## 5.2 Simulation Method

Model system for the MD simulation is the same as to that in the chapter 3 and 4 (Fig. 3.1 and 4.1), which consisted of a 2.95 nm length of CNT embedded into two graphene sheets and reservoirs at the both sides. Similar to the separation for water–methanol mixtures in chapter 4, to demonstrate the separation effect for water–ethanol solution, we used a wide range of CNT diameter, *i.e.* 0.81 nm, 0.95 nm, 1.08 nm, 1.22 nm, 1.36 nm, 1.63 nm, 2.03 nm, 2.71 nm, 3.39 nm, and 4.07 nm for (6,6), (7,7), (8,8), (9,9), (10,10), (12,12), (15,15), (20,20), (25,25), and (30,30) CNTs, respectively. The reservoirs were filled with mixtures of water–ethanol molecules where the mole fractions of water ($\chi_{water}$) were 0.81 and 0.19. Those fractions were equivalent to 61.9% and 8.6% of mass fraction. All components were placed in a rectangular box that was subjected to periodic boundary conditions in all directions (*x*, *y*, and *z*-axes).

Model for water molecule was SPC [90] and ethanol molecule was OPLS united-atom [150,180]. It has been shown that the properties of ethanol can be well reproduced by the OPLS-UA model [181] and has been widely used for molecular dynamics studies [179,182,183]. With this model, an ethanol molecule was represented with four interaction sites, *i.e.* hydrogen atom (H), oxygen atom (O), methylene group (CH$_2$), and methyl group (CH$_3$). The Lennard-Jones (LJ) parameters and charges for each site are shown in Table 5.1. To obtain the interaction of different sites, the LJ parameters were calculated with the combination rule $\sigma_{ij} = (\sigma_i\sigma_j)^{1/2}$ and $\varepsilon_{ij} = (\varepsilon_i\varepsilon_j)^{1/2}$. An electric field up to 2 V/nm was applied in the direction of positive *z*-axis.

The simulations were performed using GROMACS 4.5.5 software [91]. The van der Waals interactions were cut off at 1.5 nm, and electrostatics interaction was treated using particle mesh Ewald (PME) method [92] with the real space cut off set to 1.5 nm as well. The length of chemical bonds of water and ethanol molecules and the angles between them were maintained at constant with SHAKE algorithm [93]. Torsional motion around C−O bond was the only the intramolecular dynamics considered in the simulation. The

CNT and graphene were made rigid by keeping the length and angle of the chemical bonds constant. The simulation was performed with $NL_xL_yP_zT$ where the temperature was set at 300 K with Nosé-Hoover coupling scheme [94,95]. The pressure in the axial direction ($z$-axis) was maintained at 0.1 MPa using the Parrinello-Rahman technique [96]. Time step was set at 2 fs and the simulations were performed for minimum 12 ns. In general, the systems reached an equilibrium state within 2 ns.

To clarify the separation effect, we investigated the effects of electric fields on ethanol molecules by performing additional simulations. We used (8,8) and (10,10) CNTs and the reservoirs were filled with only ethanol molecules.

**Table 5.1** The Lennard-Jones parameters and charges for water, ethanol, and carbon nanotubes.

| Site | $\sigma$ [nm] | $\varepsilon$ [kJ/mol] | $q$ [e] |
|---|---|---|---|
| Water, SPC model | | | |
| O | 0.3166 | 0.6500 | −0.820 |
| H | 0 | 0 | 0.410 |
| Ethanol, OPLS-UA model | | | |
| $CH_3$ | 0.3775 | 0.8661 | 0 |
| $CH_2$ | 0.3905 | 0.4937 | 0.265 |
| O | 0.3070 | 0.7113 | −0.700 |
| H | 0 | 0 | 0.435 |
| Carbon nanotubes | | | |
| C | 0.3400 | 0.3612 | 0 |

## 5.3  Results and Discussion

### 5.3.1  Separation effect and molecules structure

Same as to the separation for water–methanol mixtures in chapter 4, the separation effect was obtained by calculating the mole fractions in the CNTs and compared with those in the reservoirs, as shown in Fig. 5.1. At 0 V/nm, $\chi_{water}$ in the CNTs is lower (or $\chi_{ethanol}$ in the CNTs is higher) than that in the reservoirs for both $\chi_{water} = 0.81$ and 0.19 (black dotted-lines) in the reservoirs, as shown in Fig. 5.1(a) and (b), respectively. With no electric field, ethanol molecules preferentially fill in the CNTs over water molecules. The preference of ethanol to fill CNTs promotes the separation effect for ethanol. The

separation effect is strong for small CNTs diameters. However, the separation effect of water–ethanol solution without an electric field significantly decreases with the increase of CNT diameter. This result confirms the previous study [184].

In contrast, with the presence of an electric field, $\chi_{water}$ in the CNTs is higher than that in the reservoirs. With 1 and 2 V/nm, $\chi_{water}$ in the all CNTs is one. Only water occupies all the CNTs (Fig. 5.1(a)). With 0.5 V/nm, $\chi_{water}$ is one in all CNTs, except in (6,6) CNT. Even though $\chi_{water}$ in the reservoirs is very low, with 2 V/nm $\chi_{water}$ in (6,6) to (15,15) CNTs is one. The value decreases to 0.82, 0.95, and 0.77 in (20,20), (25,25), and (30,30) CNTs, respectively (Fig. 5.1(b)). Under the electric fields, water molecules prefer to fill CNTs over ethanol molecules, resulting in a separation effect for water. Interestingly, the separation effect with the electric field is stronger and does not significantly decrease with the increase of the CNT diameter.
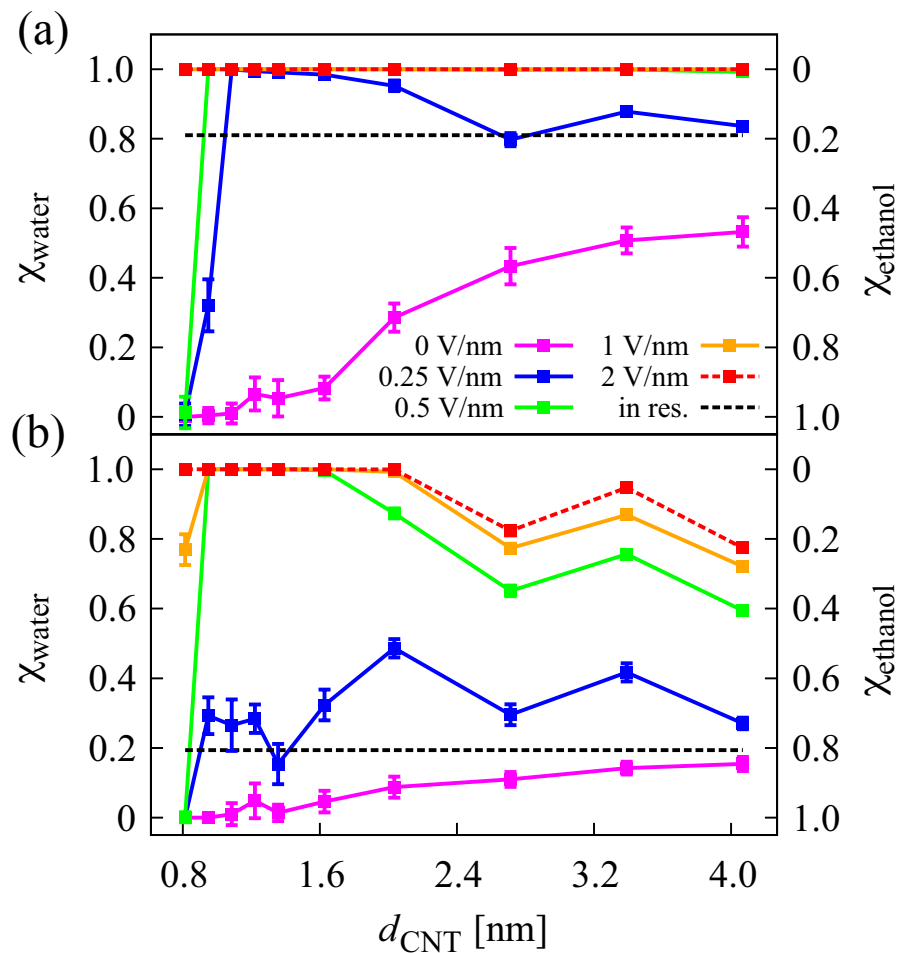


**Fig. 5.1** Mole fraction of water molecules $\chi_{water}$ (or ethanol molecules $\chi_{ethanol}$) in (6,6) to (30,30) CNTs with various electric fields. The black dotted-lines show the mole fraction in the reservoirs, *i.e.* (a) $\chi_{water}$ = 0.81, and (b) $\chi_{water}$ = 0.19. The error bars represent the standard deviation.

The dependency of the mole fractions in the CNTs on the electric field strength is displayed in Fig. 5.2. The $\chi_{water}$ in the CNTs increases with the increase of the electric field $E$. It is obviously noticed that the effect of $E \leq 0.5$ V/nm on the separation effect with (6,6) CNT is weaker than that with larger CNTs. As explained in the following paragraph, the structure of water molecules in the CNTs plays an important role for the separation effect with the electric field. As mentioned in the chapter 4, water molecules in (6,6) CNT have single file structure [4,160,161]. It will change to zig-zag structure under $E \geq 0.5$ V/nm, *i.e.* more stable structure.
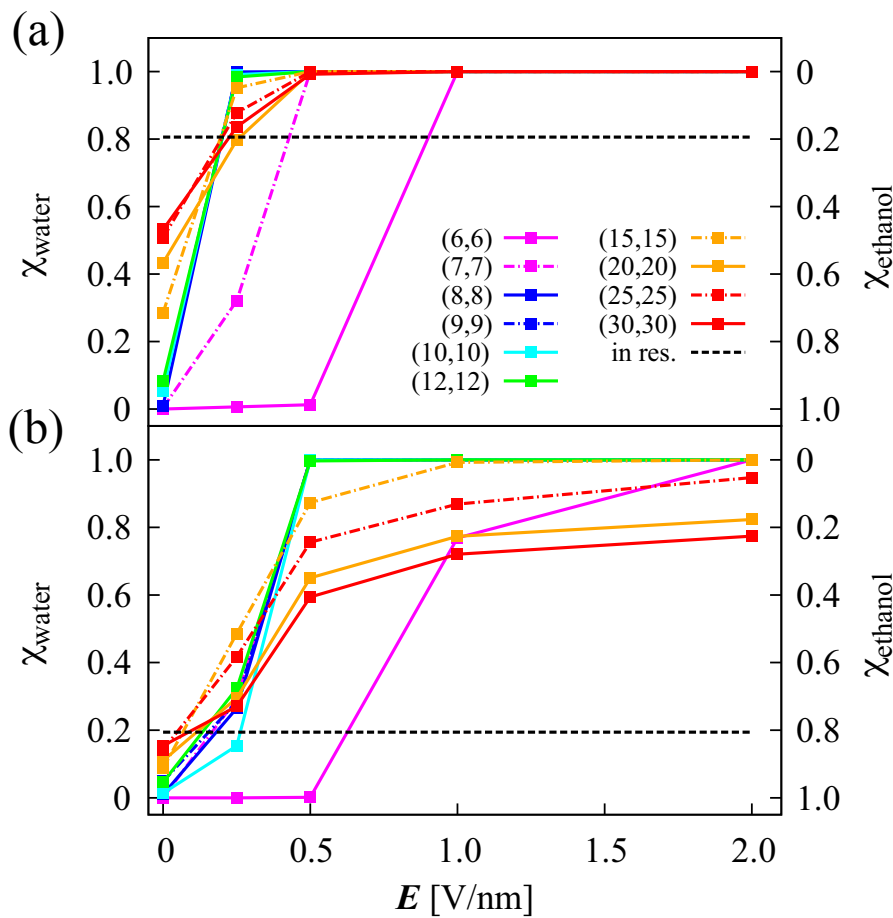


**Fig. 5.2** The dependency of $\chi_{water}$ (or $\chi_{ethanol}$) on the electric field $E$ in (6,6) to (30,30) CNTs. The mole fraction in the reservoirs are: (a) $\chi_{water}$ = 0.81 (black dotted-line), and (b) $\chi_{water}$ = 0.19 (black dotted-line).

Figure 5.3 shows snapshots of the molecules structures in (8,8) CNT for $\chi_{water}$ = 0.19 in the reservoirs. With 0 V/nm, only ethanol molecules appear in the snapshot. Water molecules in (8,8) CNT are very few for this condition (Fig. 5.1). With 0.25 V/nm, the number of water molecules in the CNT increases as seen in the snapshot. With $E \geq 0.5$ V/nm, only water molecules fill in the CNT and they form ordered (helical) structures. Those are the ice nanotube structures induced by the electric field as shown in the chapter 3. The formation of the ordered structure makes water in the CNTs to be more stable than ethanol. As a result, CNTs prefer to adsorb water instead of ethanol. Under the electric field, water structure in CNTs becomes more stable due to the electrostatic interaction within the structure as shown in the next subsection. The results in Fig. 5.1 to 5.3 are similar to the separation for water–methanol mixtures in the chapter 4.
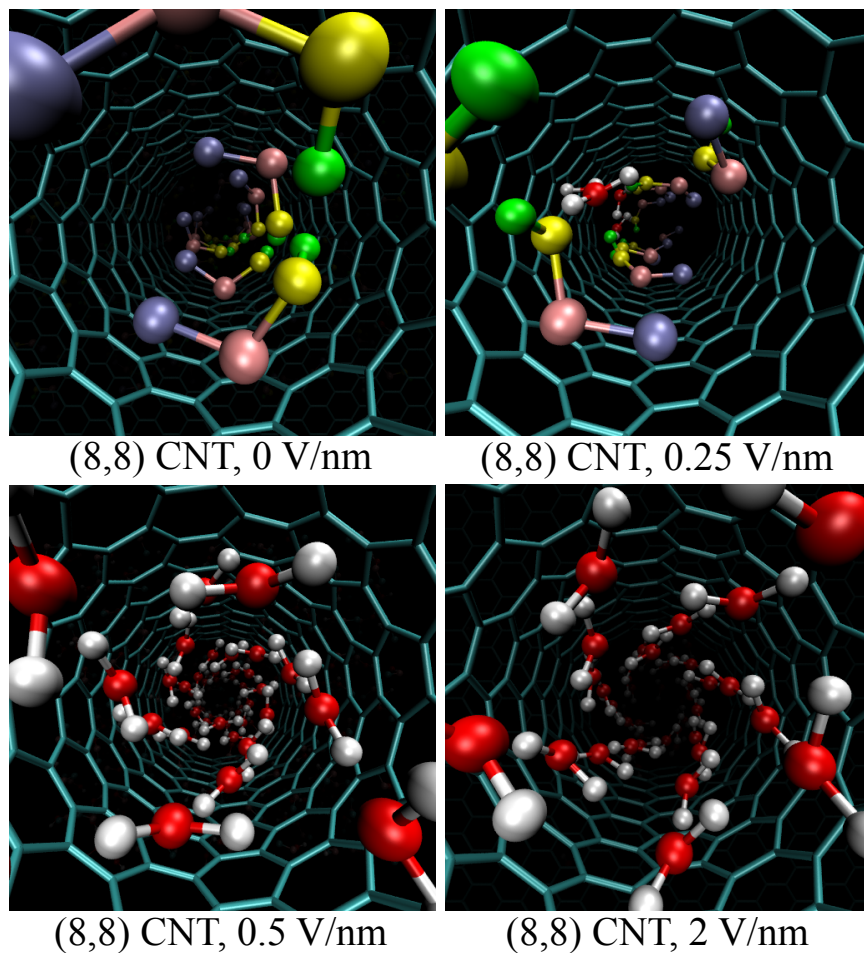


**Fig. 5.3** Structures of molecules in (8,8) CNT with $E$ = 0, 0.25, 0.5, and 2 V/nm for $\chi_{water}$ = 0.19 in the reservoirs. Green, yellow, pink, and blue are for hydrogen, oxygen, methylene, and methyl of ethanol molecules, respectively. Red and white are for oxygen and hydrogen of water molecules, respectively. With $E \geq 0.5$ V/nm, only water molecules occupy in the CNT and they form helical structures.

### 5.3.2 Comparison of electric field effects on water and ethanol molecules in CNTs

The effects of an electric field on ethanol were investigated by filling the reservoirs with ethanol molecules only. We observed the orientation of molecules, occupancy of molecules in CNTs, structures of molecules, and potential energies. The results were then compared with those for water in chapter 3.

a)  Orientation of molecules

The direct effect of an electric field on ethanol molecules is a change of dipole moment orientation. It is due to the forces induced by the electric field on the positive charges of hydrogen (H) and methylene ($CH_2$) and on the negative charge of oxygen (O). The forces produce moment aligning the direction of dipole moment parallel to that of the electric field. Figure 5.4 shows direction of dipole moment of ethanol molecules in (8,8) and (10,10) CNTs with 0, 1, and 2 V/nm. The direction of dipole moment is indicated with an angle $\alpha$, which is an angle between the dipole vector $\boldsymbol{\mu}$ and the electric field $\boldsymbol{E}$. With 0 V/nm, the dipole moment of ethanol in (8,8) CNT has a particular orientation at $\cos \alpha = -0.9$. It differs from the dipole moment of water molecules, where water in (8,8) CNT has two orientations at $\cos \alpha = -0.8$ and $0.8$ (in chapter 3). They are opposite to each other. It seems that the molecular size causes the dipole moment orientation of ethanol differs from that of water. In the larger (10,10) CNT with 0 V/nm, the dipole moment orients in all direction with two small-peaks at $\cos \alpha = -0.9$ and $0.9$. This is similar to that of the water molecules. With 1 and 2 V/nm, the direction of dipole moment of ethanol in (8,8) and (10,10) CNTs is parallel to the electric field $\boldsymbol{E}$. This is same as the direction of dipole moment of the water molecules under the electric fields.
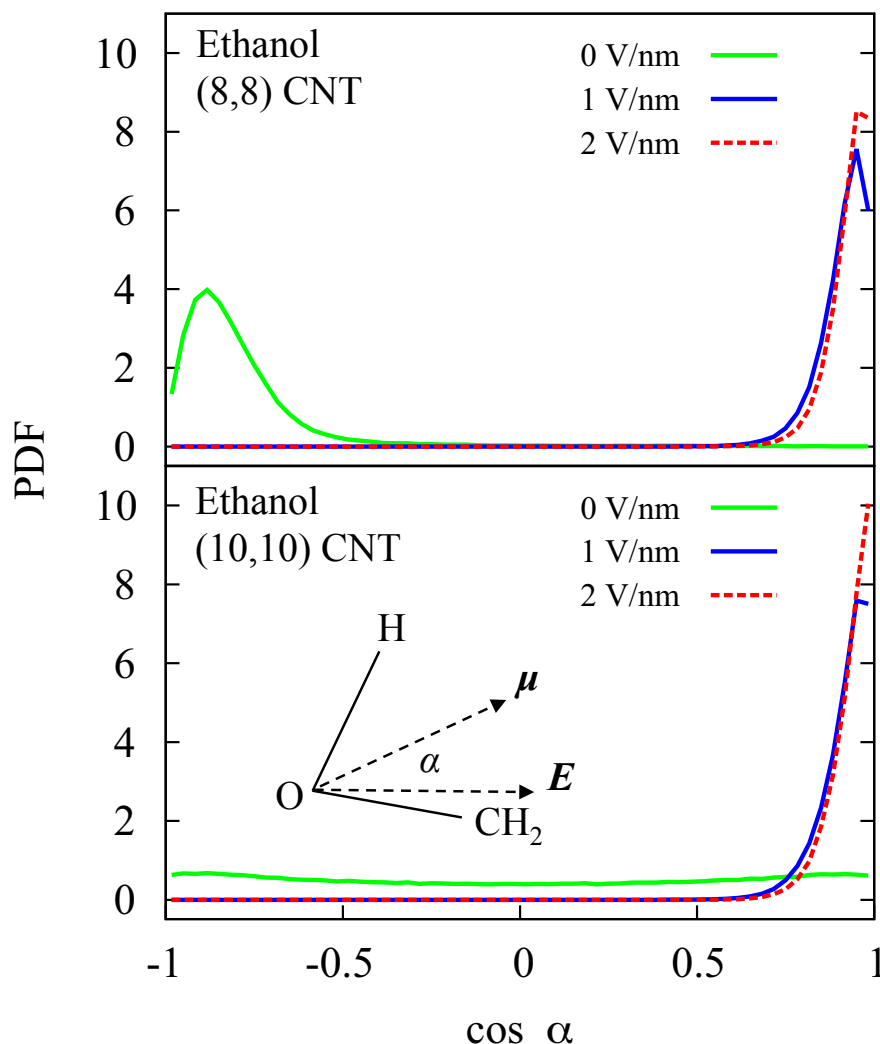
**Fig. 5.4** Orientation of dipole moment of ethanol molecules in (8,8) and (10,10) CNTs. Direction of the dipole moment is indicated with an angle $\alpha$, which is the angle between the dipole moment $\mu$ and the electric field $E$. O, H, and $CH_2$ represent oxygen, hydrogen, and methylene of ethanol, respectively. The vertical axis shows probability distribution function (PDF).

Distribution of the dihedral angle associated with torsional motion around $O - C$ bond is presented in Fig. 5.5. Ethanol in the reservoirs has a central peak at $\alpha = 180°$ and two mirror-image peaks at $\alpha = 72°$ and $288°$ (black curve). The central peak corresponds to trans conformers, and the other two-peaks correspond to gauche conformers. The fraction of each conformer was obtained by integrating the distribution curves from 0° to 120° and from 240° to 360° for the gauche conformers, and from 120° to 240° for the trans conformers. In the reservoirs with 0 V/nm, the population of the trans conformers is 50%. It is in very good agreement with bulk ethanol at 298 K [150,181]. The population of the trans conformers in the reservoirs slightly increases to 51% and 52% with 1 and 2

V/nm, respectively.

In (8,8) CNT, ethanol tends to form the gauche conformers, which is different from the dihedral angle distribution in the reservoirs. The fractions of the gauche conformers are 82%, 85%, and 81% with 0, 1, and 2 V/nm, respectively. The snapshot in the Fig. 5.5 (top) shows the orthographic projection of the ethanol molecules structure in (8,8) CNT with 2 V/nm. The ethanol molecules form a semicircle structure with the hydrogen bond of the hydrogen (green) and the oxygen (yellow) atoms in the middle. The ethanol molecules form the gauche conformers follow the contour of CNT wall. The ethanol molecules in (8,8) CNT with 0 and 1 V/nm have similar structures. In more detail, the ethanol molecules structures in CNTs are shown in Fig. 5.6 as will be described in the following paragraph. In the larger diameter of (10,10) CNT with 0 V/nm, the distribution of dihedral angle becomes similar with that in the reservoirs, *i.e.* 49% is the trans conformers. As shown by the snapshot in Fig. 5.5 (bottom), a disordered ethanol molecules structure is observed at 0 V/nm. With 1 or 2 V/nm, ethanol forms two structures in (10,10) CNT where each structure is similar to that in the (8,8) CNT. However, the ethanol molecules tend to form the trans conformers instead of the gauche conformers such as in the (8,8) CNT. With 1 and 2 V/nm, the trans conformers in (10,10) CNT is 67%. The CNT diameter could be an important factor to affect the dihedral angle.
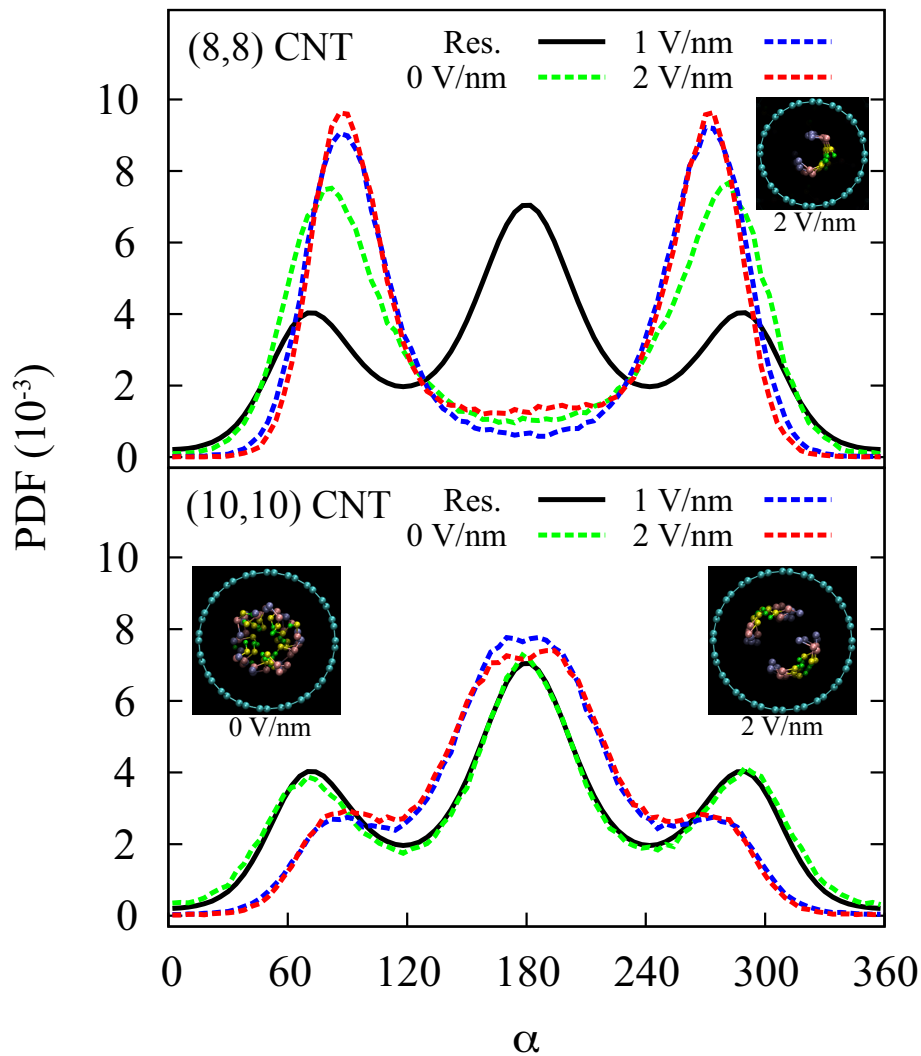
**Fig. 5.5** Distribution of the dihedral angle of ethanol molecules in (8,8) CNT (top) and (10,10) CNT (bottom) with 0, 1, and 2 V/nm. The black curve (Res.) shows the distribution of ethanol in the reservoirs with 0 V/nm. The orthographic projection of the snapshots in the figure show structure of ethanol in (8,8) CNT with 2 V/nm (top) and in (10,10) CNT with 0 and 2 V/nm (bottom).

b)  Occupancy of molecules in CNTs

The effect of electric fields on the average number of ethanol molecules occupied in (8,8) and (10,10) CNTs is shown in Tabel 5.2. The tendency of occupancy increase of ethanol in CNTs in the presence of electric field is observed. Same as to the water molecules, an electric field facilitates ethanol molecules to fill CNTs. However, the effect of an electric field on the occupancy of water in CNTs is stronger. The numbers of water molecules in CNTs increases more significantly with the electric fields (Table 3.2 in chapter 3).

**Table 5.2** The average numbers of ethanol molecules in CNTs, with standard deviation.

| $E$ [V/nm] | (8,8) CNT | (10,10) CNT |
|---|---|---|
| 0 | 12.0 ± 0.6 | 22.4 ± 1.0 |
| 1 | 12.8 ± 0.5 | 23.9 ± 0.8 |
| 2 | 12.8 ± 0.6 | 23.6 ± 0.8 |

c) Structures and hydrogen bond network

Structures of ethanol molecules in CNTs are shown in Fig. 5.6(a) and (b) for perspective projection and two-dimensional (2D) structures, respectively. Radial positions of oxygen atoms in the CNTs were averaged to determine radius of a tube. Then, all atoms of ethanol molecules were radially projected on the tube wall. Finally, the tube wall was opened to obtain the 2D structures. In (8,8) CNT with 2 V/nm, ethanol forms single line structure as seen in Fig. 5.6(a) (left) and (b) (left). In (10,10) CNT with 2 V/nm, ethanol has two parallel structures as seen in Fig. 6(a) (right) and (b) (right).

To analyze hydrogen bond (HB), we employed the geometrical criteria. A pair of ethanol molecules were considered to have HB if they fulfill the following three conditions: $R_{OO}$ < 0.35 nm, $R_{OH}$ < 0.26 nm, and angle of HO···O < 30° [181]. $R_{OO}$ and $R_{OH}$ denote the distances of oxygen–oxygen and oxygen–hydrogen, respectively. Average numbers of HB per molecule in (8,8) CNT are 1.90, 1.85, and 1.79 with 0, 1, and 2 V/nm, respectively. While the numbers in (10,10) CNT are 1.85, 1.91, and 1.87 with 0, 1, and 2 V/nm, respectively. The electric field does not significantly increase the number of HB. However, HBs under the electric field are stronger than those without the electric field. As shown in the following paragraph, the Coulomb potential energy per molecule with an electric field is lower than that without an electric field. This indicates the electric field strengthens the electrostatic interaction within the ethanol molecules structure.

Ethanol forms HB network with oxygen and hydrogen atoms only. While, methyl and methylene groups cannot contribute to build the HB network. As seen in (10,10) CNT (Fig. 6(b) right), methyl groups from each structure are close to each other. This makes the two parallel structures are not bonded by HB to one another. Bulk ethanol shows similar HB structure, which is linear chain structures [181]. Water molecules can form HB network with all of their atoms. The number of HB per molecules for water is

higher than that for ethanol, *i.e.* 2.84, 2.93, and 2.77 in (8,8) CNT with 0, 1, and 2 V/nm, respectively (as seen in chapter 4). Moreover, water in CNTs form parallel structures that are bonded by HB to each other. This facilitates a stronger electrostatic interaction within the water structure compared to that within the ethanol structure. In other words, water structure in CNTs under the influence of an electric field is more stable than those of ethanol.
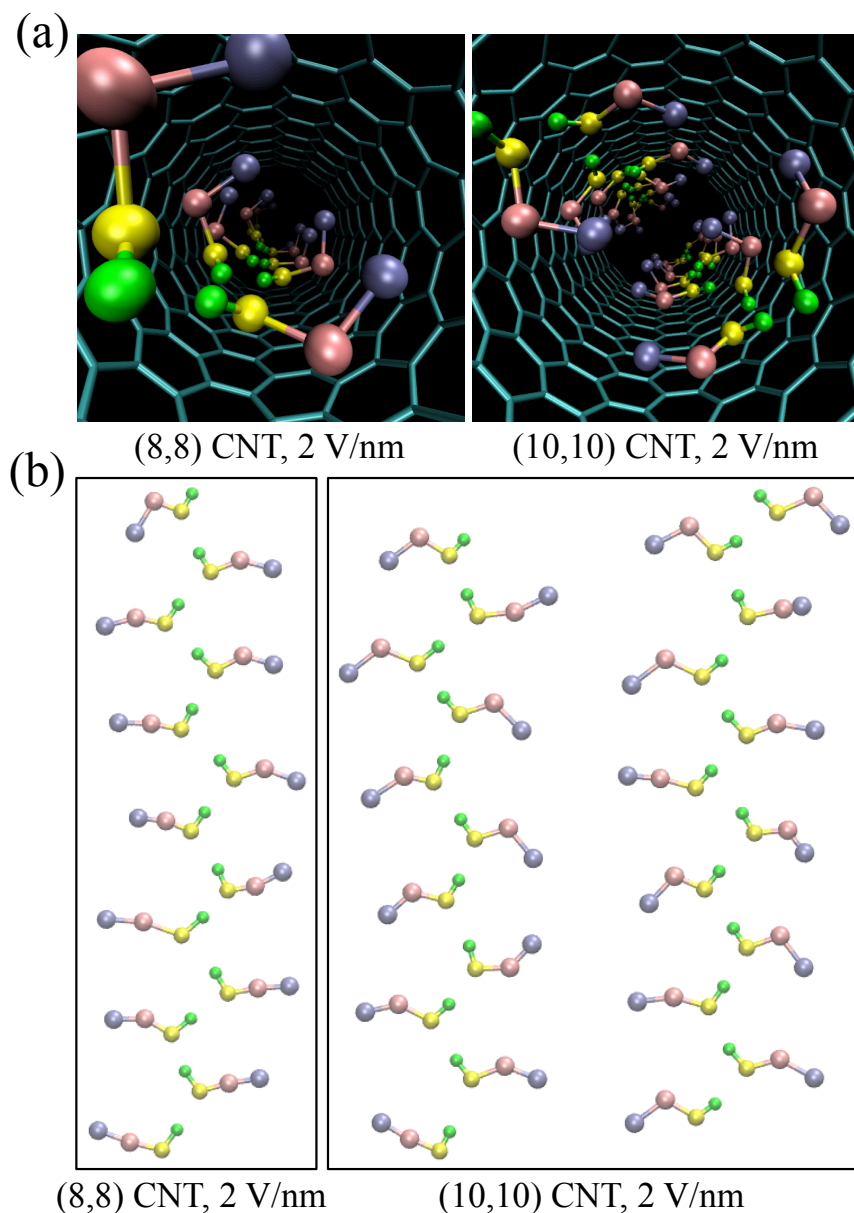


**Fig. 5.6** Snapshots of ethanol molecules in CNTs. (a) Perspective projection in (8,8) CNT with 2 V/nm (left) and in (10,10) CNT with 2 V/nm (right). (b) Two-dimensional structures with 2 V/nm in (8,8) CNT (left) and in (10,10) CNT (right). Green, yellow, pink, and blue represent hydrogen, oxygen, methylene, and methyl, respectively.
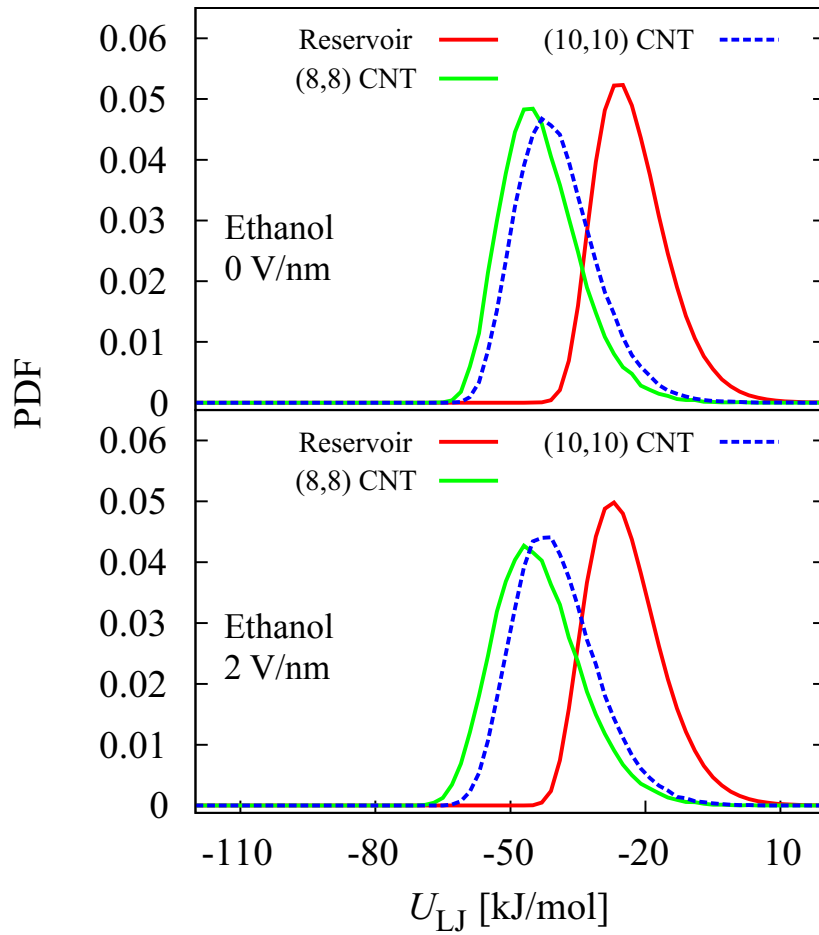
d) Potential energies

- *Lennard-Jones potential energy*

To investigate the interaction between CNT and ethanol molecules, we calculated the Lennard-Jones (LJ) potential energy of ethanol in the reservoirs and in CNTs. Distributions of the LJ potential energy with 0 and 2 V/nm are shown in Fig. 5.7. The difference of the LJ potential energy in CNT and in the reservoirs, $\Delta U_{LJ} = U_{LJ, CNT} - U_{LJ, res.}$, indicates the van der Waals interaction between CNT and ethanol molecules. With 0 V/nm, average of the LJ potential in the reservoirs and in (8,8) CNT are –22.79 kJ/mol and –43.03 kJ/mol, respectively (Table 5.3). This means the $\Delta U_{LJ}$ is –20.24 kJ/mol. The negative value of $\Delta U_{LJ}$ indicates the attractive interaction of CNT–ethanol. With 2 V/nm, the $\Delta U_{LJ}$ slightly increases to –19.34 kJ/mol. The electric field does not significantly change the van der Waals interaction of CNT–ethanol.

The $\Delta U_{LJ}$ for water in (8,8) CNT with 0 V/nm is –10.37 kJ/mol (in chapter 4), which is higher than that of ethanol. This suggests the interaction of CNT–ethanol is stronger than that of CNT–water. Moreover, it also implies that the van der Waals interaction of CNT–ethanol facilitates ethanol to fill CNTs in preference to water (Fig. 5.1). With 2 V/nm, $\Delta U_{LJ}$ for water becomes positive 6.29 kJ/mol, which indicates repulsive interaction of CNT–water. Thus, with the electric fields, the van der Waals interaction of CNT–water does not contribute in the water preference to fill CNTs (Fig. 5.1). The repulsive interaction confirms the result that the ice nanotube induced with an electric field can flow through CNT (in chapter 3).

The $\Delta U_{LJ}$ for (10,10) CNT is shown in the 6-th column of Table 5.3, *i.e.* –16.69 and –15.48 kJ/mol with 0 and 2 V/nm, respectively. $\Delta U_{LJ}$ in (10,10) CNT is larger than that in (8,8) CNT. This implies the attractive interaction of CNT–ethanol decreases as the CNT diameter increases. Figure 5.7 confirms this result where the distribution of $U_{LJ}$ is shifted to the higher energy from (8,8) to (10,10) CNTs.

**Fig. 5.7** Distribution of the Lennard-Jones (LJ) potential energy of ethanol molecules in reservoirs and in CNTs with 0 and 2 V/nm. The LJ potential energy in the CNTs is lower than that in the reservoirs denoting attraction of the van der Waals interaction between CNT and ethanol. The attractive interaction decreases as the CNT diameter increases, as shown by the (10, 10) CNT.

**Table 5.3** The average of the potential energies per molecule for ethanol in reservoirs (Res.) and in (8,8) CNT. $\Delta U$ is the difference between the potential energies in CNT ($U_{CNT}$) and in the reservoirs ($U_{res}$), $\Delta U = U_{CNT} - U_{res}$. The 6-th column shows $\Delta U$ for (10,10) CNT.

| $E$ [V/nm] | Energy $(U)$ | in Res. [kJ/mol] | in CNT [kJ/mol] | $\Delta U$ [kJ/mol] | $\Delta U_{10,10}$ [kJ/mol] |
|---|---|---|---|---|---|
| | LJ | −22.79 | −43.03 | −20.24 | −16.69 |
| 0 | Coulomb | −58.89 | −60.80 | −1.91 | 2.18 |
| | | | Total: | −22.15 | −14.51 |
| | LJ | −24.25 | −43.59 | −19.34 | −15.48 |
| | Coulomb | −61.68 | −73.21 | −11.53 | −12.10 |
| 2 | Dipole | −7.07 | −8.29 | −1.22 | −1.24 |
| | | | Total: | −32.09 | −28.82 |

_____

- *Coulomb potential energy*

Figure 5.8 shows distribution of the Coulomb potential energy of ethanol in the reservoirs and in CNTs. With 0 V/nm, there is no significant difference of the potential energy in the reservoirs and in the CNTs. The averages of the Coulomb potential energy are −58.89 kJ/mol and −60.80 kJ/mol in the reservoirs and in (8,8) CNT, respectively (Table 5.3). With 2 V/nm, the Coulomb potential energy decreases from −61.68 kJ/mol in the reservoirs to −73.21 kJ/mol in (8,8) CNT. The electric field creates a stronger electrostatic interaction within ethanol molecules structure in the CNTs compared to that in the reservoirs. The $\Delta U_{coulomb}$ decreases from −1.91 kJ/mol to −11.53 kJ/mol with 0 and 2 V/nm, respectively. This implies the Coulomb potential energy facilitates the ethanol molecules to fill CNT in the presence of an electric field. The $\Delta U_{coulomb}$ does not increase as the CNT diameter increases, *i.e.* −12.10 kJ/mol in (10,10) CNT with 2 V/nm. Unlike the van der Waals interaction with the CNT wall, the electrostatic interaction of molecules structure in CNT under the electric field does not decrease with the increase of CNT diameter. Figure 5.8 confirms this result in which the distribution of $U_{coulomb}$ for (10,10) CNT is not shifted to the higher energy compared to that for (8,8) CNT.

The $\Delta U_{coulomb}$ for water with 0 and 2 V/nm are 12.13 and −31.55 kJ/mol, respectively (in chapter 4). Without electric field, the Coulomb potential energy does not contribute as a driving energy for water to fill CNT. Contrarily, with an electric field, the Coulomb potential energy plays the role as the main factor to facilitate water to fill CNT. In the larger (10,10) CNT with 2 V/nm, $\Delta U_{coulomb}$ decreases to −35.1 kJ/mol. This supports the notion that the electrostatic interaction of molecules in CNTs under electric fields does not decrease with the increase of the diameter. Coulomb potential energy per molecule for water in (8,8) CNT with 2 V/nm is −129.01 kJ/mol, which is much lower than that for ethanol. This clarifies that the electrostatic interaction of water structure is stronger than that of ethanol structure.
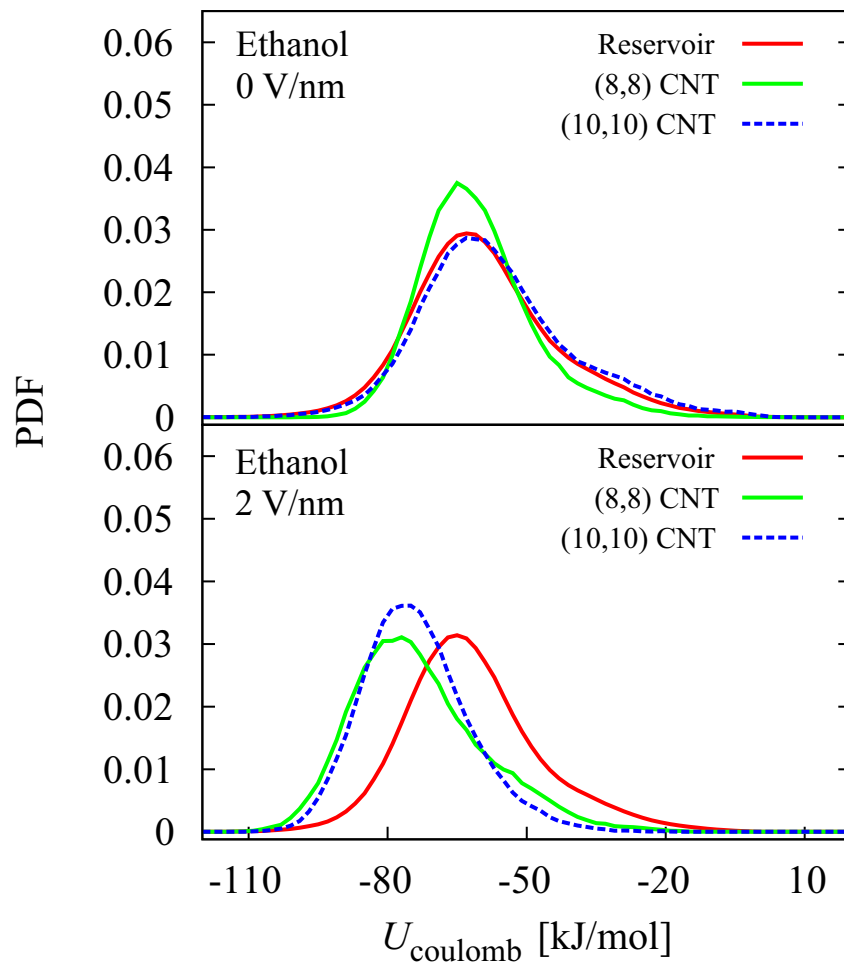
**Fig. 5.8** Distribution of Coulomb potential energy of ethanol molecules in the reservoirs and in CNTs with 0 and 2 V/nm. With an electric field, the potential energy in CNTs is lower than that in the reservoirs. The electric field strengthens the electrostatic interaction within the ethanol molecules structure in CNTs.

• *Dipole potential energy*

The dipole potential energy, due to an external electric field is determined with Eq. (4.1), which is $U_{dipole} = -\boldsymbol{\mu} \cdot \boldsymbol{E}$ . As explained in subsection 4.3.3 (chapter 4), the potential energy will be minimum if direction of the dipole moment is parallel to that of the electric field. However, under an electric field, the direction of dipole moment is not static parallel to the electric field but oscillates around it. The amplitude of the dipole oscillation in the reservoir is larger than that in the CNT because of the graphene-induced polarization in the reservoirs (subsection 3.3.2). Consequently, distribution of the dipole potential in reservoirs is broader (see Fig. 5.9) and the average of the dipole potential in the reservoirs is slightly higher than that in CNT (Table 5.3). $\Delta U_{dipole}$ for

_____

(8,8) and (10,10) CNTs are −1.22 kJ/mol and −1.24 kJ/mol, respectively. Diameter of CNT does not significantly change the $\Delta U_{\text{dipole}}$. The $\Delta U_{\text{dipole}}$ for water is slightly lower, which is −5.06 kJ/mol. This is because the dipole moment of water is larger than that of ethanol, *i.e.* 2.27 D and 2.22 D, respectively. Thus, the effect of the polarization for water is stronger and the effective electric field in the reservoirs becomes lower. As a result, the amplitude of rotational motion for water molecules in reservoirs is larger, hence the broader distribution of the dipole potential.

Total of $\Delta U$ per molecule ($\Delta U_{\text{total}}$) decreases with an electric field, from −22.15 to −32.09 kJ/mol in (8,8) CNT and from −14.51 to −28.82 kJ/mol in (10,10) CNT with 0 and 2 V/nm, respectively. A decrease in the $\Delta U_{\text{total}}$ denotes that the electric field makes ethanol molecules prefer to fill CNTs. This agrees with the occupancy data where the electric field increases the number of ethanol molecules in CNTs (Table 5.2).
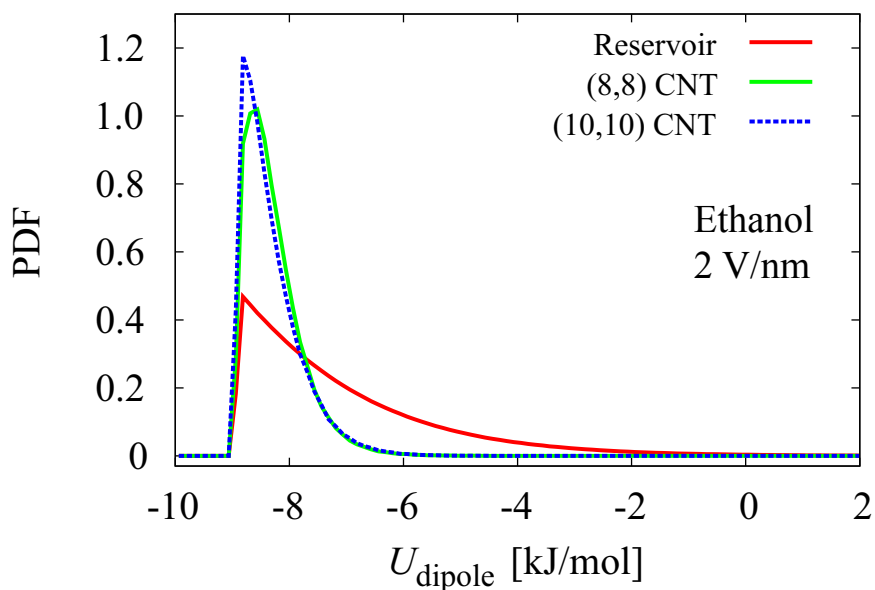


**Fig. 5.9** Distribution of the dipole potential energy for ethanol molecules in the reservoirs and in CNTs with 2 V/nm.

_____

- *Comparison of potential energy*

Same as in the chapter 4, we calculated and compared the $\Delta U_{\text{system}}$ for (8,8) CNT to clarify the separation effect. $\Delta U_{\text{system}}$ is defined as the $\Delta U_{\text{total}}$ per molecule in the Table 5.3 multiplied by the number of all molecules in the CNT (Table 5.2). The results are compared with the $\Delta U_{\text{system}}$ for water as well as methanol as shown in Table 5.4 and displayed in Fig. 5.10. With 0 V/nm, $\Delta U_{\text{system}}$ for ethanol is lower than that for water, *i.e.* −265.80 and 63.18 kJ/mol, respectively. This explains the cause of ethanol preference to fill CNTs over water (Fig. 5.1). The LJ potential energy (the interaction of CNT–ethanol) is the dominant factor to determine the $\Delta U_{\text{system}}$ of ethanol (Table 5.3). Along with the increase of CNT diameter, the $\Delta U_{\text{LJ}}$ increases, hence the separation effect without the electric field significantly decreases.

$\Delta U_{\text{system}}$ of water tends to be lower than that of ethanol with the presence of an electric field. With 1 and 2 V/nm, $\Delta U_{\text{system}}$ of water is much lower than that of ethanol (Fig 5.10). This causes water to strongly prefer to fill CNTs over ethanol (Fig. 5.1). With an electric field, the Coulomb potential energy (the electrostatic interaction within the water molecules structure) is the main factor to determine the $\Delta U_{\text{system}}$ of water. The electrostatic interaction is not weaker with the increase of the CNT diameter. As a result, the separation effect with an electric field does not decrease for a wide range of the diameter.

Actually, with 0.5, 1 and 2 V/nm, the $\Delta U_{\text{total}}$ per molecule for ethanol is lower than that for water due to the contribution of the $\Delta U_{\text{LJ}}$ and the $\Delta U_{\text{coulomb}}$. However, since the occupancy of water molecules in the CNT is much higher than that of ethanol molecules, the $\Delta U_{\text{system}}$ for water is much lower. The occupancy of water in a CNT is higher than that of ethanol because the size of a water molecule is smaller than that of an ethanol molecule. Another reason is water molecules can form hydrogen bond network with all of their atoms. This makes the structure of water molecules in the CNT is more compact and contains more molecules. This result suggests that with the electric field and CNTs water can be effectively separated from the other longer alcohol molecules such as propanol, butanol, *etc*.

**Table 5.4**  $\Delta U_{\text{system}}$ for (8,8) CNT and the reservoirs filled with water molecules (CNT–water system), methanol molecules (CNT–methanol system), and ethanol molecules (CNT–ethanol system). The $\Delta U_{\text{system}}$ is defined as the $\Delta U_{\text{total}}$ per molecule multiplied by the number of molecules occupied in the CNT.

| $E$ [V/nm] | Molecule | $\Delta U_{\text{total}}$ [kJ/mol] | Occupancy in CNT | $\Delta U_{\text{system}}$ [kJ/mol] |
|---|---|---|---|---|
| 0 | Water | 1.76 | 35.9 | 63.18 |
| | Methanol | −10.72 | 16.7 | −179.02 |
| | Ethanol | −22.15 | 12.0 | −265.80 |
| 0.5 | Water | −11.60 | 40.6 | −470.96 |
| | Methanol | −24.71 | 19.6 | −484.32 |
| | Ethanol | −30.37 | 12.6 | −382.66 |
| 1 | Water | −20.68 | 47.7 | −986.44 |
| | Methanol | −29.58 | 19.7 | −582.73 |
| | Ethanol | −32.92 | 12.8 | −421.38 |
| 2 | Water | −30.32 | 49.6 | −1503.87 |
| | Methanol | −32.14 | 19.3 | −620.30 |
| | Ethanol | −32.09 | 12.8 | −410.75 |
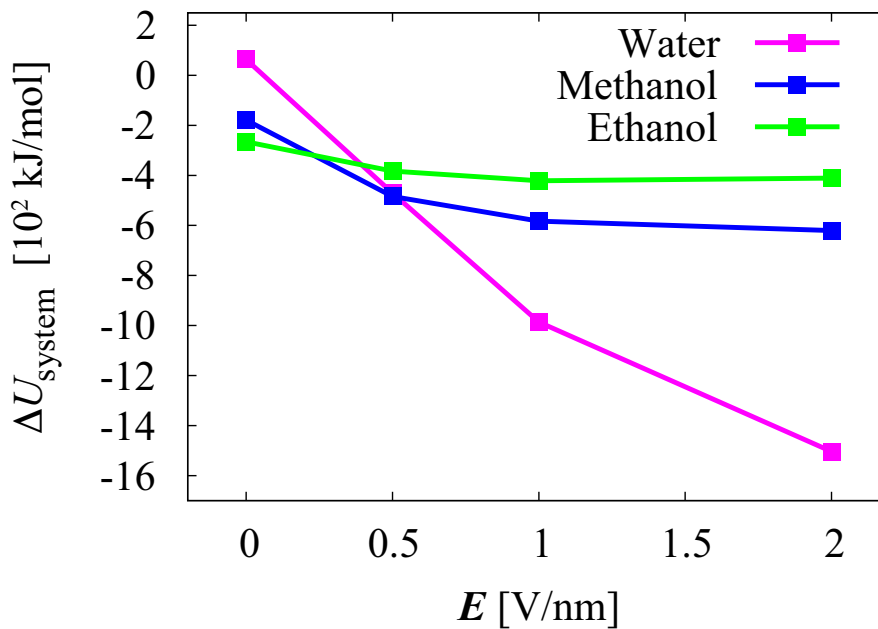


**Fig. 5.10** Comparison of $\Delta U_{\text{system}}$ for water (CNT–water system), methanol (CNT–methanol system), and ethanol (CNT–ethanol system) with (8,8) CNT. With the electric field, $\Delta U_{\text{system}}$ of water is lower than that of methanol and ethanol. This suggests water fill the CNT in preference to methanol and ethanol.

_____

### *5.3.3  Separation of methanol–ethanol mixture with CNTs and electric fields*

There is a significant difference between $\Delta U_{\text{system}}$ for ethanol and methanol in Fig. 5.10 both without and with an electric field. It is thus expected that the separation of a methanol–ethanol solution can be performed using CNTs without and with an electric field. To examine the separation effect for methanol–ethanol solution, we carried out simulations by filling the reservoirs with a mixture of methanol–ethanol molecules where the mole fraction of methanol (or ethanol) is 50%. The CNT diameter was varied, *i.e.* 0.95 nm, 1.08 nm, 1.36 nm, 1.63 nm, 2.03 nm, 2.71 nm, 3.39 nm, and 4.07 nm for (7,7), (8,8), (10,10), (12,12), (15,15), (20,20), (25,25), and (30,30) CNTs, respectively. Figure 5.11 shows the separation effect for a methanol–ethanol solution without and with electric fields.

With 0 V/nm, $\chi_{\text{ethanol}}$ in the CNTs is larger than that in the reservoirs. Without an electric field, ethanol molecules preferentially fill CNTs over methanol, resulting in a separation effect for ethanol. This result confirms with the calculation in the Table 5.4 (or Fig. 5.10) in which the $\Delta U_{\text{system}}$ for ethanol is lower than that for methanol. With 0 V/nm, the van der Waals interaction of ethanol–CNT is the main factor to determine the separation effect. However, the interaction significantly decreases with the increase of CNT diameter. As a result, the separation effect decreases with the increase of the diameter (Fig. 5.11).

In contrast, with 0.5, 1, and 2 V/nm of electric fields, $\chi_{\text{methanol}}$ in the CNTs is larger than that in the reservoirs (Fig. 5.11). This indicates methanol prefers to flow into the CNTs over ethanol, producing a separation effect for methanol. This confirms with the result in the Fig. 5.10 where the $\Delta U_{\text{system}}$ of methanol is lower than that of ethanol. The electrostatic interaction within methanol molecules structure determines the separation effect with an electric field. The interaction depends on the molecules structure instead of CNT diameter. As a result, the separation effect with an electric field is stronger for a wide range of CNT diameter.

With an electric field, the $\Delta U_{\text{total}}$ per molecules for ethanol and methanol is similar (Table 5.4). The occupancy difference makes the $\Delta U_{\text{system}}$ of methanol significantly lower than that of ethanol. The molecular size causes this occupancy difference. Therefore, this suggests that CNTs and the electric fields can be applied to separate one type of alcohol from another alcohol based on the difference of their molecular size.
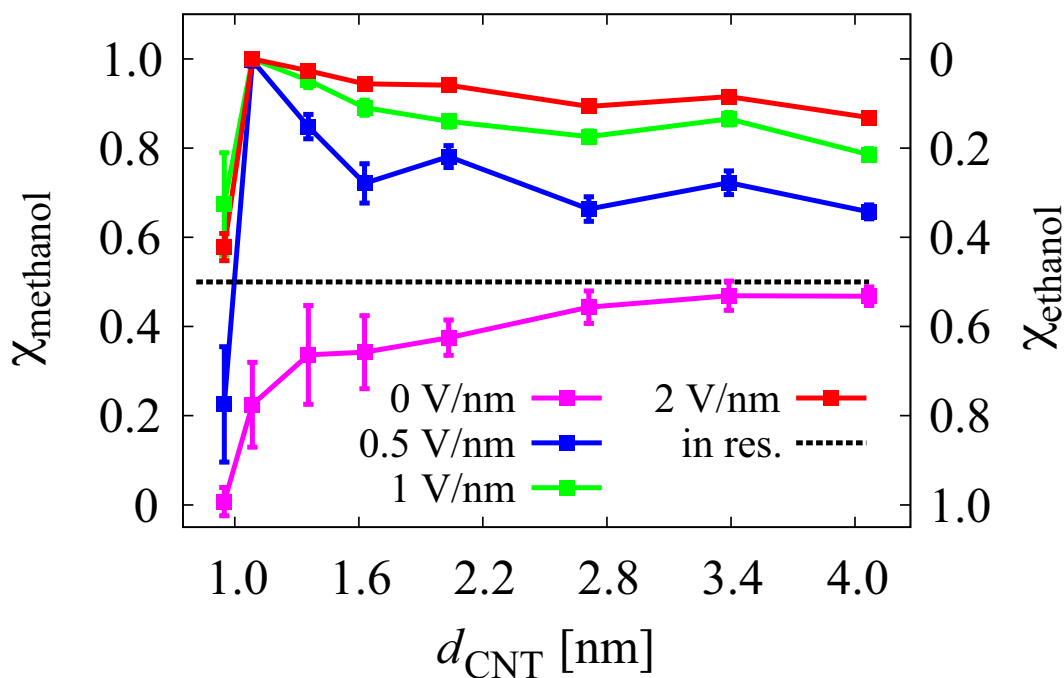
**Fig. 5.11** Mole fraction of methanol molecules $\chi_{methanol}$ (or ethanol molecules $\chi_{ethanol}$) in (7,7) to (30,30) CNTs with 0, 0.5, 1, and 2 V/nm of electric fields. The black dotted-lines shows the mole fraction in the reservoir (res.), *i.e.* $\chi_{methanol} = \chi_{ethanol} = 0.5$. The error bars represent the standard deviation.

## 5.4  Conclusions

Applying the molecular dynamics simulations, we demonstrated the effect of axial electric fields on the separation of water–ethanol solutions using CNTs. Without an electric field, CNTs prefer to adsorb ethanol over water, producing a separation effect for ethanol. The van der Waals interaction of CNT–ethanol is the main factor to determine the separation effect without an electric field. However, as the CNT diameter increases the separation effect decreases significantly due to the decrease of the van der Waals interaction. On the contrary, with an electric field, water flows into CNTs in preference to ethanol, resulting in a separation effect for water. Water molecules in the CNTs form ordered structures. Formation of the ordered structures strengthens the electrostatics interaction between the water molecules. The electrostatic interaction within the water molecules structure is then a key factor for the separation with an electric field. Moreover, the electrostatic interaction depends on the water molecules structure in CNT rather than on the CNT diameter. As a result, the separation effect with an electric field

does not significantly decrease with the increase of the CNT diameter.

CNTs and electric fields are also effective to separate a methanol–ethanol solution. Without an electric field, ethanol preferentially fills into CNTs over methanol, resulting in a separation effect for ethanol. The van der Waals interaction of CNT–ethanol causes the separation effect without an electric field. However, the interaction decreases with the increase of CNT diameter, hence a strong separation effect is observed only with a small CNT diameter. With the presence of an electric field, methanol prefers to occupy CNTs over ethanol. This means a separation effect for methanol. The electrostatic interaction between methanol molecules in the CNTs is an important factor for the separation effect with the electric field. The electrostatic interaction depends on the molecules structures instead of the CNT diameter. As a result, the separation effect of a methanol–ethanol solution with an electric field is strong for a wide range of CNT diameter.

# Chapter 6

# CONCLUSIONS

Molecular dynamics simulations have been performed to investigate the effects of the electric fields on water molecules in carbon nanotubes (CNTs). Moreover, this work investigates the effect of the electric fields on the separation of water–methanol solutions and water–ethanol solutions with CNTs. The main results of the research can be summarized as follows.

An electric field changes the orientation of water molecules in which the direction of the dipole moment is parallel to that of the electric field. Thus, under the influence of an electric field, the water molecules carry the same orientation. The uniformly molecular orientation then facilitates the water molecules in CNTs to build hydrogen bond network and form ordered structures, *i.e.* solid-like structures or ice nanotubes structures. Formation of the ordered structures strengthens the electrostatic interaction between the water molecules. As a result, water structures in the CNTs are more stable and water molecules favor to fill CNTs. In other word, the electric field facilitates water to flow into CNTs. This property is important for inducing a separation effect.

Without an electric field, CNTs preferentially adsorb methanol molecules or ethanol molecules over water molecules. This results a separation effect for methanol or ethanol. The van der Waals interaction of CNT–methanol or CNT–ethanol causes the separation effect without an electric field. However, the van der Waals interaction significantly decreases with an increase of the CNT diameter. Consequently, the separation effect without an electric field is strong only with small CNT diameters and significantly decreases with an increase of the diameter. In contrast, with an electric field, water molecules prefer to fill CNTs over methanol molecules or ethanol molecules, resulting in a separation effect for water. Water molecules in the CNTs form the ordered structures, which are the ice nanotubes structures. The electrostatic interaction within the water molecules structures is thus the main factor for the separation effect with an electric field. The electrostatic interaction depends on the molecules structures rather than the CNT diameter. As a result, the separation effect with an electric field is stronger and

does not decrease for a wide range of the CNT diameter. This work also suggests that with the electric fields and CNTs, water can be separated from other types of alcohol solutions such as propanol, butanol, *etc*.

The formation of the solid-like structures or phase transition from liquid to solid induced with the electric field plays an important role for the water's preference to fill CNTs. Hence, liquid to solid phase diagram should be established for the forthcoming work. Temperature and pressure should be considered in the phase diagram construction in addition to the electric field and CNT diameter. Simulation with other water molecule models should be performed to investigate how sensitive the effect of different water models on the formation of ice nanotubes structures and the separation effect. Simulation system with multiple CNTs rather than only one CNT in the simulation box should be considered to demonstrate the effect of the neighbor tubes in the future work. Therefore, the system can mimic the real membranes more closely. Separation effect for lower water concentration in the reservoirs ($\chi_{water} << 0.19$) is still possible as long as the water can form the ordered structures in the CNTs. However, the equilibrium condition may take a long time in a simulation with very low water concentration. Electrostatic interaction within the water structures is the main factor for the separation effect with the electric field instead of the interaction with CNT wall. Thus, it is possible for other hydrophobic nanotubes such as boron nitride nanotubes (BNNTs) to exhibit the same separation effect. BNNTs can transport water rapidly as well.

Finally, we note that one elementary charge in vacuum space can generate electric fields of 0.36 and 0.06 V/nm at distances of 2 and 5 nm which are exceptionally large on macroscopic length scale. Although the electric fields applied in this study is extremely large for macroscopic scale, but with nanotechnology it seems feasible to provide the electric field in this order. Hence, this work highlights a promise of an alternative method to produce a nearly pure alcohol in the future. At very low water concentration, the separation effect may decrease, however, combination with the existing methods should deliver a more effective technique.

# Bibliography

[1] S. Iijima, Helical microtubules of graphitic carbon, *Nature*, vol. 354, pp. 56-58, 1991

[2] R. H. Baughman, A. A. Zakhidov, W. A. de Heer, Carbon nanotubes–the route toward application, *Science*, vol. 297, pp. 787-792, 2002

[3] M. F. L. De Volder, S. H. Tawfick, R. H. Baughman, A. J. Hart, Carbon nanotubes: present and future commercial applications, *Science*, vol. 339, pp. 535-539, 2013

[4] G. Hummer, J. C. Rasaiah, and J. P. Noworyta, Water conduction through the hydrophobic channel of a carbon nanotube, *Nature*, vol. 414, pp. 188-190, 2001

[5] M. S. Dresselhaus, G. Dresselhaus, and A. Jorio, Unusual properties and structure of carbon nanotubes, *Annual Review of Materials Research*, vol. 34, pp. 247-278, 2004

[6] M. S. Dresselhaus, G. Dresselhaus, and R. Saito, Physics of carbon nanotubes, *Carbon*, vol. 33, pp. 883-891, 1995

[7] M. Terrones, Science and technology of the twenty-first century: synthesis, properties, and applications of carbon nanotubes, *Annual Review of Materials Research*, vol. 33, pp. 419-501, 2003

[8] J. C. T. Eijkel and A. van den Berg, Nanofluidics: What is it and what can we expect from it?, *Microfluidics and Nanofluidics*, vol. 1, pp. 249-267, 2005

[9] W. Sparreboom, A. van den Berg, and J. C. T. Eijkel, Transport in nanofluidic systems: A review of theory and applications, *New Journal of Physics*, vol. 12, pp. 15004, 2010

[10] A. Kalra, S. Garde, and G. Hummer, Osmotic water transport through carbon nanotube membranes, *Proceedings of the National Academy of Sciences of the United States of America*, vol. 100, pp. 10175-10180, 2003

[11] S. Joseph and N. R. Aluru, Why are carbon nanotubes fast transporter of water?, *Nano Letters*, vol. 8, pp. 452-458, 2008

[12] J. A. Thomas and A. J. H. McGaughey, Reassessing fast water transport through carbon nanotubes, *Nano Letters*, vol. 8, pp. 2788-2793, 2008

[13] J. H. Walther, K. Ritos, E. R. Cruz-Chu, C. M. Megaridis, and P. Koumoutsakos, Barriers to superfast water transport in carbon nanotube membranes, *Nano Letters*, vol. 13, pp. 1910-1914, 2013

[14] A. I. Skoulidas, D. M. Ackerman, J. K. Johnson, and D. S. Sholl, Rapid transport of gases in carbon nanotubes, *Physical Review Letters*, vol. 89, pp. 185901, 2002

[15] M. Majumder, N. Chopra, R. Andrew, and B. J. Hinds, Enhanced flow in carbon nanotubes, *Nature*, vol. 438, pp. 44, 2005

[16] X. Qin, Q. Yuan, Y. Zhao, S. Xie, and Z. Liu, Measurement of the rate of water translocation through carbon nanotubes, *Nano Letters*, vol. 11, pp. 2173-2177, 2011

[17] M. Whitby, L. Cagnon, M. Thanou, and N. Quirke, Enhanced fluid flow through nanoscale carbon pipes, *Nano Letters*, vol. 8, pp. 2632-2637, 2008

[18] J. K. Holt, H. G. Park, Y. Wang, M. Stadermann, A. B. Artyukhin, C. P. Grigoropoulos, A. Noy, and O. Bakajin, Fast mass transport through sub 2-nanometer carbon nanotubes, *Science*, vol. 312, pp. 1034-1037, 2006

[19] P. Agre, Aquaporin water channels (nobel lecture), *Angewandte Chemie International Edition*, vol. 43, pp. 4278-4290

[20] P. Agree, D. Kozono, Aquaporin water channels: Molecular mechanism for human diseases, *FEBS Letters*, vol. 555, pp. 72-78, 2003

[21] B. L. de Groot and H. Grubmüller, Water permeation across biological membranes: Mechanism and dynamics of aquaporin-1 and GlpF, *Science*, vol. 294, pp. 2353-2357, 2001

[22] M. S. P. Sansom and P. C. Biggin, Water at the nanoscale, *Nature*, vol. 414, pp. 156-159, 2001

[23] A. Noy, H. G. Park, F. Fornasiero, J. K. Holt, C. P. Grigoropoulos, and O. Bakajin, Nanofluidics in carbon nanotubes, *Nano Today*, vol. 2, pp. 22-29, 2007

[24] J. K. Holt, Carbon nanotubes and nanofluidic transport, *Advance Materials*, vol. 21, pp. 3542-3550, 2009

[25] J. C. Rasaiah, S. Garde, and G. Hummer, Water in nonpolar confinement: From nanotubes to proteins and beyond, *Annual Review of Physical Chemistry*, vol. 59, pp. 713-740, 2008

[26] J. P. Rothstein, Slip on superhydrophobic surfaces, *Annual Review of Fluid Mechanics*, vol. 42, pp. 89-109, 2010

[27] S. K. Kannam, B. D. Todd, J. S. Hansen, and P. J. Daivis, How fast does water flow in carbon nanotubes?, *The Journal of Chemical Physics*, vol. 138, pp. 94701-94709, 2013

[28] J. Eijkel, Liquid slip in micro and nanofluidics: Recent research and its possible implications, *Lab on a Chip*, vol. 7, pp. 299-301, 2007

[29] D. Lohse, Surface nanobubbles and nanodroplets, *Review of Modern Physics*, vol. 87, pp. 981-1035, 2015

[30] P. G. de Gennes, On fluid/wall slippage, *Langmuir*, vol. 18, pp. 3413-3414, 2002

[31] S. Granick, Motion and relaxations of confined liquids, *Science*, vol. 253, pp. 1374-1379, 1991

[32] R. Zangi, Water confined to a slab geometry: A review of recent computer simulation studies, *Journal of Physics: Condensed Matter*, vol. 16, pp. S5371-S5388, 2004

[33] A. Alexiadis and S. Kassinos, Molecular simulation of water in carbon nanotubes, *Chemical Reviews*, vol. 108, pp. 5014-5034, 2008

[34] M. Majumder, N. Chopra, and B. J. Hinds, Effect of tip functionalization on transport through vertically oriented carbon nanotube membranes, *Journal of the American Chemical Society*, vol. 127, pp. 9062-9070, 2005

[35] B. Corry, Designing carbon nanotube membranes for efficient water desalination, *The Journal of Physical Chemistry B*, vol. 112, pp. 1427-1434, 2008

[36] B. Corry, Water and ion transport through functionalized carbon nanotubes: Implications for desalination technology, *Energy and Environmental Science*, vol. 4, pp. 751-759, 2011

[37] W.-F. Chan, H.-Y. Chen, A. Surapathi, M. G. Taylor, X. Shao, E. Marand, and J. K. Johnson, Zwitterion functionalized carbon nanotube/polyamide nanocomposite membranes for water desalination, *ACS Nano*, vol. 7, pp. 5308-5319, 2013

[38] J. Goldsmith and C. C. Martens, Molecular dynamics simulation of salt rejection in model surface-modified nanopores, *The Journal of Physical Chemistry Letters*, vol. 1, pp. 528-535, 2010

[39] G. Arora and S. I. Sandler, Air separation by single wall carbon nanotubes: Thermodynamics and adsorptive selectivity, *The Journal of Chemical Physics*, vol. 123, pp. 44705-44713, 2005

[40] G. Arora and S. I. Sandler, Molecular sieving using single wall carbon nanotubes, *Nano Letter*, vol. 7, pp. 565-569, 2007

[41] H. Chen and D. S. Sholl, Predictions of selectivity and flux for $CH_4/H_2$ separations using single walled carbon nanotubes as membranes, *Journal of Membrane Science*, vol. 269, pp. 152-160, 2006

[42] J. Lee and N. R. Aluru, Separation of gases from gas-water mixture using carbon nanotubes, *Applied Physics Latters*, vol. 96, pp. 133108-133110, 2010

[43] S. K. Vashist, D. Zheng, G. Pastorin, K. Al-Rubeaan, J. H. T. Luong, F-S, Sheu, Delivery of drugs and biomolecules using carbon nanotubes, *Carbon*, vol. 49, pp. 4077-4097, 2011

[44] C. Fabbro, H. Ali-Boucetta, T. D. Ros, K. Kostarelos, A. Bianco, and M. Prato, Targeting carbon nanotubes against cancer, *Chemical Communications*, vol. 48, pp. 3911-3926, 2012

[45] B. Hille, Ionic channels in excitable membranes, current problems and biophysical approaches, *Biophysical Journal*, vol. 22, pp. 283-294, 1978

[46] A. Philippsen, W. Im, A. Engel, T. Schirmer, B. Roux, and D. J. Müller, Imaging the electrostatic potential of transmembrane channels: Atomic probe microscopy of OmpF porin, *Biophysical Journal*, vol. 82, pp. 1667-1676, 2002

[47] M. L. Berkowitz, D. L. Bostick, and S. Pandit, Aqueous solutions next to phospholipid membrane surfaces: Insights from simulations, *Chemical Reviews*, vol. 106, pp. 1527-1539, 2006

[48] M. F. Toney, J. N. Howard, J. Richer, G. L. Borges, J. G. Gordon, O. R. Melroy, D. G. Wiesler, D. Yee, and L. B. Sorensen, Voltage-dependent ordering of water molecules at an electrode-electrolyte interface, *Nature*, vol. 368, pp. 444-446, 1994

[49] R. Simons, Strong electric field effects on proton transfer between membrane-bound amines and water, *Nature*, vol. 280, pp. 824-826, 1979

[50] M. G. Nikolaides, A. R. Bausch, M. F. Hsu, A. D. Dinsmore, M. P. Brenner, C. Gay, and D. A. Weitz, Electric-field-induced capillary attraction between like-charged particles at liquid interfaces, *Nature*, vol. 420, pp. 299-301, 2002

[51] J. Dzubiella and J.-P. Hansen, Electric-field-controlled water and ion permeation of a hydrophobic nanopore, *The Journal of Chemical Physics*, vol. 122, pp. 234706-234719, 2005

[52] S. Vaitheeswaran, J. C. Rasaiah, and G. Hummer, Electric field and temperature effects on water in the narrow nonpolar pores of carbon nanotubes, *The Journal of Chemical Physics*, vol. 121, pp. 7955-7965, 2004

[53] Z. Fu, Y. Luo, J. Ma, and G. Wei, Phase transition of nanotube-confined water driven by electric field, *The Journal of Chemical Physics*, vol. 134, pp. 154507-154512, 2011

[54] R. Zangi and A. E. Mark, Electrofreezing of confined water, *The Journal of Chemical Physics*, vol. 120, pp. 7123-7130, 2004

[55] E.-M. Choi, Y.-H. Yoon, S. Lee, and H. Kang, Freezing transition of interfacial water at room temperature under electric fields, *Physical Review Letters*, vol. 95, pp. 85701-85704, 2005

[56] K. F. Rinne, S. Gekle, D. J. Bonthuis, and R. R. Netz, Nanoscale pumping of water by AC electric fields, *Nano Letters*, vol. 12, pp. 1780-1783, 2012

[57] S. De Luca, B. D. Todd, J. S. Hansen, and P. J. Daivis, Molecular dynamics study of nanoconfined water flow driven by rotating electric fields under realistic experimental conditions, *Langmuir*, vol. 30, pp. 3095-3109, 2014

[58] M. E. Suk and N. R. Aluru, Effect of induced electric field on single-file reverse osmosis, *Physical Chemistry Chemical Physics*, vol. 11, pp. 8614-8619, 2009

[59] D. Frenkel and B. Smit, *Understanding molecular simulation, from algorithms to applications*, Academic Press, 2$^{nd}$ Ed., San Diego USA, 2002

[60] F. Ercolessi, *A molecular dynamics primer*, International School for Advanced Studies, Trieste-Italy, http://www.sissa.it/furio/

[61] A. R. Leach, *Molecular modeling, principle and applications*, Pearson Prentice Hall, 2$^{nd}$ Ed., Harlow England, 2001

[62] M. P. Allen and D. J. Tildesley, *Computer simulation of liquids*, Oxford University Press, New York USA, 2009

[63] M. E. Tuckerman, *Statistical mechanics: theory and molecular simulation*, Oxford University Press, New York USA, 2010

[64] A. Satoh, *Introduction to practice of molecular simulation*, Elsevier, 1$^{st}$ Ed., London, 2011

[65] X. Gong, J. Li, H. Lu, R. Wan, J. Li, J. Hu, and H. Fang, A charge-driven molecular water pump, *Nature Nanotechnology*, vol. 2, pp. 709-712, 2007

[66] M. J. Longhurst and N. Quirke, Temperature-driven pumping of fluid through single-walled carbon nanotubes, *Nano Letters*, vol. 7, pp. 3324-3328, 2007

[67] Z. Insepov, D. Wolf, and A. Hassanein, Nanopumping using carbon nanotubes, *Nano Letters*, vol. 6, pp. 1893-1895, 2006

[68] J. Kou, X. Zhou, H. Lu, Y. Xu, F. Wu, and J. Fan, A vibration-charge-induced unidirectional transport of water molecules in confined nanochannels, *Soft Matter*, vol. 8, pp. 12111-12115, 2012

[69] Y. Wang, Y. J. Zhao, and J. P. Huang, Giant pumping of single-file water molecules in a carbon nanotube, *The Journal of Physical Chemistry B*, vol. 115, pp. 13275-13279, 2011

[70] A. Bianco, K. Kostarelos, and M. Prato, Applications of carbon nanotubes in drug delivery, *Current Opinion in Chemical Biology*, vol. 9, pp. 674-679, 2005

[71] K. Kostarelos, A. Bianco, and M. Prato, Promises, facts and challenges for carbon nanotubes in imaging and therapeutics, *Nature Nanotechnology*, vol. 4, pp. 627-633, 2009

[72] H. Nagai, Y. Okazaki, S. H. Chew, N. Misawa, Y. Yamashita, S. Akatsuka, T. Ishihara, K. Yamashita, Y. Yoshikawa, H. Yasui, *et al.*, Diameter and rigidity of multiwalled carbon nanotubes are critical factors in mesothelial injury and carcinogenesis, *Proceedings of the National Academy of Sciences of the United States of America*, vol. 108, pp. E1330-E1338, 2011

[73] K. Koga, G. T. Gao, H. Tanaka, and X. C. Zeng, Formation of ordered ice nanotubes inside carbon nanotubes, *Nature*, vol. 412, pp. 802-805, 2001

[74] J. Bai, J. Wang, and X. C. Zeng, Multiwalled ice helixes and ice nanotubes, *Proceedings of the National Academy of Sciences of the United States of America*, vol. 103, pp. 19664-19667, 2006

[75] W. H. Noon, K. D. Ausman, R. E. Smalley, and J. Ma, Helical ice-sheets inside carbon nanotubes in the physiological condition, *Chemical Physics Letters*, vol. 355, pp. 445-448, 2002

[76] Y. Liu, Q. Wang, T. Wu, and L. Zhang, Fluid structure and transport properties of water inside carbon nanotubes, *The Journal of Chemical Physics*, vol. 123, pp. 234701-234707, 2005

[77] D. Takaiwa, I. Hatano, K. Koga, and H. Tanaka, Phase diagram of water in carbon nanotubes, *Proceedings of the National Academy of Sciences of the United States of America*, vol. 105, pp. 39-43, 2008

[78] Y. Maniwa, H. Kataura, M. Abe, S. Suzuki, Y. Achiba, H. Kira, and K. Matsuda, Phase transition in confined water inside carbon nanotubes, *Journal of the Physical Society of Japan*, vol. 71, pp. 2863-2866, 2002

[79] Y. Maniwa, H. Kataura, M. Abe, A. Udaka, S. Suzuki, Y. Achiba, H. Kira, K. Matsuda, H. Kadowaki, and Y. Okabe, Ordered water inside carbon nanotubes: Formation of pentagonal to octagonal ice-nanotubes, *Chemical Physics Letters*, vol. 401, pp. 534-538, 2005

[80] S. Ghosh, K. V. Ramanathan, and A. K. Sood, Water at nanoscale confined in single-walled carbon nanotubes studied by NMR, *Europhysics Letters*, vol. 65, pp. 678-684, 2004

[81] A. I. Kolesnikov, J.-M. Zanotti, C.-K. Loong, P. Thiyagarajan, A. P. Moravsky, R. O. Loutfy, and C. J. Burnham, Anomalously soft dynamics of water in a nanotube: A revelation of nanoscale confinement, *Physical Review Letters*, vol. 93, pp. 035503-035506, 2004

[82] O. Byl, J.-C. Liu, Y. Wang, W.-L. Yim, J. K. Johnson, and J. T. Yates, Jr., Unusual hydrogen bonding in water-filled carbon nanotubes, *Journal of the American Chemical Society*, vol. 128, pp. 12090-12097, 2006

[83] S. Joseph and N. R. Aluru, Pumping of confined water in carbon nanotubes by rotation-translation coupling, *Physical Review Letters*, vol. 101, pp. 064502-064505, 2008

[84] J. Su and H. Guo, Control of unidirectional transport of single-file water molecules through carbon nanotubes in an electric field, *ACS Nano*, vol. 5, pp. 351-359, 2011

[85] X. Wu, L. Lu, Y. Zhu, M. Wei, X. Guo, and X. Lu, Changes in CNT-confined water structural properties induced by the variation in water molecule orientation, *Molecular Simulation*, vol. 38, pp. 1094-1102, 2012

[86] Z. Qian, Z. Fu, and G. Wei, Influence of electric fields on the structure and structure transition of water confined in a carbon nanotube, *The Journal of Chemical Physics*, vol. 140, pp. 154508-154514, 2014

[87] Y. He, G. Sun, K. Koga, and L. Xu, Electrostatic field-exposed water in nanotube at constant axial pressure, *Scientific Reports*, vol. 4, pp. 6596-6600, 2014

[88] D. J. Bonthuis, K. Falk, C. N. Kaplan, D. Horinek, A. N. Berker, L. Bocquet, and R. R. Netz, Comment on "Pumping of confined water in carbon nanotubes by rotation-translation coupling", *Physical Review Letters*, vol. 105, pp. 209401, 2010

[89] D. J. Bonthuis, K. F. Rinne, K. Falk, C. N. Kaplan, D. Horinek, A. N. Berker, L. Bocquet, and R. R. Netz, Theory and simulations of water flow through carbon nanotubes: prospects and pitfalls, *Journal of Physics: Condensed Matter*, vol. 23, pp. 184110-184119, 2011

[90] H. J. C. Berendsen, J. P. M. Postma, W. F. van Gunsteren, and J. Hermans, Interaction models for water in relation to protein hydration, *Intermolecular Forces*, vol. 14, pp. 331-342, 1981

[91] B. Hess, C. Kutzner, D. van der Spoel, and E. Lindahl, GROMACS 4: Algorithms for highly efficient, load-balanced, and scalable molecular simulation, *Journal of Chemical Theory and Computation*, vol. 4, pp. 435-447, 2008

[92] T. Darden, D. York, and L. Pedersen, Particle mesh Ewald: An $N.\log(N)$ method for Ewald sums in large systems, *The Journal of Chemical Physics*, vol. 98, pp. 10089-10092, 1993

[93] J.-P. Ryckaert, G. Ciccotti, and H. J. C. Berendsen, Numerical integration of the cartesian equations of motion of a system with constraints: Molecular dynamics of *n*-alkanes, *Journal of Computational Physics*, vol. 23, pp. 327-341, 1977

[94] S. Nosé, A unified formulation of the constant temperature molecular dynamics methods, *The Journal of Chemical Physics,* vol. 81, pp. 511-519, 1984

[95] W. G. Hoover, Canonical dynamics: Equilibrium phase-space distributions, *Physical Review A*, vol. 31, pp. 1695-1697, 1985

[96] M. Parrinello and A. Rahman, Polymorphic transitions in single crystals: A new molecular dynamics method, *Journal of Applied Physics*, vol. 52, pp. 7182-7190, 1981

[97] J. Martí, G. Nagy, M. C. Gordillo, and E. Guàrdia, Molecular simulation of liquid water confined inside graphite channels: Thermodynamics and structural properties, *The Journal of Chemical Physics*, vol. 124, pp. 094703-094709, 2006

[98] M. C. Gordillo and J. Martí, Structure of water adsorbed on a single graphene sheet, *Physical Review B*, vol. 78, pp. 075432-075436, 2008

[99] M. C. Gordillo, G. Nagy, and J. Martí, Structure of water nanoconfined between hydrophobic surfaces, *The Journal of Chemical Physics*, vol. 123, pp. 054707-054715, 2005

[100] J. Wang, Y. Zhu, J. Zhou, and X.-H. Lu, Diameter and helicity effects on static properties of water molecules confined in carbon nanotubes, *Physical Chemistry Chemical Physics*, vol. 6, pp. 829-835, 2004

[101] D. Takaiwa, K. Koga, and H. Tanaka, Structures of filled ice nanotubes inside carbon nanotubes, *Molecular Simulation*, vol. 33, pp. 127-132, 2007

[102] J. B. Kaelberer and R. D. Etters, Phase transitions in small clusters of atoms, *The Journal of Chemical Physics*, vol. 66, pp. 3233-3239, 1977

[103]  Y. Zhou, M. Karplus, K. D. Ball, and R. S. Berry, The distance fluctuation criterion for melting: Comparison of square-well and Morse potential models for clusters and homopolymers, *The Journal of Chemical Physics*, vol. 116, pp. 2323-2329, 2002

[104]  F. Ding, K. Bolton, and A. Rosén, Molecular dynamics study of the surface melting of iron clusters, *The European Physical Journal D*, vol. 34, pp. 275-277, 2005

[105]  K. Zhang, G. M. Stocks, and J. Zhong, Melting and premelting of carbon nanotubes, *Nanotechnology*, vol. 18, pp. 285703-285707, 2007

[106]  J. Martí, Analysis of the hydrogen bonding and vibrational spectra of supercritical model water by molecular dynamics simulations, *The Journal of Chemical Physics*, vol. 110, pp. 6876-6886, 1999

[107]  M. C. Gordillo and J. Martí, Hydrogen bond structure of liquid water confined in nanotubes, *Chemical Physics Letters*, vol. 329, pp. 341-345, 2000

[108]  A. Luzar and D. Chandler, Hydrogen-bond kinetics in liquid water, *Nature*, vol. 379, pp. 55-57, 1996

[109]  S. Paul and A. Chandra, Hydrogen bond dynamics at vapour–water and metal–water interfaces, *Chemical Physics Letters*, vol. 386, pp. 218-224, 2004

[110]  L. Figueras and J. Faraudo, Competition between hydrogen bonding and electric field in single-file transport of water in carbon nanotubes, *Molecular Simulation*, vol. 38, pp. 23-25, 2012

[111]  W.-H. Zhao, J. Bai, L.-F. Yuan, J. Yang, and X. C. Zeng, Ferroelectric hexagonal and rhombic monolayer ice phases, *Chemical Science*, vol. 5, pp. 1757-1764, 2014

[112]  H. Qiu and W. Guo, Electromelting of confined monolayer ice, *Physical Review Letters*, vol. 110, pp. 195701-195705, 2013

[113]  G. A. Olah, Beyond oil and gas: the methanol economy, *Angewandte Chemie International Edition*, vol. 44, pp. 2636-2639, 2005

[114]  D. W. Stephan, A step closer to a methanol economy, *Nature*, vol. 495, pp. 54-55, 2013

[115]  M. Nielsen, E. Alberico, W. Baumann, H.-J. Drexler, H. Junge, S. Gladiali and M. Beller, Low-temperature aqueous-phase methanol dehydrogenation to hydrogen and carbon dioxide, *Nature*, vol. 495, pp. 85-89, 2013

[116]  M. Barinaga, California introduces methanol for cars in pollution fight, *Nature*,

_____

vol. 327, pp. 361, 1987

[117]  L. Shenghua, E. R. Cuty Clemente, H. Tiegang and W. Yanjv, Study of spark ignition engine fueled with methanol/gasoline fuel blends, *Applied Thermal Engineering*, vol. 27, pp. 1904-1910, 2007

[118]  W. Yanju, L. Shenghua, L. Hongsong, Y. Rui, L. Jie and W. Ying, Effects of methanol/gasoline blends on a spark ignition engine performance and emissions, *Energy and Fuels*, vol. 22, pp. 1254-1259, 2008

[119]  T. Hu, Y. Wei, S. Liu and L. Zhou, Improvement of spark-ignition (SI) engine combustion and emission during cold start, fueled with methanol/gasoline blends, *Energy and Fuels*, vol. 21, pp. 171-175, 2007

[120]  B. Höhlein, P. Biedermann, T. Grube and R. Menzer, Fuel cell power trains for road traffic, *Journal of Power Sources*, vol. 84, pp. 203-213, 1999

[121]  X. Ren, P. Zelenay, S. Thomas, J. Davey and S. Gottesfeld, Recent advances in direct methanol fuel cells at Los Alamos National Laboratory, *Journal of Power Sources*, vol. 86, pp. 111-116, 2000

[122]  D. A. Boysen, T. Uda, C. R. I. Chisholm and S. M. Haile, High-performance solid acid fuel cells through humidity stabilization, *Science*, vol. 303, pp. 68-70, 2004

[123]  J. Zhang, G.-P. Yin, Q.-Z. Lai, Z.-B. Wang, K.-D. Cai and P. Liu, The influence of anode gas diffusion layer on the performance of low-temperature DMFC, *Journal of Power Sources*, vol. 168, pp. 453-458, 2007

[124]  J. Schrader, M. Schilling, D. Holtmann, D. Sell, M. Villela Filho, A. Marx and J. A. Vorholt, Methanol-based industrial biotechnology: current status and future perspectives of methylotrophic bacteria, *Trends in Biotechnology*, vol. 27, pp. 107-115, 2009

[125]  R. D. Cortright, R. R. Davda and J. A. Dumesic, Hydrogen from catalytic reforming of biomass-derived hydrocarbons in liquid water, *Nature*, vol. 418, pp. 964-967, 2002

[126]  T. P. Vispute, H. Zhang, A. Sanna, R. Xiao and G. W. Huber, Renewable chemical commodity feedstocks from integrated catalytic processing of pyrolysis oils, *Science*, vol. 330, pp. 1222-1227, 2010

[127]  J. P. Maity, J. Bundschuh, C.-Y. Chen and P. Bhattacharya, Microalgae for third generation biofuel production, mitigation of greenhouse gas emissions and wastewater treatment: Present and future perspectives–a mini review, *Energy*,

vol. 78, pp. 104-113, 2014

[128] P. Trop, B. Anicic and D. Goricanec, Production of methanol from a mixture of torrefied biomass and coal, *Energy*, vol. 77, pp. 125-132, 2014

[129] Y. Huang, R. W. Baker and L. M. Vane, Low-energy distillation-membrane separation process, *Industrial and Engineering Chemistry Research*, vol. 49, pp. 3760-3768, 2010

[130] K. Liang, W. Li, H. Luo, M. Xia and C. Xu, Energy-efficient extractive distillation process by combining preconcentration column and entrainer recovery column, *Industrial and Engineering Chemistry Research*, vol. 53, pp. 7121-7131, 2014

[131] T. C. Bowen, R. D. Noble and J. L. Falconer, Fundamentals and applications of pervaporation through zeolite membranes, *Journal of Membrane Science*, vol. 245, pp. 1-33, 2004

[132] L. M. Vane, A review of pervaporation for product recovery from biomass fermentation processes, *Journal of Chemical Technology and Biotechnology*, vol. 80, pp. 603-629, 2005

[133] K. Hu, J. Nie, J. Liu and J. Zheng, Separation of methanol from methanol/water mixtures with pervaporation hybrid membranes, *Journal of Applied Polymer Science*, vol. 128, pp. 1469-1475, 2013

[134] G. Rutkai, É. Csányi and T. Kristóf, Prediction of adsorption and separation of water–alcohol mixtures with zeolite NaA, *Microporous and Mesoporous Materials*, vol. 114, pp. 455-464, 2008

[135] T. Remy, J. Cousin Saint Remi, R. Singh, P. A. Webley, G. V. Baron and J. F. M. Denayer, Adsorption and separation of C1-C8 alcohols on SAPO-34, *The Journal of Physical Chemistry C*, vol. 115, pp. 8117-8125, 2011

[136] K. Zhang, R. P. Lively, J. D. Noel, M. E. Dose, B. A. McCool, R. R. Chance and W. J. Koros, Adsorption of water and ethanol in MFI-type zeolites, *Langmuir*, vol. 28, pp. 8664-8673, 2012

[137] D. Nimcevic and J. R. Gapes, The acetone–butanol fermentation in pilot plant and pre-industrial scale, *Journal of Molecular Microbiology and Biotechnology*, vol. 2, pp. 15-20, 2000

[138] A. Chapeaux, L. D. Simoni, T. S. Ronan, M. A. Stadtherr and J. F. Brennecke, Extraction of alcohols from water with 1-hexyl-3-methylimidazolium bis (trifluoromethylsulfonyl) imide, *Green Chemistry*, vol. 10, pp. 1301-1306, 2008

[139] L. M. Chávez-Islas, R. Vasquez-Medrano and A. Flores-Tlacuahuac, Optimal molecular design of ionic liquids for high-purity bioethanol production, *Industrial and Engineering Chemistry Research*, vol. 50, pp. 5153-5168, 2011

[140] J. Zang, S. Konduri, S. Nair and D. S. Sholl, Self-diffusion of water and simple alcohols in single-walled aluminosilicate nanotubes, *ACS Nano*, vol. 3, pp. 1548-1556, 2009

[141] G. Arora and S. I. Sandler, Air separation by single wall carbon nanotubes: Mass transport and kinetic selectivity, *The Journal of Chemical Physics*, vol. 124, pp. 084702, 2006

[142] O. Sae-Khow and S. Mitra, Carbon nanotube immobilized composite hollow fiber membranes for pervaporative removal of volatile organics from water, *The Journal of Physical Chemistry C*, vol. 114, pp. 16351-16356, 2010

[143] J. Zheng, E. M. Lennon, H.-K. Tsao, Y.-J. Sheng and S. Jiang, Transport of a liquid water and methanol mixture through carbon nanotubes under a chemical potential gradient, *The Journal of Chemical Physics*, vol. 122, pp. 214702, 2005

[144] W.-H. Zhao, B. Shang, S.-P. Du, L.-F. Yuan, J. Yang and X. C. Zeng, Highly selective adsorption of methanol in carbon nanotubes immersed in methanol-water solution, *The Journal of Chemical Physics*, vol. 137, pp. 034501, 2012

[145] X. Tian, Z. Yang, B. Zhou, P. Xiu and Y. Tu, Alcohol-induced drying of carbon nanotubes and its implications for alcohol/water separation: A molecular dynamics study, *The Journal of Chemical Physics*, vol. 138, pp. 204711, 2013

[146] F. Mikami, K. Matsuda, H. Kataura and Y. Maniwa, Dielectric properties of water inside single-walled carbon nanotubes, *ACS Nano*, vol. 3, pp. 1279-1287, 2009

[147] B. Xu, Y. Qiao, Q. Zhou and X. Chen, Effect of electric field on liquid infiltration into hydrophobic nanopores, *Langmuir*, vol. 27, pp. 6349-6357, 2011

[148] D. Bratko, C. D. Daub, K. Leung and A. Luzar, Effect of field direction on electrowetting in a nanopore, *Journal of the American Chemical Society*, vol. 129, pp. 2504-2510, 2007

[149] S. De Luca, B. D. Todd, J. S. Hansen and P. J. Daivis, Electropumping of water with rotating electric fields, *The Journal of Chemical Physics*, vol. 138, pp. 154712, 2013

[150] W. L. Jorgensen, Optimized intermolecular potential functions for liquid alcohols, *The Journal of Physical Chemistry*, vol. 90, pp. 1276-1284, 1986

_____

[151] W. L. Jorgensen, J. M. Briggs and M. L. Contreras, Relative partition coefficients for organic solutes from fluid simulations, *The Journal of Physical Chemistry*, vol. 94, pp. 1683-1686, 1990

[152] A. V. Shevade, S. Jiang and K. E. Gubbins, Molecular simulation study of water–methanol mixtures in activated carbon pores, *The Journal of Chemical Physics*, vol. 113, pp. 6933-6942, 2000

[153] A. M. Saitta, F. Saija and P. V. Giaquinta, *Ab initio* molecular dynamics study of dissociation of water under an electric field, *Physical Review Letters*, vol. 108, pp. 207801, 2012

[154] Y. Zhang, T.-T. Tang, C. Girit, Z. Hao, M. C. Martin, A. Zettl, M. F. Crommie, Y. R. Shen and F. Wang, Direct observation of a widely tunable bandgap in bilayer graphene, *Nature*, vol. 459, pp. 820-823, 2009

[155] L. An, J. M. Owens, L. E. McNeil and J. Liu, Synthesis of nearly uniform single-walled carbon nanotubes using identical metal-containing molecular nanoclusters as catalysts, *Journal of the American Chemical Society*, vol. 124, pp. 13688-13689, 2002

[156] A. Okamoto and H. Shinohara, Control of diameter distribution of single-walled carbon nanotubes using the zeolite-CCVD method at atmospheric pressure, *Carbon*, vol. 43, pp. 431-436, 2005

[157] T. Thurakitseree, C. Kramberger, A. Kumamoto, S. Chiashi, E. Einarsson and S. Maruyama, Reversible diameter modulation of single-walled carbon nanotubes by acetonitrile-containing feedstock, *ACS Nano*, vol. 7, pp. 2205-2211, 2013

[158] M. Ferrario, M. Haughney, I. R. McDonald and M. L. Klein, Molecular-dynamics simulation of aqueous mixtures: Methanol, acetone, and ammonia, *The Journal of Chemical Physics*, vol. 93, pp. 5156-5166, 1990

[159] M. Pagliai, G. Cardini, R. Righini and V. Schettino, Hydrogen bond dynamics in liquid methanol, *The Journal of Chemical Physics*, vol. 119, pp. 6655-6662, 2003

[160] A. Berezhkovskii and G. Hummer, Single-file transport of water molecules through a carbon nanotube, *Physical Review Letters*, vol. 89, pp. 64503, 2002

[161] G. Zuo, R. Shen, S. Ma and W. Guo, Transport properties of single-file water molecules inside a carbon nanotube biomimicking water channel, *ACS Nano*, vol. 4, pp. 205-210, 2010

[162] L. R. Lynd, J. H. Cushman, R. J. Nichols and C. E. Wyman, Fuel ethanol from

cellulosic biomass, *Science*, vol. 251, pp. 1318-1323, 1991

[163] A. E. Farrell, R. J. Plevin, B. T. Turner, A. D. Jones, M. O'Hare and D. M. Kammen, Ethanol can contribute to energy and environmental goals, *Science*, vol. 311, pp. 506-508, 2006

[164] J. Goldemberg, Ethanol for a sustainable energy future, *Science*, vol. 315, pp. 808-810, 2007

[165] K. Kohse-Höinghaus, P. Oßwald, T. A. Cool, T. Kasper, N. Hansen, F. Qi, C. K. Westbrook and P. R. Westmoreland, Biofuel combustion chemistry: From ethanol to biodiesel, *Angewandte Chemie International Edition*, vol. 49, pp. 3572-3597, 2010

[166] Ó. J. Sánchez and C. A. Cardona, Trends in biotechnological production of fuel ethanol from different feedstocks, *Bioresource Technology*, vol. 99, pp. 5270-5295, 2008

[167] M. Balat and H. Balat, Recent trends in global production and utilization of bio-ethanol fuel, *Applied Energy*, vol. 86, pp. 2273-2282, 2009

[168] A. Gupta and J. P. Verma, Sustainable bio-ethanol production from agro-residues: A review, *Renewable and Sustainable Energy Reviews*, vol. 41, pp. 550-567, 2015

[169] I. Gelfand, R. Sahajpal, X. Zhang, R. C. Izaurralde, K. L. Gross and G. P. Robertson, Sustainable bioenergy production from marginal lands in the US Midwest, *Nature,* vol. 493, pp. 514-517, 2013

[170] H. Chen, D. Zhou, G. Luo, S. Zhang and J. Chen, Macroalgae for biofuels production: Progress and perspectives, *Renewable and Sustainable Energy Reviews*, vol. 47, pp. 427-437, 2015

[171] R. L. Costa, T. V. Oliveira, J. de Souza Ferreira, V. L. Cardoso and F. R. X. Batista, Prospective technology on bioethanol production from photo-fermentation, *Bioresource Technology*, vol. 181, pp. 330-337, 2015

[172] M. Wang, X. Pan, X. Xia, B. Xi and L. Wang, Environmental sustainability of bioethanol produced from sweet sorghum stem on saline–alkali land, *Bioresource Technology*, vol. 187, pp. 113-119, 2015

[173] F. Yüksel and B. Yüksel, The use of ethanol–gasoline blend as a fuel in an SI engine, *Renewable Energy*, vol. 29, pp. 1181-1191, 2004

[174] S. Kumar, N. Singh and R. Prasad, Anhydrous ethanol: A renewable source of energy, *Renewable and Sustainable Energy Reviews*, vol. 14, pp. 1830-1844,

_____

2010

[175] A. Kyriakides, V. Dimas, E. Lymperopoulou, D. Karonis and E. Lois, Evaluation of gasoline–ethanol–water ternary mixtures used as a fuel for an Otto engine, *Fuel*, vol. 108, pp. 208-215, 2013

[176] X. Feng and R. Y. M. Huang, Liquid separation by membrane pervaporation: A review, *Industrial and Engineering Chemistry Research*, vol. 36, pp. 1048-1066, 1997

[177] J. Z. Yang, Q. L. Liu and H. T. Wang, Analyzing adsorption and diffusion behaviors of ethanol/water through silicalite membranes by molecular simulation, *Journal of Membrane Science*, vol. 291, pp. 1-9, 2007

[178] M. Simo, S. Sivashanmugam, C. J. Brown and V. Hlavacek, Adsorption /desorption of water and ethanol on 3A zeolite in near-adiabatic fixed bed, *Industrial and Engineering Chemistry Research*, vol. 48, pp. 9247-9260, 2009

[179] A. Phan, D. R. Cole and A. Striolo, Preferential adsorption from liquid water–ethanol mixtures in alumina pores, *Langmuir*, vol. 30, pp. 8066-8077, 2014

[180] W. L. Jorgensen, J. D. Madura and C. J. Swenson, Optimized intermolecular potential functions for liquid hydrocarbons, *Journal of the American Chemical Society*, vol. 106, pp. 6638-6646, 1984

[181] L. Saiz, J. A. Padro and E. Guàrdia, Structure and dynamics of liquid ethanol, *The Journal of Physical Chemistry B*, vol. 101, pp. 78-86, 1997

[182] L. Lu, Q. Shao, L. Huang and X. Lu, Simulation of adsorption and separation of ethanol–water mixture with zeolite and carbon nanotube, *Fluid Phase Equilibria*, vol. 261, pp. 191-198, 2007

[183] Q. Shao, L. Huang, J. Zhou, L. Lu, L. Zhang, X. Lu, S. Jiang, K. E. Gubbins, Y. Zhu and W. Shen, Molecular dynamics study on diameter effect in structure of ethanol molecules confined in single–walled carbon nanotubes, *The Journal of Physical Chemistry C*, vol. 111, pp. 15677-15685, 2007

[184] S.-P Du, W.-H Zhao and L.-F Yuan, Absorption and structural property of ethanol/water mixture with carbon nanotubes, *Chinese Journal of Chemical Physics*, vol. 25, pp. 487-493, 2012